Institute of Thermoelectricity, Academy of Sciences and Ministry of Education and Science of Ukraine

Journal of THERMOELECTRICITY

International Research

Founded in December, 1993

published 6 times a year

No. 1 *2015*

Editorial Board

International Editorial Board

Founders - National Academy of Sciences, Ukraine
Institute of Thermoelectricity of National Academy of Sciences and Ministry of Education and Science of Ukraine

Certificate of state registration № КВ 15496-4068 ПР

Editorial office manager O. Pugantseva

Approved for printing by the Academic Council of Institute of Thermoelectricity of the National Academy of Sciences and Ministry of Education and Science, Ukraine

Address of editorial office:
Ukraine, 58002, Chernivtsi, General Post Office, P.O. Box 86.
Phone: +(380-372) 90 31 65.
Fax: +(380-3722) 4 19 17.
E-mail: jt@inst.cv.ua
http://www.jt.inst.cv.ua

Signed for publication 25.03.15. Format 70×108/16. Offset paper №1. Offset printing.
Printer's sheet 11.1. Publisher's signature 9.2. Circulation 400 copies. Order 6.

Printed from the layout original made by "Journal of Thermoelectricity" editorial board in the printing house of "Bukrek" publishers,
10, Radischev Str., Chernivtsi, 58000, Ukraine

CONTENTS

Articles of materials of XVI International Forum on Thermoelectricity

General Problems

L.I. Anatychuk. On the life and scientific activity of Jean-Charles Athanase Peltier. (Based on the materials of the film shown at the XVI International Forum on Thermoelectricity) 5

Material Research

A. I. Casian, J. Pflaum, I. I. Sanduleac. Prospects of low dimensional organic materials for thermoelectric applications 16

K.Sh. Kahramanov, F.K.Aleskerov, S.A. Nabiyeva, S.Sh. Kahramanov. Three-dimensional nanoobjects in the layered dissipative environments of $A_2^{V}B_3^{VI}$ 27

X. Zianni. Modeling the thermoelectric properties of modulated nanocomposites 35

Design

L.I. Anatychuk, O.V. Nitsovich Research of double-layer thermoelements with periodically profiled surface 41

T. Fröhlich, M. Hohmann, M. Schalles Calibration bench for heat flux sensors 49

Yu.M. Lobunets. Heat xchange-type TEG for micro-CHP 60

Thermoelectric products

D.F. Worner. Another update on the multi-mission radioisotope thermoelectric generator powering the curiosity rover 68

News

XVI International forum on thermoelectricity 81

Z. M. Dashevsky (Dedicated to 70-th birthday) 92

V.Y.Mychailovsky 94

L.I. Anatychuk

L.I. Anatychuk

Institute of Thermoelectricity NAS and MES of Ukraine
1, Nauky Str., Chernivtsi, 58029, Ukraine

ON THE LIFE AND SCIENTIFIC ACTIVITY OF JEAN-CHARLES ATHANASE PELTIER. (BASED ON THE MATERIALS OF THE FILM SHOWN AT THE XVI INTERNATIONAL FORUM ON THERMOELECTRICITY)

The most complete description of Charles Peltier's life one can learn from Frederic Peltier's, his son, book. He writes in the preface to his book "Soon after my father's death I worked out a draft of his life story. It was only my poor health that was able to interfere with fulfillment of this work".

Despite his illness, he did manage to finish his book about Peltier and have it published in 1847 in Paris.

Apart from the book mentioned, 63 scientific publications by Peltier [1-63] and 32 articles and books where the details on Peltier are given [64-95] were used during preparation of this work.

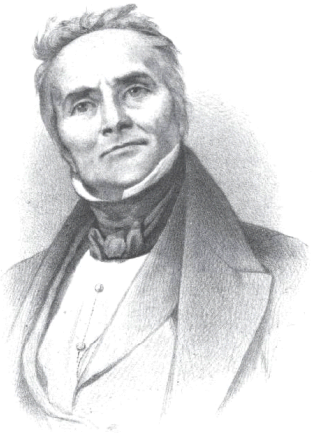

Fig. 1. Jean-Charles Athanase Peltier.

Jean Charles Peltier was born in the north of France in the small town of Ham, 130 km away from Paris. Peltier was born on February 22, 1785. Peltier's father was a shoemaker and his mother was a housewife. They sent young Peltier to school where the teacher could teach him only reading and writing.

Thus, Peltier did not receive any classical education. He was but a self-educated person.

But Peltier was a gifted child. When he was only 10 he disassembled, cleaned and repaired a watch. His father, impressed by the action, decided to help his son become a watchmaker. The father hired his son as an apprentice to a watchmaker, Brown by name, in the town of Saint-Quentin. That man did not possess better human qualities.

Peltier was an inquisitive youth. He was eager to read books by candlelight in the evenings. But Brown forbade him to do so. Peltier then got into the way of reading by moonlight thus driving Brown crazy. Peltier's father, on learning about the situation, took his son back home.

In 1802 at the age of 17 Peltier became a watchmaker apprentice in the famous Breguet Company. Marie-Antoinette, Queen of France, Napoleon Bonaparte, French Emperor and other celebrities wore the watches of this Company.

Peltier worked with great zeal. His endeavours were taken notice of: he was entrusted with making of chronometers, the major watchmaker's achievement.

But Peltier still longed for sciences. In 1815 he received a modest legacy that allowed him to leave work and dedicate his life to science.

In doing so, he practically followed Seebeck who left work after having received a small legacy to devote him to scientific experiments.

The fundamentals of thermoelectricity were laid, therefore, by great enthusiasts, and it was an unmistakable sign of their future success.

At first Peltier was tempted by literature and even wrote some poetry.

Then he turned to studying grammar rules which led him to the enigma of brain potential and the effect of electricity on its work.

Such was a miraculous way that led Peltier to electricity.

In 1827 he purchased an electrophorus machine. In the process of working with it he realized that it was necessary to have a more reliable source of electricity.

At that time it was voltaic pile (Fig.2).

The efforts to improve its operation were directed towards increasing the number of pile elements. M.Donn, for example, had increased the number of elements N from 30 to 3000.

In practice, though, it was somewhat different. The current I in the external circuit was saturated rapidly. At the same time, a great number of elements caused the decrease in stability of the source operation.

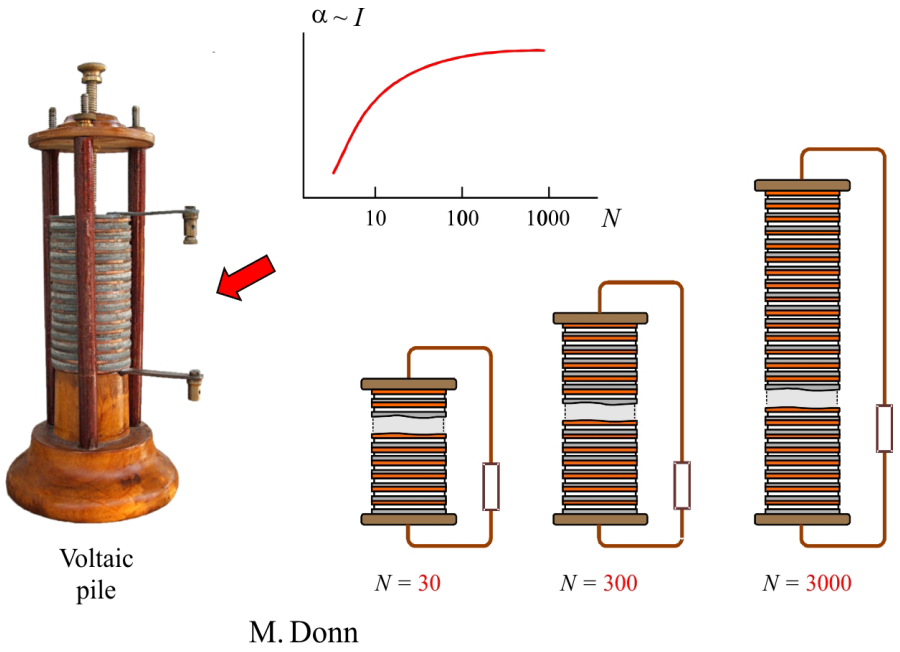

Fig. 2. Effect of voltaic cells number on the amount of current in the external circuit.

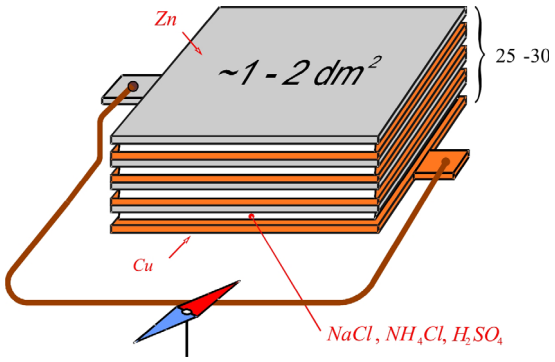

Puc. 3. Galvanic element that Peltier used.

Peltier chose a different way (Fig.3). Instead of increasing the number of elements, he increased their area to 1-2 dm^2. He used only about 25 to 30 elements and obtained some good results.

On July 19, 1830 Peltier pronounced those results for the first time during his speech held in the French Academy of Sciences.

Peltier made good use of thermoelectric sources. The first source of this kind was created by Oersted and Fourier in 1824. Peltier studied its

properties thoroughly. He established the dependence of the generated current on:

– the length of legs of thermocouples,

Fig.4. French Academy of Sciences where Peltier reported on the results obtained.

– the cross-section of legs of thermocouples,

– the number of in-series connected thermocouples,

– the level of heating of junctions of thermocouples.

Relying upon these data, Peltier created thermoelectric current sources for his experiments.

It is universally recognized that Ohm was the first to use a thermogenerator for experimental verification of his law in 1826. But it was Peltier who used a thermoelectric source earlier, in 1824, when he discovered his famous effect.

Peltier realized quite well that his experiments required highly sensitive and handy electric current measuring instruments.

Fig. 5. Schweigger's galvanometer.

A magnetized needle reacting to magnetic field excited by electric current served as such instrument at that period. This idea was brilliantly implemented by Schweigger, a German physicist, in 1820.

The device consisted of two pancake coils with a magnetic needle between them.

Peltier admired this device but realized that it was not suitable enough for carrying out experiments. That is why Peltier developed his very handy high-sensitivity galvanometers. The principal part of the said galvanometer was a magnetic needle haft on the spine. Friction between the spine and the depression in the magnetic needle was the main reason for the galvanometer low sensitivity. The similar requirement for minimal friction between axes and their latches in watches was crucial for

their proper work.

Therefore, Peltier surely used his high-class watchmaker's experience to minimize friction.

The excitation of magnetic field in galvanometers was generated from a single loop ribbon conductor in the circuits with low resistance. For the circuits with increased resistance magnetic field was produced by a multiloop coil.

Peltier widely used thermocouples for temperature measurements in his experiments. Antoine César Becquerel, a French physicist, fabricated a thermocouple of copper and iron in 1823 and connected it to Schweigger's galvanometer thus being able to measure temperature in the range from 0 to 300 ^{O}C.

With all his accuracy, Peltier set to studies on the properties of thermocouples as temperature measurers.

Firstly, he established that temperature readings depend strongly on the length 1 of the contact area of conductors. Short junctions should have been used.

Secondly, short junctions should have sizes very close to the diameters of the conductors.

Thirdly, poor contacts cause increase in the electric resistance of the junctions leading to distortions of temperature measurements.

Fourthly, Peltier established that when the temperature of liquids was measured with thermocouples, readings strongly depended on the depth of their immersion.

Fifthly, Peltier also established that thermocouples temperature readings depend upon the lengths of conductors connecting them to the galvanometer.

The performed researches encouraged Peltier to develop a witty device with amazing sensitivity, which played a decisive role in discovery of his famous effect. It is so called Peltier's thermoscopic clip (Fig.6).

In the figure you can see a variant of this device. It contains "jaws" 1 of two thermocouples that elastically grip the object of temperature measurements 2 with a steel plate 3.

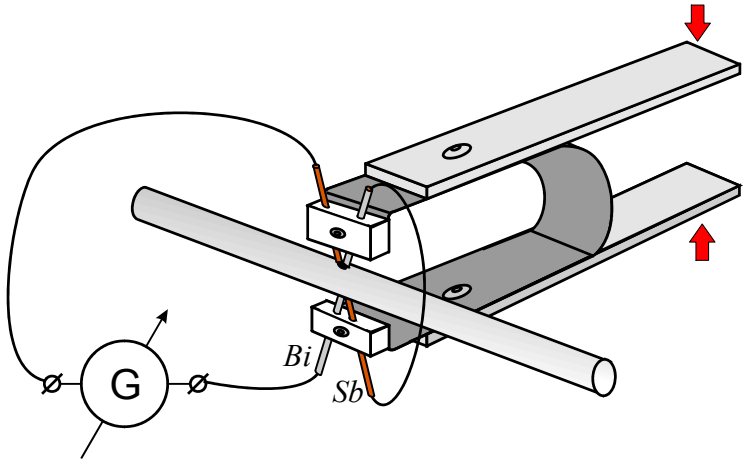

Fig.6. Peltier's thermoscopic clip.

The legs of thermocouples were fabricated of bismuth and antimony. Large values of thermoEMF coefficients of these materials and application of two in-series thermocouples made the said device especially sensitive.

To harmonize electric resistances of thermocouples and a galvanometer, a special coil with 80 loops of copper wire for magnetic field induction was used.

The device created by Peltier was, actually, a multiplier that consisted of two thermocouples.

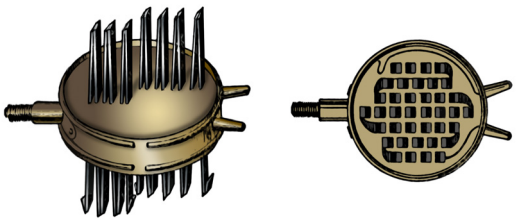

Fig.7. Nobile's multiplier.

As early as 1830, an Italian physicist Nobeli developed a multiplier consisting of 38 *Bi-Sb* components (Fig.7).

The device was so sensitive it was able to register the heat of human body in a dark room from the distance of 9 to 10 m. In fact, it was a prototype of a heat direction finder.

Therefore Peltier took special measures of precaution to eliminate negative influence of various external heat sources on measurements with his device.

The variety of means of experiment enabled Peltier to set a series of experiments that resulted in discovery of his famous effect.

It was very popular at that time to measure electric resistivity of metals. Peltier was also tempted to do this. He started measuring bismuth and antimony resistances because others failed to do it.

Peltier succeeded in casting of rods of bismuth and antimony with the diameter of 0.5 mm and length of 45 mm.

A thermocouple was used by Peltier as a current source. The galvanometer was a low-resistance one and consisted of a thick copper wire loop and, surely, a magnetic needle. Deflection of the magnetic needle when a rod with unknown resistance was used was compared to the rod with certain resistance.

This was how Peltier managed to do what no one else was able to. He was a venturesome researcher longing to do something what all the rest failed to do.

There was nothing special about this experiment, except bismuth and antimony rods. It was them that played a critical role in the Peltier effect discovery.

Peltier was led to experiments that resulted in discovery of his effect by the idea that at small currents new thermal effects should occur.

In Peltier words: "Till now thermal effects caused by electric current have not been measured with the help of sensitive devices so that we could enjoy the variety of phenomena occurring when the intensity of current is low".

It is well-known now that Joule-Lenz heat is proportional to the square of current, whereas the Peltier effect – to the first degree only. Therefore, with the decrease of the amount of current the Joule-Lenz heat will decrease rapidly thus giving chance for the Peltier effect to reveal itself. It is what exactly happened during Peltier experiments.

But Peltier knew nothing about that. One can but admire Peltier's keen insight in his expectations of new effects at small currents.

The layout of the experiment that led to the Peltier effect discovery consisted of a thermogenerator, low-resistance galvanometer and bismuth and antimony rods, fabricated before (Fig. 8).

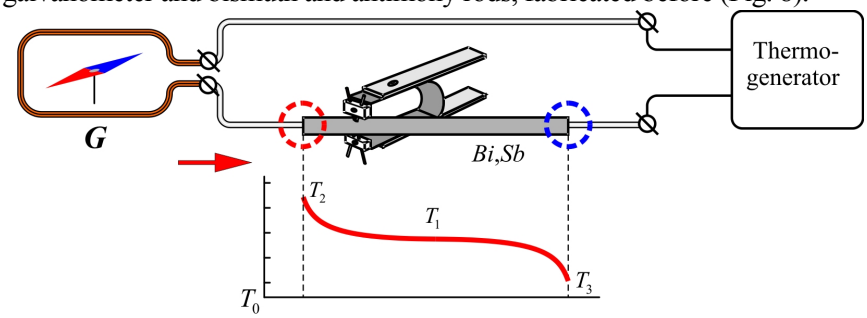

Fig.8. Layout of the experiment that led to the Peltier effect discovery
1 - temperature distribution along the rod, T_2, T_3 - temperature anomalies.

A thermoscope for measuring temperatures along the wires was employed.

Peltier sent the electric current through the rod and measured its heating with the thermoscope. In full agreement with Peltier's suggestions, a uniform heating by the current was observed in central parts of the samples. In the contact areas of samples with conductors, though, obvious temperature anomalies were observed, such as additional heating to temperature T_2 at one side and cooling to T_3 at the other. When the direction of current was changed, the temperature distribution became reversed.

Therefore, the Peltier effect consisted in anomalous heat release and absorbing at the areas of two different conductors connection if electric current was sent through them.

The discovery of his effect was promulgated by Peltier in 1824.

Peltier, certainly, expected some response to his discovery in contemporary scientific circles. Unfortunately, it did not happen. The Peltier's discovery attracted very little attention of the scientific community. There existed several explanations for this fact.

First, nobody saw any real use of this effect. Second, the discovery was made by a poorly educated man who might have simply been mistaken. And third, the effect was impossible to repeat in other laboratories.

The latter is easy to explain by absence of devices as sensitive as those developed by Peltier in other researchers' laboratories.

To convince the others in the presence of his effect, Peltier invents an extraordinary simple, elegant and, in his own opinion, persuasive experiment that was called a "thermal cross".

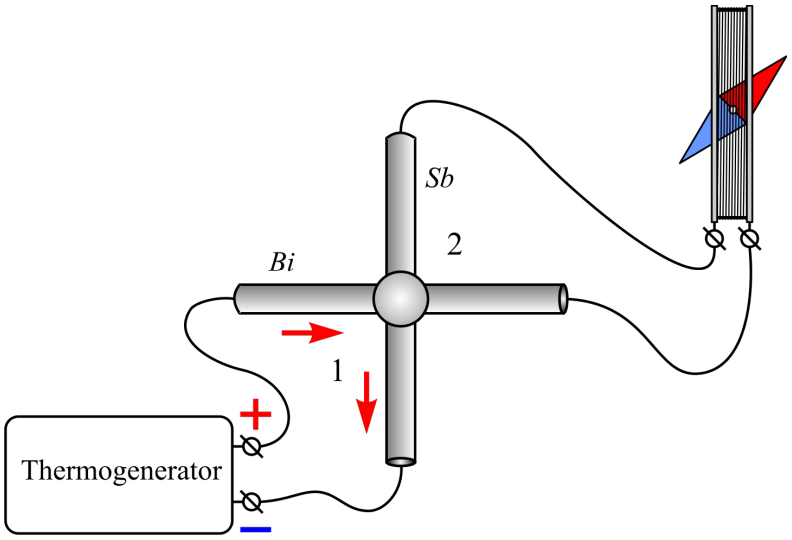

Fig.9. Peltier's thermal cross.
1, 2 – thermocouples of Bi and Sb, 3 – galvanometer.

The device really had the shape of a cross of two bars connected in the middle. One bar was made of bismuth, the other – of antimony. Such thermal cross formed two thermocouples, 1 and 2, connected at their junctions.

The experiment was as follows: electric current was sent through one of the thermocouples which, due to the Peltier effect, caused the junction cooling. The presence of such cooling was registered by the second thermocouple.

But even such experiment failed to convince sceptics.

The end to any doubts as for the Peltier effect was put by Lenz, a scientist from St. Petersburg, in 1838.

For this purpose he developed an experimental setup (Fig.10), the main parts of which were two rectangular bars of bismuth and antimony soldered in a butt joint. There was a hole where a drop of water was placed at the junction.

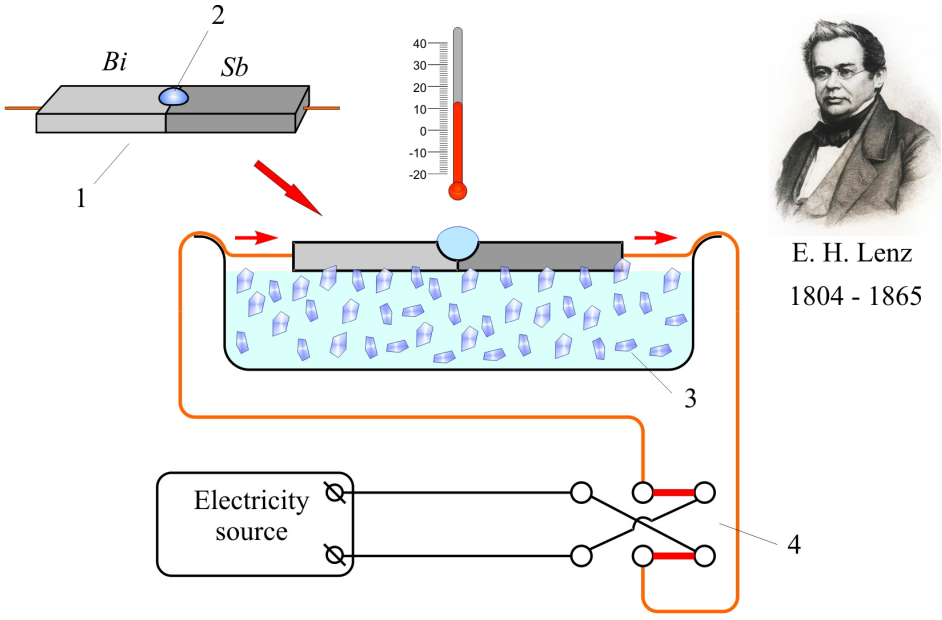

Fig.10. Lenz experiment layout
1 – rod of Bi and Sb, 2 – hole with a drop of water,
3 – melting ice, 4 – current switch

The rod was driven into contact with the surface of water with pieces of melting ice floating on it. The ends of the rod were connected to the source of electricity with the current switch. The switch served for changing the direction of the current.

When the current passed from bismuth to antimony, a drop of water froze and the temperature of -4.5^{O}C was registered by the thermometer. When the current direction was reversed, the drop of water melted.

This is the way the Peltier effect was rehabilitated and Lenz became famous as the first one who got ice from thermoelectricity.

After acknowledgement of his effect, Peltier became captivated by other researches. He studied the effect of electricity upon plants.

He developed a highly sensitive humidity meter where he employed a thermopile.

He studied electric potentials occurring between the Earth and air. For these purposes he used a wire one end of which was placed at the height of 25 metres, whereas the other one was put into a well 12 metres deep. An ultrasensitive galvanometer was embedded into the breakage of the wire. He established the connection between the readings of the device and weather conditions.

In general, he made a great contribution into development of the metrology scientific base.

Peltier lived at a very high speed. He worked to the point of exhaustion. He wrote: “I would rather die 10 years earlier and leave behind discoveries that will remind people of me”.

Peltier did implement his life plan. He died on October 27, 1845 at the age of 60 and a half. His name is familiar to the entire educated world.

References

1. Observations sur le rapport presente par M, Becquerel au Tribunal de Commerce de Rouen dans l'affaire de la trombe de Monville, *Revue Scientifique* VIII, 219-225 (1846).
2. Nouvelles experiences sur la caloricite des courants electriques, *Annal. de Chimie* LVI, 371-386 (1834*); L'Institut* II, 133-134, 265-266 (1834).
3. Pluie de crapauds, *L'Institu*t II, 346-347 (1834).
4. Experiences electro-magnetiques, *Annal. de Chimie* LX, 261-271 (1835).
5. Nouvelle observation meteorologique et electrique, *Paris, Bull Soc. Sci. Nat*., 90-91 (1835).
6. Observations microscopiques sur les animalcules, *Paris, Ball. Soc. Sci. Nat*., 92-95 (1835).
7. Electricite comparee du sol et des nuages, *Paris, Comptes Rendus* I, 94-95 (1835).
8. Sur la conduetibilite electrique, *Paris, Comptes Rendus* I, 203-204 (1835).
9. Sur une production d'electricite qui est due au simple contact de deux corps heterogenes, *Paris, Comptes Rendus* I, 360-361 (1835).
10. Lettre sur la puissance relative des divers metaux pour coercer l'electricite, *Paris, Comptes Rendus* I, 470-471 (1835).
11. Observations sur quelques causes d'erreur dans les mesures des tensions electriques, Annal de Chimie LXII, 422-432 (1836); *Paris, Soc. Philom. Proc. Verb*., 41-44 (1836).
12. Definition des mots quantite et intensite electriques, tiree d'experiences directes, *Annal de Chimie* LXIII, 245-255 (1836); *Froriep, Notizen* XLVII, 177-179 (1836); *Paris, Comptes Rendus* II, 475-476 (1836).
13. Lettre sur les animaux microscopiques, *Paris, Comptes Rendus* II, 134-135 (1836).
14. Electricite des nuages, *Paris, Comptes Rendus* III., 145-148 (1836).
15. Explication de phenomene, *Paris, Comptes Rendus* III, 148-149 (1836).
16. Observations nouvelles sur quelques animaux microscopiques, principalement sur une Vorticelle, *Paris, Soc. Philom. Proc. Verb*., 4-6 (1836).
17. Rhizopodes, *Paris, Soc. Philom. Proc. Verb*., 30 (1836).
18. Sur les effets negatifs des courants electriques sur les vegetaux et les animaux, *Paris, Soc. Philom. Proc Verb*. , 45-46 (1836).
19. Nouvelle espece de Floscularia, *Paris, Soc. Philom. Proc. Verb*., 63-64 (1836).
20. Note sur un mode de propagation des Arcelles vulgaires et scutelliformes (Arcellæ aculeatæ, Erh.), *Paris, Soc. Philom. Proc. Verb*., 64-66 (1836).
21. Recherches experimentales sur les divers phenomenes qui concourent a l'effet general des piles electriques, *Paris, Comptes Rendus* IV, 64-66 (1837); *Annal. de Chimie* LXVII, 422-444 (1838).
22. Sur l'electricite dynamique engendree par le frottement, *Paris, Comptes Rendus* IV, 172-173 (1837).
23. Sur une propriete assignee par M. De la Rive aux courants magneto-electriques, *Paris, Comptes Rendus* IV, 907-908 (1837); *Quetelet, Corresp. Math*. IX., 210-211 (1837).
24. Quelques observations sur la solubiliie et la dilution des corps, *Paris, Soc. Philom. Proc. Verb*., 70-75 (1837).
25. Observations sur les courants magneto-electriques, *Paris, Soc Philom. Proc. Verb*., 94-95 (1837).
26. Solution de la theorie de la pile, *Paris, Soc. Philom. Proc Verb*., 103-105 (1837).
27. Observations sur la structure des muscles et experiences sur la contraction, *Ann. Sci, Nat. IX. (Zool.)*, 89-96 (1838).
28. Observations sur une nouvelle espece de Floscularia, *Ann. Sci. Nat. X. (Zool.)*, 41-46 (1838).

29. Evaluation comparative des electricite statiqueet dynamique, *Paris, Comptes Rendus* VI, 816-818 (1838).
30. Sur la difference de capacite electrique des differents corps, *Paris, Comptes Rendus* VII, 965-968 (1838); *Sturgeon,Ann. Electr*. III, 560-563 (1838-39).
31. Sur l'origine et le developpement des zoospermes de la Grenouille, *Paris, Soc. Philom. Proc. Verb*., 43-44 (1838).
32. Memoire sur la formation des tables des rapports qu'il y a entre la force d'un coarant electrique et la deviation des aiguilles des multiplicateurs ; suivi de recherches sur les causes de perturbation des couples thermo- e1ectriques et sur les moyens de s'en garantir dans leur emploi a la mesure des temperatures moyennes, *Annal. de Chimie* LXXI, 225-313 (1839).
33. Sur la constitution des nerfs qui se rendent aux organes de la sensation et sur ceux qui se rendent aux organes de la locomotion, *Paris, Soc. Philom. Proc. Verb*., 20-23 (1839); *Ann. Sci. Nat XI. (Zool.),* 313-316 (1839).
34. Observations sur le fait precedent, *Annal. de Chimie* LXXV, 330-333 (1840).
35. Note sur la reproduction du Leucophrys vesiculosa, *Paris, Soc. Philom. Proc Verb*., 74-75 (1840).
36. Sur l'electricite atmospherique, *Paris, Soc. Philom. Proc. Verb*., 104-106 (1840); Sturgeon, *Ann. Electr*. VI, 135-137 (1841).
37. Recherches sur la cause de l'electricite des nuages, Paris, Comptes Rendus XII, 307-309(1841) ; *Archives de I'Electr*. I, 258-261 (1841); *Bibl. Univ. Archives* I, 258-261(1841); *Sturgeon, Ann. Electr*. VII, 370-372 (1841).
38. Temperature de l'eau placee sur un corps incandescent, *Paris, Soc. Philom. Proc. Verb*., 5-7 (1841).
39. Recherches sur la cause des phenomenes electriques de l'atmosphere et sur les moyens d'en recueillir la manifestation, *Annal .de Chimie* IV, 385-433 (1842); *Sturgeon, Ann. Electr*. X, 424-453 (1843); *Taylor, Scientif. Mem*. III, 377-415 (1843).
40. Sur la nature de l'electricite de l'air, Bruxelles, *Acad. Sci. Bull*. IX, 416- 422 (1842).
41. Sur les diverses especes de brouillards, *Bruxelles, Acad. Sci. Bull*. IX, (pte.2), 148-157, 496-500 (1842); *Annal. de Chimie* Vl, 129-155 (1842); *Bibl Univ*. XLII, 368-393 (1842); Walker, *Electr. Mag*. I, 416-417 (1845).
42. Sur les courants electriques propres aux animaux, *Paris, Soc. Philom. Proc. Verb*., 26-27 (1842).
43. Sur l'electricite atmospherique, *Bruxelles, Acad. Sci. Bull*. X, 201-207 (1843).
44. Sur le developement des l'electricite par un jet de vapeur, *Bruxelles, Acad. Sci. Bull*. X, 318-322 (1843); *Walker, Electr. Mag*. I, 450-453 (1845).
45. Meteorologie electrique, *Archives de l'Electr*. IV, 173-224 (1844).
46. Remarques sur quelques anomalies apparentes dans les phenomenes electriques produits par la foudre, *Archives de l'Electr*. IV, 580-583 (1844).
47. Essai de coordination des causes qui precedent, produisent et accompagnent les phenomenes electriques, *Bruxelles, Acad. Sci. Bull.* XI., (pte. 2), 31-34 (1844); *Bruxelles, Memoires Couronn.* XIX, (1845-46).
48. Sur l'electricite de la vapeur produite par les locomotives, *Bruxelles, Acad. Sci. Bull*. XI, (pie. 2), 34-39 (1844).
49. Sur la separation et l'individualisation des parties des animalcules au moyen de l'inanition, *Paris, Comptes Rendus* XVIII, 161-162 (1844).

50. Observation d'un double coup de foudre ascendante pendant l'orage du 9 Sep- tembre 1844, *Paris, Comptes Rendus*, XIX, 527 (1844).
51. Sur l'electricite des vapeurs provenant des bouilleurs a naute pression, *Paris, Soc. Philom. Proc. Verb.*, 58-62 (1844); *Archives de l'Electr*. IV, 474-479 (1844); *Walker, Electr. Mag*. I, 453-457 (1845).
52. Sur plusieurs causes d'erreur dans les observations de meteorologie electrique, *Paris, Soc Philom. Proc. Verb*., 70-74 (1844).
53. Observations sur les trombes, *Paris, Soc Philom. Proc Verb*., 80-82 (1844).
54. Recherches sur la cause des variations barometriques, *Bruxelles, Memoires Couronn*. XVIII, (1844-45); *Bruxelles, Acad. Sci*. Bull XII, 91-106 (1845); *Walker, Electr. Mag*. II, 147-153 (1846).
55. Sur les modifications eprouvees par les fils de metal qui ont servi longtemps de conducteurs electriques, *Archives de I'Electr*. V, 182-184 (1845).
56. De la cyanometrie et de la polarimetrie atmospherique, ou notice sur les additions et les changements faits au cyano-polariscope de M. Arago, *Bruxelles, Acad. Sci. Bull*. XII, 453-488 (1845).
57. Sur la cause des oscillations du niveau a bulle d'air, *Paris, Soc Philom. Proc.Verb*., 47-50 (1845); *Grunert, Archiv* VII, 1-3 (1846).
58. Theorie de l'electricite atmospherique, *Ann. Met. de France*, 180-183 (1850).
59. Peltier, Athanase, et Auguste, Bravais, Observations faites dans les Alpes sur la temperature d'ebullition de l'eau, *Paris, Comptes Rendus* XVIII, 572-583 (1844).
60. *Météorologie. Observations et recherches expérimentales sur les causes qui concourent à la formation des trombes*, J. C. A. Peltier, Bruxelles: Société belge de Librairie, 444p. (1841).
61. *Mémoire sur les diverses espèces de brouillards*, M. Ath. Peltier, T. XV, 25 (1842).
62. *Observations sur les multiplicateurs et sur les piles thermo-électriques*, J. C. A. Peltier, Paris: Imprimerie de E.-J. Bailly, place Sorbonne, 2, 14 p. (1839).
63. *Notice des faits principaux et des instrumens nouveaux ajoutés à la science de l'électricité,* J. C. A. Peltier, Paris: Imprimerie de E.-J. Bailly, place Sorbonne, 2, 7p (1839).
64. Sur l'electricite dynamique engendree par le frottement, *Paris, Comptes Rendus* IV, 172-173 (1837).
65. Nouvel hygrométre, *Paris, Comptes Rendus* IV, 767 (1837).
66. Sur une propriete assignee par M. De la Rive aux courants magneto-electriques, *Paris, Comptes Rendus* IV, 907-908 (1837).
67. Bernard S.Finn, Thermoelectricity, Washington, *Electronics and Electron Physics* 50, 182-184 (1980).
68. *Thermoelectrics Handbook: Macro to Nano*, Ed. by D.M. Rowe, Taylor & Francis, 2006.
69. Courants determines dans des fils métalliques par l'oxidation de quelques points de leur continuite, Lettre de M. Peltier, *Paris, Comptes Rendus* III, 176 (1836).
70. Courants electro-chimiques produits par le mercure, Lettre de M. Peltier a M. Becquerel, *Paris, Comptes Rendus* VI, 303-304 (1838).
71. Polarite secondaire des courants e1ectriques, Lettre de M. Peltier, *Paris, Comptes Rendus* VII, 763 (1838); *Bibl.Univ*. XVIII, 186-187 (1838).
72. Sur les circonstances qui ont acccmipagne la formation de la trombe par laquelle a ete ravagee, le 18 Juin 1839, la commune de Chatenay, Lettre de M. Peltier, *Paris, Comptes Rendus* IX, 112-115 (1839).

73. Sur les transports opere par la foudre, Lettre de M. Peltier, *Paris, Comptes Rendus* X, 202-204 (1840).
74. Recherches sur la cause qui maintient reunies les vapeurs dont se composent les nuages, Lettre de M. Peltier, *Paris, Comptes Rendus* X, 841-842 (1840).
75. Sur les circonstances qui determinent un degagement d'electricite quand de l'eau passe de l'etat liquide a l'etat de vapeur, Note de M. Peltier, *Paris, Comptes Rendus* XI, 908-910 (1840).
76. Sur le developpement des courants electriques par suite de la dissolution des gaz dans an liquide, Lettre de M. Peltier, *Paris, Comptes Rendus* XVI, 1006-1008 (1843).
77. Sur la nature electrique des trombes, Trombe de Cette, Lettre de M. Peltier, *Paris, Comptes Rendus* XIX, 1210-1212 (1844); *Palomba, Raccolta* I, 7-10 (1845); *Walker, Electr. Mag*. II, 7-11 (1846).
78. W. Thomson, The Bakerian Lecture, On the Electro-dynamic Qualities of Metals, *Philosophical Transactions of the Royal Society of London* **146**(3), 653-654 (1856).
79. Extension of Kelvin's Thermoelectric Theory, *Nature, Letters to editor* **68**(1752), 78-79 (1903).
80. D.D. Pollock, Thermoelectricity: theory, thermometry, tool (*ASTM; 852*), 2-6, 111-118, 244 (1985).
81. A.A. Buryak, N.B.Karpova, *Essays on Thermoelectricity Development*, Ed. by L.I.Anatychuk (Kyiv: Naukova Dumka, 1988), p. 8-10.
82. H.Kuhling, *Handbook on Physics*, Transl. from German, 2nd Ed. (Moscow: Mir, 1985), p. 374-375.
83. *Thermoelectric Materials and Converters*, Ed. by A.I.Karchevsky (Moscow: Mir, 1964), p. 11-23.
84. V.D.Gorbokonenko, N.Uchendu, Studies in the Field of Thermoelectricity, *Proc. of International Scientific Conference, November 20-22, 2012* (Ulyanovsk, State Technical University, 2012), p.97.
85. A.G.Samoilovich, *Thermoelectric and Thermomagnetic Energy Conversion Methods: Compendium of Lectures* (Chernivtsi: Ruta, 2006), p.72-73.
86. F.Rosenberg, *History of Physics*, Transl.from German, Ed.by I.Sechenov (Moscow, 1935), p. 201.
87. A.G.Samoilovich, L.L.Korenblit, Modern Status of Theory of Thermoelectric and Thermomagnetic Phenomena in Semiconductors, *Advances in Physical Sciences* 49(2), 244-246 (1953).
88. Peltier, Athanase, *The Brockhaus and Efron Encyclopedic Dictionary in 86 Volumes* (Saint-Petersburg, 1890—1907).
89. Yu.A.Khramov, *Peltier Jean Charles Athanase, Physicists: Biographical Guidebook*, Ed. by A.I.Ahieser, 2nd ed.(Moscow: Nauka, 1983), p.211, 400 p.
90. L.V.Sivukhin, *General Course of Physics, Vol.III, Electricity* (Moscow. Nauka, 1977).
91. B.M.Yavorsky, A.A.Detlaf, *Handbook on Physics: for Engineers and Students of Higher Educational Institutions, 4th ed.* (Nauka, Main Editorial Office for Physical and Mathematical Literature, 1968), p. 417.
92. L.D.Landau, O.M.Lifshits, *Theoretical Physics: Manual for Higher Educational Institutions in 10 Volumes, Vol.VIII, Electrodynamics of Continuous Media*, 4th Ed., 1982, 624 p.
93. A.I.Anselm, *Introduction to Theory of Semiconductors, 2nd ed*. (Moscow: 1978).
94. B.M.Askerov, *Electron Transition Phenomena in Semiconductors* (Moscow: 1985).
95. S.R.de Groot, *Thermodynamics of Irreversible Processes* (Moscow: State Publishers of Technical and Theoretical Literature, 1956), p. 174-197.

Submitted 12.02.2015

A. I. Casian[1], J. Pflaum[2], I. I. Sanduleac[1]

[1]Technical University of Moldova, MD-2004, Chisinau, Rep. of Moldova
[2]Julius-Maximilians University, Am Hubland, 97074 Wurzburg, Germany

PROSPECTS OF LOW DIMENSIONAL ORGANIC MATERIALS FOR THERMOELECTRIC APPLICATIONS

The aim of the paper is to present briefly the state-of-art and to analyze the prospects of thermoelectricity based on organic materials. It is shown that low dimensional nanostructured organic crystals have the highest prospects for thermoelectric applications. In these crystals, the density of electronic states is increased due to the low dimensionality of carrier spectrum and the interdependence between electrical conductivity, thermopower and the electronic thermal conductivity is somewhat overcome due to more diverse internal interactions. The thermoelectric properties of tetrathiotetracene–iodide crystals, TTT_2I_3 are analyzed in the frame of a more complete 3D physical model and the optimal parameters are determined in order to achieve values of the thermoelectric figure of merit at room temperature of ZT ~ 2 and even higher.

Key words: organic crystal, tetrathiotetracene–iodide crystal, 3D physical model, electrical conductivity, thermopower, electronic thermal conductivity, thermoelectric figure of merit.

Introduction

The search and investigation of new materials with increased thermoelectric figure of merit, *ZT*, continue to be an important and actual problem of solid state physics. In this domain during the last decade impressive results have been obtained. A value of $ZT \sim 2.2$ at 800 K was reported [1] in complex chalcogenide compounds of the type $AgPb_mSbTe_{2+m}$. $ZT \sim 2.4$ has been measured [2] at room temperature in *p*-type Bi_2Te_3/Sb_2Te_3 superlattice structures. Harman [3] has obtained $ZT \sim 3$ in *PbTeSe* quantum dot superlattices [3], and even $ZT \sim 3.5$ [4, 5]. It is known that for $ZT > 3$ the thermoelectric generators and refrigerators become economically competitive with those that are usually used nowadays. But the thermoelectric devices have evident advantages: no mechanical wear, long life, high reliability, no environmental pollution, noiseless operation. Therefore, the obtaining of materials with $ZT > 3$ is a big progress in this area. However, in spite of these impressive results, there are many difficulties for their practical applications, because the technology to obtain such structures is complicated, expensive and can not be applied for large scale production. Now the used thermoelectric materials have still low efficiency. Therefore, the commercialization of thermoelectric devices has still limited applications. Nevertheless, mass production of miniaturized thermoelectric modules has succeeded to maintain constant temperatures in the operation of laser diodes [5], seat heatings fabricated by Gentherm Corporation and installed in hundreds of thousands of vehicles each year [6, 7], portable beverage coolers [8] and other applications.

In the last years organic compounds attract more and more attention as materials which are less expensive, have more diverse and often unusual properties in comparison with their inorganic counterparts and their molecular structure can be easily modified to tune the desirable physical and chemical properties. Besides, the organic materials usually have low thermal conductivity due to their mainly dispersive interaction.

In poly3,4-ethylenedioxythiophene (PEDOT) doped by polystyrenesulphonate (PSS) thin films of *p*-type conductivity a value of the thermoelectric figure of merit $ZT = 0.42$ at room temperature has been measured [9] by optimizing the carrier concentration. It is reported also a value of $ZT = 1.02$ in PP-PEDOT/TOS [10] films, but the value of the thermal conductivity is taken from another study and thus has not been confirmed for the reported films of higher electrical conductivity. For *n*-type materials the best result is obtained in powder-processed inorganic hybrid polymer, poly[Kx-(*Ni*-ett)], with a $ZT = 0.2$ at 400 K [11].

It is expected that the nanocomposites of organic and inorganic components may have an even better thermoelectric performance than their individual components [12-16]. But no significant improvement in the figure of merit of this material class has been achieved until now. In PEDOT-based nanocomposites *ZT* varies between 0.02 and 0.1 [17]. The highest value of $ZT = 0.57$ at room temperature was measured in phenyl acetylene-capped silicon nano particles [18].

Different theoretical models describing the thermoelectric transport in organic materials have been also developed [19-24]. Ref. [24] should be mentioned explicitly, because a value of $ZT \sim 15$ at room temperature has been predicted in molecular nanowires of conducting polymers in spite of hopping conducting mechanism that usually leads to smaller carrier mobilities than band transport.

In highly conducting quasi-one dimensional (Q1D) organic charge transfer crystals we have predicted even higher values of $ZT \sim 20$ under some conditions [25, 26]. However, all predictions were made on the base of a strictly one dimensional physical model. In existing Q1D crystals of tetrathiotetracene-iodide, TTT_2I_3, grown from solution [27] with measured electrical conductivity $\sigma_{xx} = 1.8 \cdot 10^5\ \Omega^{-1}m^{-1}$, Seebeck coefficient $S_{xx} = 39\ \mu V/K$ and thermal conductivity $\kappa_{xx} = 1.0\ Wm^{-1}K^{-1}$ along the conductive chains only $ZT \cong 0.1$ was obtained at room temperature [28]. Such low value of *ZT* is explained by the fact that the crystals were not very pure and the parameters were not optimized.

More detailed modelings of the thermoelectric properties of TTT_2I_3 crystals, taking into account the interchain interaction in 2D approximation were also presented [29-31]. It was shown that in not very perfect crystals the results obtained by 2D and 1D approximation are very similar. First theoretical calculations in a more comprehensive 3D physical model have been partially realized in [32] and [33].

The aim of this paper is to present detailed modeling of the thermoelectric properties in the most complete 3D physical model and to determine realistic values of the thermoelectric figure of merit in TTT_2I_3 crystals with enhanced degree of purity. The criteria, when the simpler 1D model can be applied will be elucidated.

Three-dimensional crystal model for TTT_2I_3

From the structural point of view the Q1D crystals of tetrathiotetracene-iodide, TTT_2I_3, are formed from segregate stacks or chains of *TTT* molecules and iodine [30]. However, only *TTT* chains are conductive due to considerable overlap of π – electron wave functions along their stacking direction. Two molecules of *TTT* supply one electron to the iodine chain formed from I_3^- ions which play the role of acceptors. The electrons on I_3^- ions are in a rather localized states and do not participate in the transport. Thus, the carriers are holes. The electrical conductivity along *TTT* chains is almost of three orders of magnitude bigger than in transversal directions. Previously, due to this property the simpler 1D physical model was used [34-36] and the crystal was considered to be formed from independent 1D chains packed into a 3D crystalline structure. However, in reality some

additional interaction between the 1D conductive chains exists. Of course, this interchain interaction will affect somehow the results of the 1D approximation, especially in crystals with high degree of purity, when this interaction will limit the carrier mobility. Therefore, it is very important to determine the effect of interchain interaction on the thermoelectric properties in real crystals and, in this regard, to determine the criteria, when the simpler 1D model is still valid.

The charge and energy transport are described in the tight binding and nearest neighbors approximations. In the 3D model the energy of the hole with the quasi-wave vector $\boldsymbol{k}$ and its orthogonal projections (k_x, k_y, k_z), measured from the top of conduction band, has the form

$$E(\boldsymbol{k}) = -2w_1(1-\cos k_x b) - 2w_2(1-\cos k_y a) - 2w_3(1-\cos k_z c), \tag{1}$$

where w_1, w_2, w_3 are the hole transfer energies from a given molecule to the nearest ones along lattice vectors $\boldsymbol{b}$, $\boldsymbol{a}$, $\boldsymbol{c}$, the axes x, y, z are directed along $\boldsymbol{b}$, $\boldsymbol{a}$, $\boldsymbol{c}$, the conductive chains are directed along $\boldsymbol{b}$, therefore it is considered that w_1 is much bigger than w_2 and w_3.

Only longitudinal acoustic phonons are taken into consideration with the dispersion law

$$\omega_{\boldsymbol{q}}^2 = \omega_1^2 \sin^2(bq_x/2) + \omega_2^2 \sin(aq_y/2) + \omega_3^2 \sin(cq_z/2), \tag{2}$$

where the quasi-wave vector $\boldsymbol{q}$ has the projections (q_x, q_y, q_z), and ω_1, ω_2 and ω_3 are the limit frequencies in the x, y and z directions. Due to the quasi-one-dimensionality ω_1 is much bigger than ω_2 and ω_3.

As in previous 1D and 2D cases, two of the most important interactions of holes with acoustic phonons are considered, generalized for the 3D case. One interaction is similar to that of deformation potential with three coupling constants w_1', w_2' and w_3' determined by the variation of transfer energies with respect to intermolecular distances. The second interaction is similar to that of a polaron and is caused by the induced polarization of molecules surrounding the conduction hole. The coupling constant of this interaction is determined by the mean polarization of the molecules α_0.

The square of matrix element module describing the hole-phonon interaction has the form

$$\left|\mathrm{A}(\boldsymbol{k},\boldsymbol{q})\right|^2 = 2\hbar/(MN\omega_q)\{w_1'^2[\sin(k_x b) - \sin((k_x - q_x)b) + \gamma_1 \sin(q_x b)]^2 +$$

$$+ w_2'^2[\sin(k_y a) - \sin((k_y - q_y)a) + \gamma_2 \sin(q_y a)]^2 + w_3'^2[\sin(k_y c) - \sin((k_y - q_y)c) + \gamma_3 \sin(q_y c)]^2\}. \tag{3}$$

Here M is the mass of *TTT* molecule, N is the number of molecules in the basic region of the crystal. The parameters γ_1, γ_2 and γ_3 have the meanings of amplitudes ratios between the second interaction and the first one along the chains and in transversal directions

$$\gamma_1 = 2e^2\alpha_0/(b^5 w_1'), \quad \gamma_2 = 2e^2\alpha_0/(a^5 w_2'), \quad \gamma_3 = 2e^2\alpha_0/(c^5 w_3'), \tag{4}$$

where e is the elementary charge.

The scattering of holes by impurities is considered as point like and neutral is also taken into account. The impurity scattering rate is described in this case by a dimensionless parameter D_0 which is proportional to the impurity concentration and can be assumed very small, if the crystal purity is rather high. The variation of wave vectors $\boldsymbol{k}$ and $\boldsymbol{q}$ is considered in the whole Brillouin zones for holes and phonons, because the conduction band is not very large and the Debye temperature is relatively low for organic materials.

Transport properties

Let a weak electrical field and a weak temperature gradient be applied along the conductive chains. At room temperature it is possible to neglect the phonon energy and the transversal kinetic energy of the hole in the scattering processes, because they are much smaller than the kinetic energy of the hole along the chains. Then, the linearized kinetic equation is solved analytically and the electrical conductivity σ_{xx}, the Seebeck coefficient S_{xx}, the electronic thermal conductivity κ^e_{xx} and $(ZT)_{xx}$ can be expressed through the transport integrals R_n as follows

$$\sigma_{xx} = \sigma_0 R_0,\ S_{xx} = (k_0 / e)(2w_1 / k_0 T) R_1 / R_0, \tag{5}$$

$$\kappa^e_{xx} = [4w_1^2 \sigma_0 / (e^2 T)](R_2 - R_1^2 / R_0),\ (ZT)_{xx} = \sigma_{xx} S_{xx}^2 T / (\kappa^L_{xx} + \kappa^e_{xx}), \tag{6}$$

where

$$\sigma_0 = (2e^2 M v_{s1}^2 w_1^3 r) / (\pi^2 \hbar abc (k_0 T)^2 w_1'^2), \tag{7}$$

With $r = 4$ being the number of molecular chains contained in the transversal section of the elementary cell, k^L_{xx} is the lattice thermal conductivity, v_{s1} is the velocity of sound along the chains and R_n are the transport integrals

$$R_n = \int_0^2 d\varepsilon \int_0^\pi d\eta \int_0^\pi d\varsigma \varepsilon(2-\varepsilon) n_{\varepsilon,\eta,\varsigma}(1 - n_{\varepsilon,\eta,\varsigma}) \times$$

$$\times \frac{[\varepsilon + d_1(1-\cos\eta) + d_2(1-\cos\varsigma) - (1+d_1+d_2)\varepsilon_F]^n}{\gamma_1^2(\varepsilon-\varepsilon_0)^2 + D_0 + \{d_1^2(1+\gamma_2^2+2\sin^2\eta - 2\gamma_2\cos\eta) + d_2^2(1+\gamma_3^2+2\sin^2\varsigma - 2\gamma_3\cos\varsigma)\}/(8\varepsilon(2-\varepsilon))}. \tag{8}$$

Here, in order to compare with the 1D model, new dimensionless variables $\varepsilon = (1 - \cos(k_x b))$, $\eta = k_y a$ and $\varsigma = k_z c$ were introduced, $n_{\varepsilon,\eta,\varsigma}$ is the Fermi distribution function in this new set of variables, $\varepsilon_0 = (\gamma_1 - 1)/\gamma_1$ is the dimensionless resonance energy in the relaxation time in units of $2w_1$, $d_1 = w_2/w_1 = w_2'/w_1'$, $d_2 = w_3/w_1 = w_3'/w_1'$, $\varepsilon_F = E_F/2w_1$ is the 1D Fermi energy in units of $2w_1$. The 3D Fermi energy will be $2w_1(1+d_1+d_2)\varepsilon_F$. The parameter D_0 describes the hole scattering by impurities

$$D_0 = n_{im}^{3D} I^2 V_0^2 \frac{M v_s^2}{4b^3 a c w_1'^2 k_0 T}, \tag{9}$$

where n_{im}^{3D} is the density of impurities, I is the height of impurity potential and V_0 is the domain of potential action.

If we put in (8) $d_1 = 0$ and $d_2 = 0$, the integrals for η and ς can be calculated analytically and the results of the previously discussed 1D model are obtained. It can be seen that in this case the expression in the integral in (8) has a maximum for ε close to ε_0 and this maximum can be rather high, if D_0 is sufficiently small. It is a consequence of mutual compensation of the two mentioned hole-phonon interactions for states in the conduction band close to ε_0. In the 1D case this maximum is limited by D_0. Now the maximum is limited also by the rate of interchain scattering. Therefore, it becomes important to determine the criteria, when the entertain scattering will predominate, and further crystal purification will not yield better results.

In order to determine the parameters d_1 and d_2 we have calculated the electrical conductivity in the transversal directions σ_{yy} and σ_{zz}. Along these directions the overlap of hole wave functions is very weak and it is more convenient to write the Hamiltonian of the system in the representation of localized states at *TTT* molecules. Respectively, for the *y* and *z* direction the most important term in

the Hamiltonian becomes the hole-phonon interaction and the term which describes the motion of holes in the periodic lattice potential is considered as small perturbation. Therefore, a canonical transformation is applied to the Hamiltonian which permits to take into consideration the main part of the hole-phonon interaction already in the zero approximation. This also leads to considerable narrowing of the initial conduction band along the conductive chains. As a consequence, in the transversal directions the transport becomes of hopping type and the carriers can be described as small polarons.

Expressions for σ_{yy} and σ_{zz} were calculated numerically. By comparing them with the experimental data of $\sigma_{yy} \sim \sigma_{zz} = 3.3\ \Omega^{-1}\text{cm}^{-1}$, it can be estimated that $w_2 = w_3 = 0.015 w_1$. These values are of the same order because the lattice constants a and c in y and z direction are very close to each other.

Results and discussion

Expressions (5)–(8) have been calculated numerically for quasi-one-dimensional organic crystals of TTT_2I_3 with different degrees of purity. The crystal parameters are: $M = 6.5 \cdot 10^5 m_e$ (m_e is the mass of the free electron), a =18.35 Å, b = 4.96 Å, c = 18.46 Å, $v_{s1} = 1.5 \cdot 10^3$ m/s, $w_1 = 0.16$ eV, $w_1' = 0.26$ eVÅ^{-1}, $r = 4$, $d_1 = d_2 = 0.015$, $k_{xx}^L = 0.6$ WK^{-1}m^{-1}. The mean polarizability of *TTT* molecules was taken as in [30] $\alpha_0 = 45$ Å^{-3} and this leads to $\gamma_1 = 1.7$. The parameters γ_2 and γ_3 were calculated after (4). For the parameter D_0 the following values were chosen: 0.1 which corresponds to crystals grown by gas phase method [37] with stoichiometric electrical conductivity $\sigma_{xx} \sim 10^6\ \Omega^{-1}\text{m}^{-1}$; 0.02 which correspond to purer crystals grown also by gas phase method with somewhat higher $\sigma_{xx} \sim 3 \cdot 10^6\ \Omega^{-1}\text{m}^{-1}$, and 0.005 which corresponds to even more perfect crystals with $\sigma_{xx} \sim 6.6 \cdot 10^6\ \Omega^{-1}\text{m}^{-1}$ not obtained yet.

In Fig. 1 the dependences of electrical conductivity along chains σ_{xx} as functions of dimensionless Fermi energy ε_F in units of $2w_1$ are presented for these values of D_0.

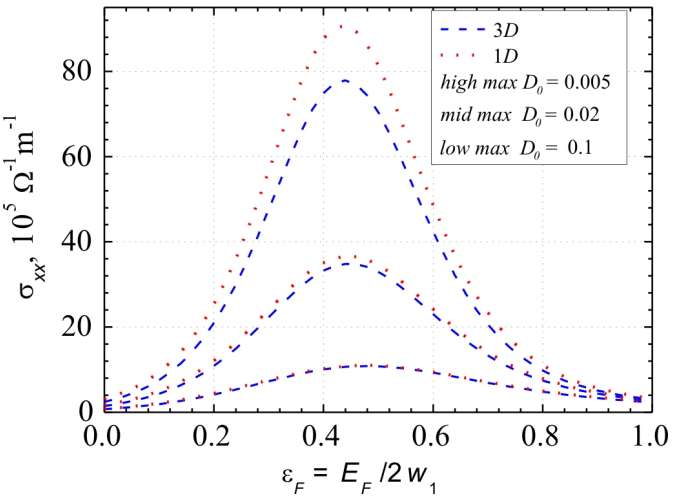

Fig.1. Electrical conductivity σ_{xx} along chains as a function of E_F for $\gamma_1 = 1.7$.

It can be seen that for not very pure crystals which corresponds to $D_0 = 0.1$ the results of the 3D model coincide with those of simpler 1D model in the entire region of ε_F variation. Even for purer crystals, i.e. $D_0 = 0.02$ the deviation of 3D model from the 1D model is still negligible. In these cases

the carrier mobility is limited by scattering at impurities, the scattering on adjacent chains does not give important contribution to σ_{xx} and the simpler 1D model may be used instead. In case of the purest crystals with stoichiometric electrical conductivity $\sigma_{xx} \sim 6.6 \cdot 10^6$ $\Omega^{-1}m^{-1}$ the deviation between 3D model and 1D amounts to ~ 18%. Now the carriers' scattering on adjacent chains gives significant contribution to σ_{xx} and the 3D model must be used.

In Fig. 2 the dependences of thermopower (Seebeck coefficient) along chains S_{xx} on Fermi energy at room temperature are presented. It is seen that the results of the models for 3D and 1D are very close across the whole interval of ε_F variation.

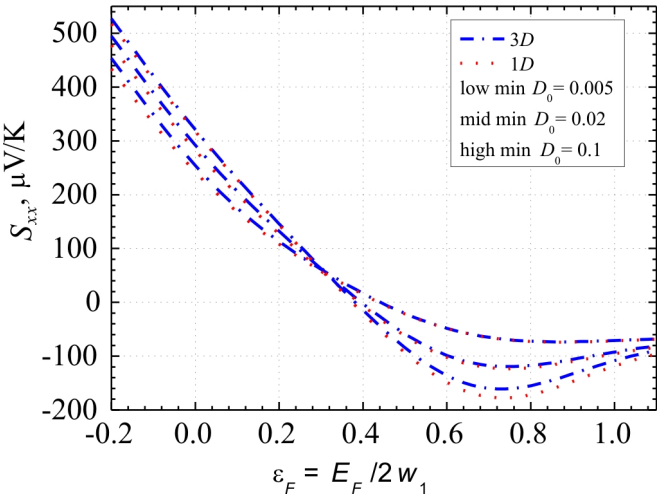

Fig. 2. Thermopower S_{xx} along chains as a function of E_F for $\gamma_1 = 1.7$.

As it is seen from (5), S_{xx} is proportional to the ratio of transport integrals R_1/R_0 and therefore is less sensitive to the interchain interaction. For stoichiometric crystals ($\varepsilon_F \sim 0.35$) S_{xx} weakly depends on crystal perfection and takes values between 35 and 40 μV/K as it is observed experimentally. With the decrease of ε_F from the stoichiometric value, S_{xx} grows considerably that is favorable for the improvement of the thermoelectric properties.

In Fig.3 the dependences of the electronic thermal conductivity along chains κ^e_{xx} on Fermi energy at room temperature are presented. It is seen that for crystals to which it corresponds $D_0 = 0.1$ and 0.02 with stoichiometric electrical conductivity $\sigma_{xx} \sim 10^6$ $\Omega^{-1}m^{-1}$ and $\sigma_{xx} \sim 3 \cdot 10^6$ $\Omega^{-1}m^{-1}$, respectively, predictions by the 3D and 1D model practically coincide. Only in the case of the purest crystals when $D_0 = 0.005$ a diminution of κ^e_{xx} by about 5% with respect to the 1D model is observed, less than in the case of σ_{xx}, where the diminution was ~ 18%. But the contribution of κ^e_{xx} to the total thermal conductivity has increased considerably. Even in less pure stoichiometric crystals κ^e_{xx} is 5.5 times bigger than κ^L_{xx} and up to 20 times in the most perfect crystals. This means that practically all thermal conductivity relates to the electronic part. It is also seen that the maxima of κ^e_{xx} are displaced to higher values of ε_F with respect to the maxima of σ_{xx}. This ensures a decrease of the Lorenz number in the interval of ε_F which is important for the increase of the thermoelectric figure of merit *ZT* and thus is favorable for the improvement of the thermoelectric properties.

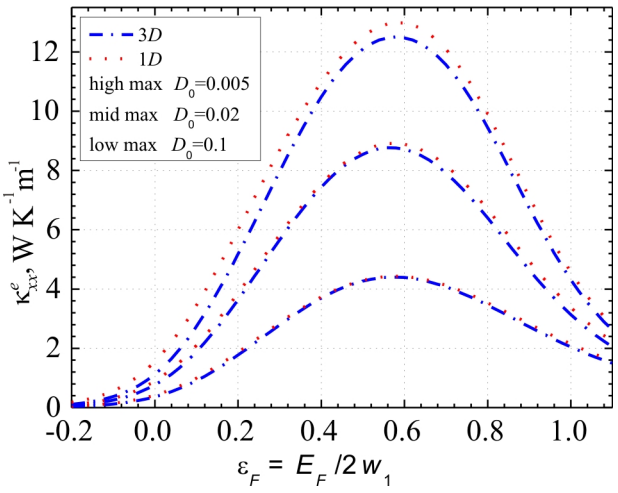

Fig.3. Electronic thermal conductivity along chains κ_{xx}^{e} as a function of E_F for $\gamma_1 = 1.7$.

The dependences of the thermoelectric figure of merit along chains *ZT* on Fermi energy at room temperature are presented in Fig.4.

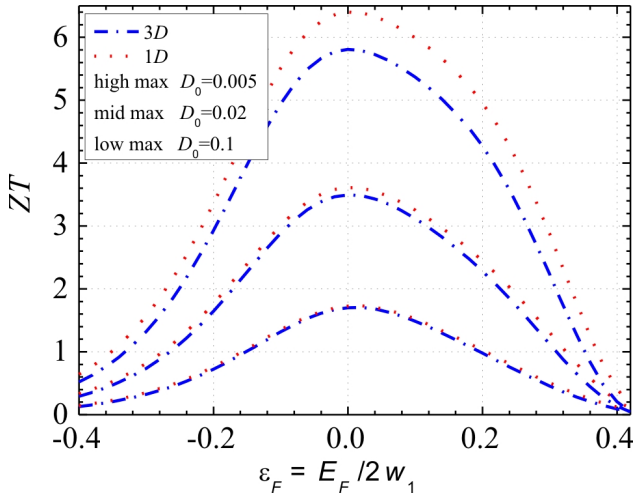

Fig.4. Thermoelectric figure of merit ZT along chains as a function of E_F for $\gamma_1 = 1.7$.

It can be seen that for crystals with $D_0 = 0.1$ and 0.02 the results of 1D and 3D model practically coincide. But for the most perfect crystals ($D_0 = 0.005$) the deviation between the 3D and 1D model becomes important. The decrease of *ZT* in the 3D model with respect to the 1D one achieves 10%, 16% and 40% for $\varepsilon_F = 0$; 0.2 and 0.35, respectively. In stoichiometric crystals (with $\varepsilon_F \sim 0.35$) *ZT* takes very small values even in the most perfect crystals, because the values of the Seebeck coefficient amount to ~ 40 μV/K and thus are very small. In order to increase *ZT* it is therefore necessary to decrease ε_F or the carrier concentration. As it is seen from the Figs. 1-3, in this case the electrical conductivity σ_{xx} decreases, but the thermopower S_{xx} grows considerably and the electronic thermal

conductivity κ_{xx}^{e} decreases. Thus, if ε_F is decreased down to 0.2 (the carrier concentration is decreased by 1.5 times, from $1.2\cdot10^{27}$ m^{-3} down to $0.81\cdot10^{27}$ m^{-3}) *ZT* is expected to achieve values of 1.0 in existing crystals grown by gas phase method with stoichiometric $\sigma_{xx} \sim 10^6$ $\Omega^{-1}m^{-1}$. The predicted thermoelectric parameters in this case are: $\sigma_{xx} = 4.1\cdot10^5$ $\Omega^{-1}m^{-1}$, $S_{xx} = 113$ μV/K, $\kappa_{xx}^{e} = 1.8$ $Wm^{-1}K^{-1}$ and $\kappa_{xx} = 2.4$ $Wm^{-1}K^{-1}$. The main contribution to the increase of *ZT* originates from the increase of the power factor $P_{xx} = \sigma_{xx}S_{xx}^2$. Now for TTT_2I_3 $P_{xx} = 5.2\cdot10^{-3}$ $Wm^{-1}K^{-2}$ which is higher than in Bi_2Te_3, were also $ZT \sim 1$, but $P_{xx} = 4\cdot10^{-3}$ $Wm^{-1}K^{-2}$.

Even higher values of $ZT \sim 2.2$ are expected in more perfect crystals with somewhat higher $\sigma_{xx} \sim 3\cdot10^6$ $\Omega^{-1}m^{-1}$ but which have not been obtained yet. The predicted parameters in this case are: $\sigma_{xx} = 11\cdot10^5$ $\Omega^{-1}m^{-1}$, $S_{xx} = 132$ μV/K, $\kappa_{xx}^{e} = 3.6$ $Wm^{-1}K^{-1}$ and $\kappa_{xx} = 4.2$ $Wm^{-1}K^{-1}$. In this case P_{xx} achieves a value of $1.9\cdot10^{-2}$ $Wm^{-1}K^{-2}$ which is about 4.7 times higher than that of Bi_2Te_3.

In this context, we can conclude that values of $ZT \sim 20$, predicted earlier in highly conducting Q1D organic crystals, are not realizable in TTT_2I_3, because in very pure crystals the carrier mobility becomes limited by the carrier scattering on adjacent chains. It is possible that in other structures, composed of more independent highly conducting molecular chains, such high values of *ZT* could be realized. But values of $ZT \sim 4$ are predicted in still more perfect crystals of TTT_2I_3 with stoichiometric $\sigma_{xx} \sim 6.6\cdot10^6$ $\Omega^{-1}m^{-1}$, if ε_F is decreased up to 0.2. The expected parameters in this case are: $\sigma_{xx} = 2.1\cdot10^6$ $\Omega^{-1}m^{-1}$, $S_{xx} = 146$ μV/K, $\kappa_{xx}^{e} = 5.2$ $Wm^{-1}K^{-1}$ and $\kappa_{xx} = 5.8$ $Wm^{-1}K^{-1}$. The thermal conductivity is increased considerably by 3.5 times with respect to Bi_2Te_3, but now the power factor amounts to $P_{xx} = 4.4\cdot10^{-2}$ $Wm^{-1}K^{-2}$, which is about 11 times higher than in Bi_2Te_3. Thus, if the crystals are more perfect, still more contribution to the increase of *ZT* comes from the increase of the power factor. This is favorable for the thermoelectric applications, because *ZT* is not limited by the lowest value of lattice thermal conductivity.

Conclusions

Detailed modeling of the thermoelectric properties of highly conducting quasi-one dimensional (Q1D) charge transfer organic crystals of TTT_2I_3 in the most comprehensive 3D physical model are presented. These crystals have the advantages that the density of electronic states is increased due to the low dimensionality of the carrier spectrum and the interdependence between electrical conductivity, thermopower and electronic thermal conductivity is somewhat compensated by the more diverse internal interactions. The dependences of electrical conductivity σ_{xx}, thermopower S_{xx}, electronic thermal conductivity κ_{xx}^{e} and of the thermoelectric figure of merit *ZT* along the chains on Fermi energy at room temperature are presented for 1D and 3D physical models. Three sets of TTT_2I_3 crystals are considered: rather pure ones with stoichiometric electrical conductivity $\sigma_{xx} \sim 10^6$ $\Omega^{-1}m^{-1}$, grown previously by the gas phase method [37], more perfect crystals with somewhat higher $\sigma_{xx} \sim 3\cdot10^6$ $\Omega^{-1}m^{-1}$, and even more perfect ones with $\sigma_{xx} \sim 6.6\cdot10^6$ $\Omega^{-1}m^{-1}$, not synthesized yet. It is shown that for the first and second set of samples the results of 1D and 3D model practically coincide. For the third set the scattering on adjacent chains becomes important and it is necessary to apply the 3D model to correctly describe the thermoelectric characteristics. It is obtained that in stoichiometric crystals *ZT* takes very small values even in the most perfect crystals, because the values of the Seebeck coefficient are about ~ 40 μV/K and thus are only very small. In order to increase *ZT* it is necessary to decrease the Fermi energy or the carrier concentration. Thus, if the carrier concentration is decreased

by 1.5 times, from $1.2 \cdot 10^{27}$ m^{-3} down to $0.81 \cdot 10^{27}$ m^{-3}, it is expected to obtain $ZT = 1.0$ in existing crystals with stoichiometric $\sigma_{xx} \sim 10^6$ $\Omega^{-1}m^{-1}$. Higher values of $ZT \sim 2.2$ are expected in more perfect crystals with somewhat higher $\sigma_{xx} \sim 3 \cdot 10^6$ $\Omega^{-1}m^{-1}$ but have not been obtained yet, and even $ZT \sim 4$ in still more perfect crystals of TTT_2I_3 with stoichiometric $\sigma_{xx} \sim 6.6 \cdot 10^6$ $\Omega^{-1}m^{-1}$. It is important to note that although the electronic part of the thermal conductivity grows considerably with increase of σ_{xx}, the main contribution to the increase of ZT originates from the increase of the power factor which is by 1.3; 4.7 and 11 times higher than that in Bi_2Te_3, respectively for three ZT values mentioned. With the decrease of carrier concentration the thermopower grows considerably and the rise is even bigger in the most perfect crystals. The optimal thermoelectric parameters which would permit to obtain the above mentioned values of ZT are determined.

Acknowledgement The authors gratefully acknowledge the support from EU Commission FP7 program under the grant no. 308768.

References

1. D. Bilc, S.D. Mahanti, E. Quarez, K-F. Hsu, R. Pcionek, and M.G. Kanatzidis, Resonant States in Electronic Structures of the High Performance $AgPb_mSbTe_{2+m}$: The Role of *Ag-Sb* Microstructures, *Phys. Rev. Lett.* **93**, 146403-1 (2004).
2. R. Venkatasubramanian, E. Sivola, et al. Thin-film Thermoelectric Devices with High Room-Temperature Figure of Merit, *Nature* **413**, 597 (2001).
3. M.S. Dresselhaus and J.P.Heremans in: *Thermoelectric Handbook, Macro to Nano*, Ed. by D. M. Rowe, CRC Press, 2006, Chap. 39 (and references therein).
4. C.B. Vining, *ZT*~ 3.5: Fifteen Years Progress and Things to Come, *Proc. of 5th Europe Conf. on Thermoel.* (Odessa. 2007), p. 5-10.
5. T.C. Harman, M.P. Walsh, B.E. LaForge, and G.W. Turner, Nanostructured Thermoelectric Materials. *J. Electronic Mater*. **34**, L19-L22 (2005).
6. Marlow Inc., "Transmission Lasers (DWDM)", as accessed on the website: http://www.marlow.com/industries/telecommunications/transmission-lasers-dwdm.html.
7. Gentherm, "Climate Seats", as accessed on the website: http://www.gentherm.com/page/climate-seats.
8. "Koolatron", as accessed on the website: http://www.koolatron.com/
9. G-H. Kim, L. Shao, K. Zhang, and K. P. Pipe, Engineered Doping of Organic Semiconductors for Enhanced Thermoelectric Efficiency, *Nat. Mater*. **12**, 719 (2013), DOI: 10.1038/NMAT3635.
10. T. Park, C. Park, B. Kim, H. Shin, and H. Kim, Flexible PEDOT Electrodes with Large Thermoelectric Power Factors to Generate Electricity by the Touch of Fingertips, *Energy Environ. Sci.* **6**, 788 (2013).
11. Y. M. Sun, P. Sheng, C. A. Di, F. Jiao, W. Xu, D. Qiu, and D. Zhu, Organic Thermoelectric Materials and Devices Based on *p* - and *n* -Type Poly(metal 1,1,2,2-ethenetetrathiolate)s, *Adv. Mater*. **24**, 932 (2012).
12. N. E. Coates, S. K. Yee, B. McCulloch, K. C. See, A. Majumdar, R. A. Segalman, and Jeffrey J. Urban, *Adv. Mater*. 25 , 1629 (2013).
13. W.Q.Ao, L.Wang, J. Q. Li, F.Pan, and C.N.Wu, Synthesis and Characterization of Polythiophene/Bi2Te3 Nanocomposite Thermoelectric Material, *J.Electron. Mat*. **40,** 9 (2011).
14. N. Toshima, N. Jiravanichanun, and H. Marutani, Organic Thermoelectric Materials Composed of Conducting Polymers and Metal Particles. *J. Electron. Mat*. **41**, 6 (2012).

15. J. Carrete, N. Mingo, G. Tian, H. Agren, A. Baev, and P. N. Prasad, Thermoelectric Properties of Hybrid Organic–Inorganic Superlattices, *The Journal of Physical Chemistry* C **116** (20), 10881 (2012).
16. Jihui Yang, Hin-Lap Yip, and Alex K.-Y. Jen, Rational Design of Advanced Thermoelectric Materials, *Advanced Energy Materials* **3**, 549 (2013).
17. P.J. Troni, I. Hoces, I. Singelin N.et al. Thermoelectric Materials: A Brief Historical Survey from Metal Junctions and Inorganic Semiconductors to Organic Polymers, *Isr. J. Chem*. **54**, 534-552 (2014).
18. Shane P. Ashby, Jorge García-Cañadas, Gao Min and Yimin Chao, *JEM*, **42**, 1495 (2013).
19. G. Kim, K. P. Pipe, Thermoelectric Model to Characterize Carrier Transport in Organic Semiconductors. *Phys. Rev.* ***B***, **86**, 085208 (2012).
20. J. Chen, D. Wang, Z. Shuai, First-Principles Predictions of Thermoelectric Figure of Merit for Organic Materials: Deformation Potential Approximation. *J. Chem. Theory Comput*. **8** (9), 3338 (2012) DOI: 10.1021/ct3004436.
21. J. Yang, Hin-Lap Yip, and Alex K.-Y. Jen, Rational Design of Advanced Thermoelectric Materials, *Advanced Energy Materials* **3**, 5, 549–565 (2013).
22. D. Wang et al., Modeling Thermoelectric Transport in Organic Materials, *Phys. Chem. Chem. Phys.***14**, 16505-16520 (2012), DOI: 10.1039/C2CP42710A
23. W. Shi, J. Chen, J. Hi et al., Search for Organic Thermoelectric Materials with High Mobility: The Case of 2,7-Dialkyl[1]benzothieno[3,2-b][1]benzothiophene Derivatives, *Chem. Mater*. **26**, 669−2677 (2014).
24. Y. Wang, J. Zhou, and R. Yang. *J. Phys. Chem. C* **115**, 24418 (2011).
25. A. Casian in: *Thermoelectric Handbook, Macro to Nano*, Ed. by D. M. Rowe, CRC Press, 2006, Chap.36.
26. A. Casian, Prospects of the Thermoelectricity Based on Organic Materials, *J. Thermoelectricity* **3**, 45 (2007).
27. V.F. Kaminskii, M.L. Khidekel', R.B. Lyubovskii et all. *Phys. Status Solidi* A **44**, 77 (1977).
28. A. Casian, I. Sanduleac, Thermoelectric Properties of Tetrathiotetracene Iodide Crystals: Modeling and Experiment, *J. Electron. Mat*. **43**, 3740 (2014).
29. A. Casian, I. Sanduleac, Effect of Interchain Interaction on Electrical Conductivity in Quasi-One-Dimensional Organic Crystals of Tetrathiotetracene-Iodide, *J. Nanoelectronics and Optoelectronics* **7**, 706-711 (2012).
30. A. I. Casian, I. I. Sanduleac, Organic Thermoelectric Materials: New Opportunities, *J.Thermoelectricity*, **3**, 2013.
31. I. I. Sanduleac, A. I. Casian, J. Pflaum, Thermoelectric Properties of Nanostructured Tetrathiotetracene Iodide Crystals in a Two-Dimensional Model, *Journal of Nanoelectronics and Optoelectronics,* **9**, 247-252, 2014.
32. I. I. Sanduleac, Thermoelectric Power Factor of TTT_2I_3 Quasi-One-Dimensional Crystals in the 3D Physical Model, *J. Thermoelectricity* **4**, 50 (2014).
33. A. Casian, I. Sanduleac, Thermoelectric Properties of Nanostructured Tetrathiotetracene Iodide Crystals: 3D Modeling, *Mat. Today Proc*. (2015), in press.
34. A. Casian, V. Dusciac, and Iu. Coropceanu. Huge Carrier Mobilities Expected in Quasi-One-Dimensional Organic Crystals. *Phys. Rev.* ***B*** **66**, 165404 (2002).
35. A. Casian, V. Dusciac, and V. Nicic. Thermoelectric Opportunities of Quasi-One-Dimensional Organic Crystals of Tetrathiotetracene–Iodide, *J. Thermoelectricity* **2**, 33-39 (2009).

36. A. Casian, J. Stockholm, V. Dusciac, and V. Nicik, Low-Dimensional Organic Crystal Tetrathiotetracene–Iodide as Thermoelectric Material: Reality and Prospects, *J. Nanoelectronics and Optoelectronics* **4**, 95-100 (2009).
37. B. Hilti and C.W. Mayer, Electrical Properties of the Organic Metallic Compound bis (Tetrathiotetracene)-Triiodide, $(TTT)_2I_3$, *Helvetica Chimica Acta* **61** (40), 501(1978).

Submitted 25.02.2015

K.Sh. Kahramanov, F.K.Aleskerov, S.A. Nabiyeva, S.Sh. Kahramanov.

NPO Selen of NANA, Baku, Azerbaijan

THREE-DIMENSIONAL NANOOBJECTS IN THE LAYERED DISSIPATIVE ENVIRONMENTS OF $A_2^{V}B_3^{VI}$

Comparison nanostructured Sb_2Te_3, Bi_2Te_3 crystals surface morphology and natural structures educed in them geometrically similar elements type of Benard cells, "bee honeycombs", some forms of hexahedral nanoobjects in the layered crystals were the example of dissipative structures. Self-organization processes in such systems results in forming of hexahedral structures on different hierarchical levels. Three-dimensional nanoobjects are similar to the structures of "bee honeycombs" and Benard cells hexahedral forms on the van der Waals surface of crystals of Sb_2Te_3, Bi_2Te_3 attributed to the interlayer structures - patterns. Similarity of such forms testifies to the single mechanism of the self-similar solid patterns formed by self-organization.
Key words: morphology, surface, dissipative structures, dislocations, nanostructuring.

Introduction

The emergence of dissipative structures is extremely important for the development of new processes of formation nanostructured materials. This, it belongs for example, the formation of hexagonal annular structures gold nanoparticles on a smooth substrate, and other pseudocrystal and hierarchically ordered structures. In [1-3], such systems are called "organized" and "structured". External flows of matter keep them in a steady state and does not allow move to equilibrium state. It is necessary to consider a number of approaches leading to spontaneous emergence of structures and their self-reproduction. This ability is related to the mechanism of appearance structures (localization processes factor) and spontaneous decay and diffusion in complex systems. This can manifest by examining fractals of different scales [4-6].

Shortest length of a circle of all the figures is a hexagon. Built at the same space on the hexagons requires less material than into squares or triangles. For example, consider a layered graphite and graphene. Ideal graphene consists exclusively of hexagonal cells. The presence of five and heptagonal cells will result to cuts in atomic plane in the cone. Another example – Benard cells. The emergence of Benard cells is a classic example of the spatial order of the structure. All the above are given in detail in the various published articles and monographs (e.g. [7-13]).

Depending on the concentration of embedded impurities in layered crystals $A_2^{V}B_3^{VI}$ <impurity> can be localized in the interlayer space and penetrate into the crystalline layers [10-11]. Purposeful introduction into layered semiconductors 3*d*-transition elements allows create structures with alternating, magnetic and semiconducting layers. Their thickness is several nanometers and, accordingly, a semiconductor material in which the combined magnetic and other properties. In studied $A_2^{V}B_3^{VI}$ single crystals is Predominant defects are dislocations located in the basal plane (0001). Hexagonal grid of dislocations and parallel rows presence found. Possible reactions occurring during the formation of the hexagonal mesh Sb_2Te_3 in similar reactions and are presented in [10]. Interest in the study of physical processes in the interlayer islet systems supported mainly by the fact

that they are a source of important information about the nature of the interaction between atoms migrate across the surface of the crystal structure and elements of the real patterns.

In terms of effects of interest are two fundamentally different situations: when all the islands in the ensemble at rest, or when for various reasons they can move across the substrate surface. In the first situation, the diffusion fluxes can cause transformation of resting forms islands and atom- wise diffusion transport of matter from island to island. In the second situation, against the background of these processes may also occur, mutual collisions of islands, accompanied by their diffusion merger. Both situations are carried out in real conditions [14-15].

In this works, an analysis of known natural dissipative structures, nanostructured crystalline samples and similar objects identified by atomic force microscopy (AFM) on the van der Waals surface of the crystal type $A_2^VB_3^{VI}$ (for example Sb_2Te_3, Bi_2Te_3).

Experimental results and discussion

Concepts and the experimental results describing processes of new phase origin and its subsequent evolution [4, 14-15] are used for surface nanoobjects growth mechanism analysis. The statement of material is carried out from positions of the classical approach allowing from uniform point of view to analysis of processes (0001) $A_2^VB_3^{VI}$ occurring on surface at self-intercalation and intercalation due to Ostwald ripening. For confirmation of conclusions used a dome-shaped and pyramidal forms nanoislands (NI) fragments AFM-images in $A_2^VB_3^{VI}$ <*Se, Zn*> made on various growth phase. Electron microscopic images were obtained with a scanning probe microscope (SPM) brand Solver Next.

In $Te^{(1)}$-$Te^{(1)}$ environments of $A_2^VB_3^{VI}$ by intercalation atoms between telluride quintets Benard cells formed when a temperature gradient is not only perpendicular to the plane (0001) Sb_2Te_3, but also along the plane. The experimental results are shown in Figs 1-4. Figure1 shows a hexagonal honeycomb-known; obtained Sb_2Te_3 AFM image (Fig.1.) clear evidence that these objects are very close in form.

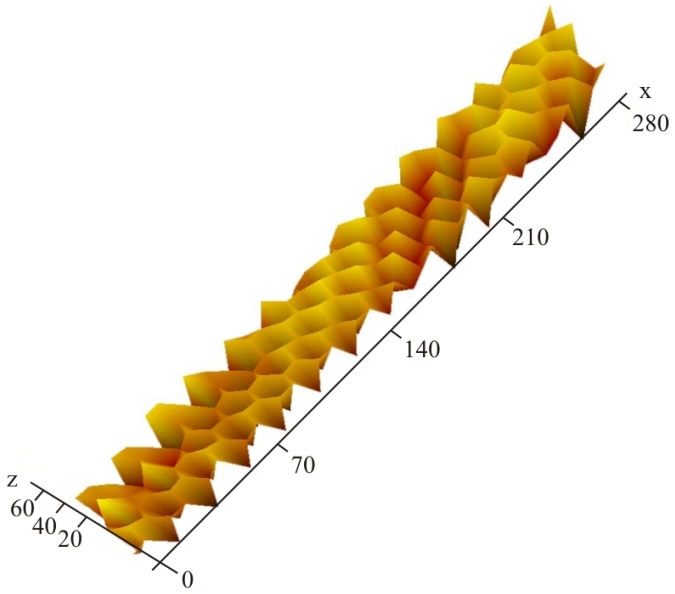

Fig.1. Photo of "bee honeycombs" in 3D scale on van der Waals surface.

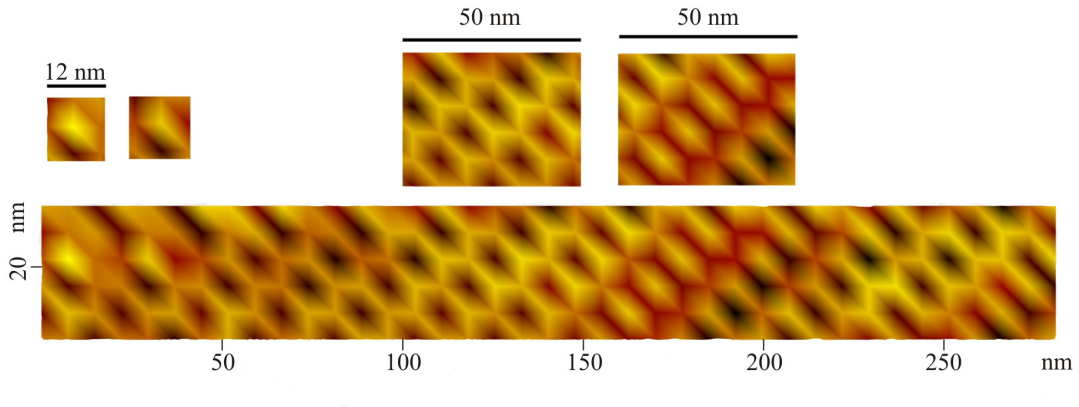

Fig.2. 2D AFM image of nanoobjects such "honeycomb of bees" in Sb_2Te_3:
in box at the top left are fragments of Benard cells images;
Upstairs, there are 2D- image (scan in 50×50nm) nanoforms such Benard cells.

In the middle of the top rate allocated hex (~ 50 nm) have the form of a grid similar to graphite; separate fragment in 3D- scale "bee cell" in the interlayer space Sb_2Te_3 given in Fig. 3.

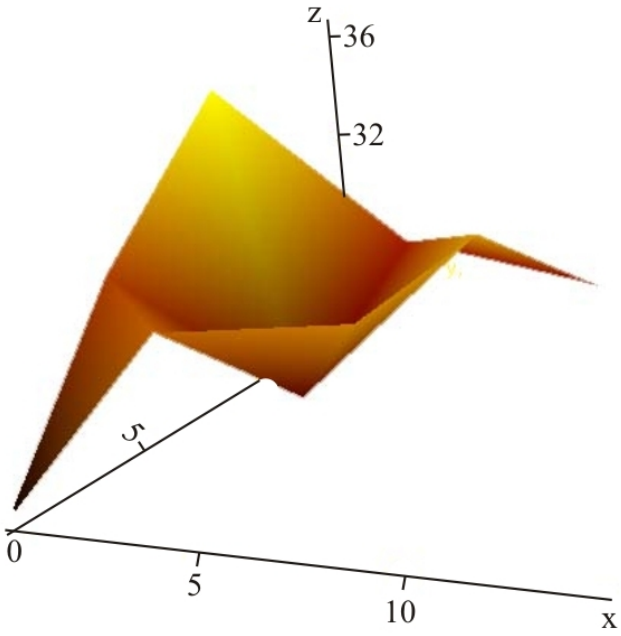

Fig.3. Separate three-dimensional fragment of " bee honeycomb" in Sb_2Te_3.

From profilograms (along the line 1 Fig. 4a), shown in Fig.4b seen that the height of the interlayer Benard cells ranges 12-16 nm, width has a size of about 10 nm. These structures are ordered and formed in the process of self-organization as well as other dissipative structure.

Highly ordered self-organizing structures in studied systems which far from equilibrium, have a certain shape and size of the spatial-time characteristic, they are stable against small perturbations. The most important characteristics of such dissipative structures is the localization region and the fractal dimension.

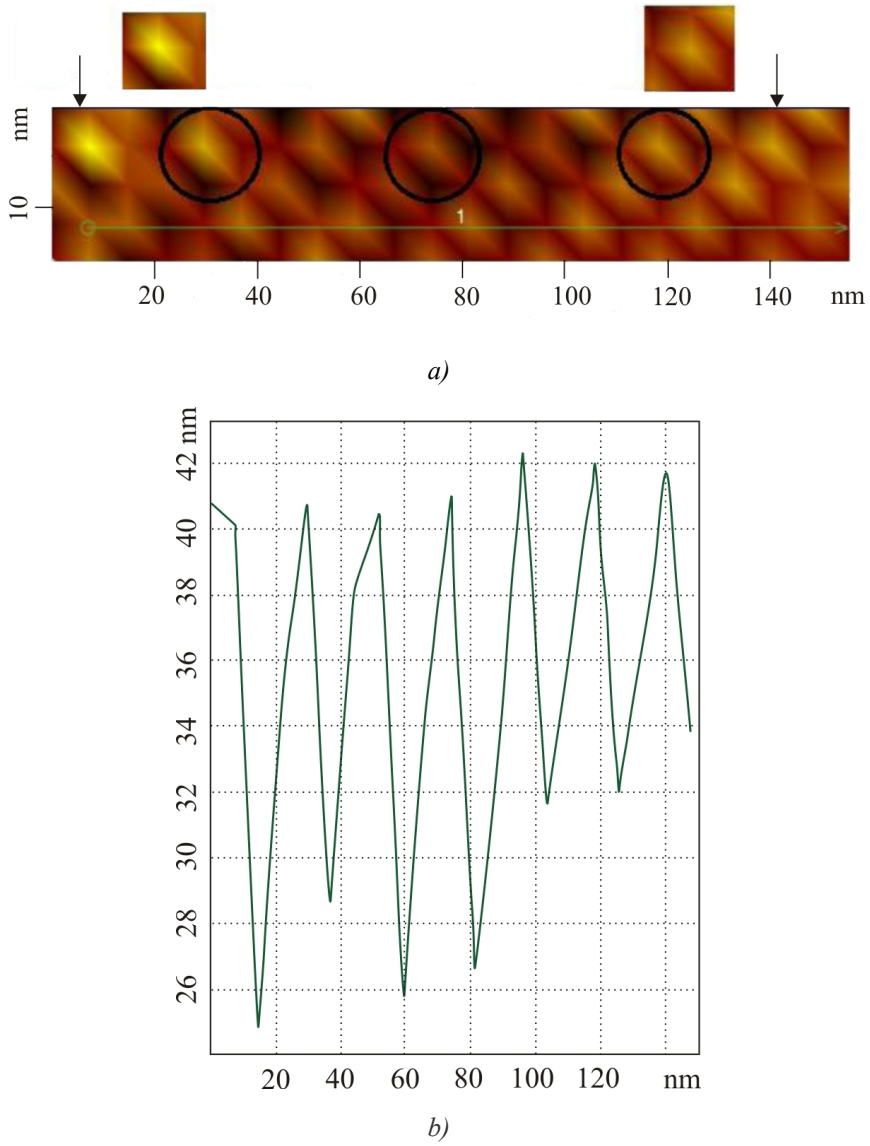

Fig.4. a) – 3D Benard's cells in Sb_2Te_3; b) – a profilogram along the line given in Fig.4a.

Complex systems are possible due to the hierarchical organization of systemic levels of complexity. It is obvious relationship between the phase transitions in the system state and abrupt changes of parameters. All phenomena occurring in nature (including in solids), in varying degrees, are interconnected. In considering the different scales of natural and man-made structures can be observed microlevel and macrolevel communication in the system hierarchy. In considering forms of seeming chaotic formations can detect the laws of growth of fractal forms [4-5, 11]. Given our experimental figures indicate not only fractality of natural processes, but also distributing them on nano-objects formed in layered systems (see Fig. 1-3, 5). These structures are identical to those obtained by modeling diffusion limited clustering hexagonal lattice "honeycomb" type [8, 12-13].

It is possible to distinguish three necessary (but not always sufficient) self-organization conditions in open systems with formation of dissipative structures:

– deviation from equilibrium has to exceed critical value, i.e. the system has to be in area of existence of bifurcations;

– volume of system has to be rather great and surpass some critical volume in which there is a necessary number undamped fluctuations; interaction of these fluctuations creates streamlining in system;

– existence of positive feedback.

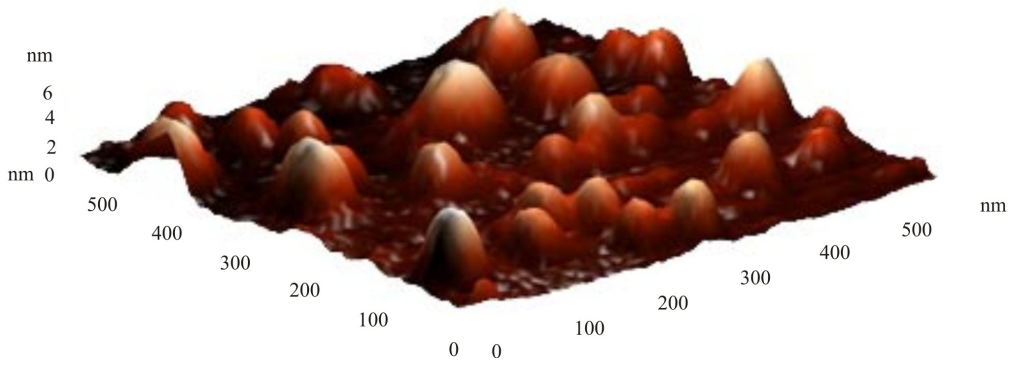

a)

b) *c)* *d)*

Fig.5. Forms of interlayer patterns in $A_2^VB_3^{VI}$ <impurity>:
a) – dome-shaped don't facetted nanoislands (Bi_2Te_3 <Cu>); b) – facetted nanoislandsNI (Bi_2Te_3 <Zn>);c) – localized patterns - (Sb_2Te_3); d) – don't facetted nanoislands (Bi_2Te_3 <Se>).

Self-organization of interlayer structures patterns in thermoelectric systems

We presented researches results of three-dimensional nanoobjects similar to "bee honeycombs" and hexagonal shape on van der Waals surface of Sb_2Te_3, Bi_2Te_3 crystals. Questions are considered of self-organization and formation of structures – patterns in crystalline solids. They are related with the concepts of dissipation associated with damping of various kinds of motions and the need for forming predictably repeating patterns in open systems.

In Fig.5 presents various forms of patterns grown in environs $Te^{(1)}$-$Te^{(1)}$ $A_2^VB_3^{VI}$ <impurity> . Determined their classification associated with localized spatial ordering, the sustainability of existing in conservative dissipative nonequilibrium environments.

The term "dissipative structures" unites all types of patterns. Concept of a pattern we applied to solid-state structures of various sizes.

It was analyzed solid-state conservative dissipative patterns in nanostructured $A_2^VB_3^{VI}$ crystals and similar natural objects patterns are revealed. The experimental testify not only fractal similarity of

natural macroobjects but also about dissemination of them on the nanoobjects formed in the crystals of $A_2^VB_3^{VI}$.

Nanoobjects in Fig.5 are received by various methods. They are interesting to that are natural and regular (their single fragments repeat). In literature they are called nanoparticles, nanoislands (NI), clusters depending on their structure and the function which is carried out by them.

Numerous experiments on growth of nanoobjects show that the form of germs on a surface changed in the course of their growth. Either it is facetted, or, on the contrary, becomes unstable or dendritic. This fact significantly influences a stage of Ostwald ripening and respectively their structure. Despite these changes as we see from Fig. 6, the created nanofragments in interlayer space have forms of don't facetted nanoislands. These structures are formed at self-intercalation of copper in space $Te^{(1)}$-$Te^{(1)}$ Bi_2Te_3- thus arise up don't facetted fragments. The faceted nanofragments are formed at intercalation of atoms on a surface (0001) of layered crystals. Growth of these islets occurs due diffusion in the space $Te^{(1)}$-$Te^{(1)}$ of $A_2^VB_3^{VI}$ <*Se, Zn*> and due to the mechanism of Ostwald ripening [14].

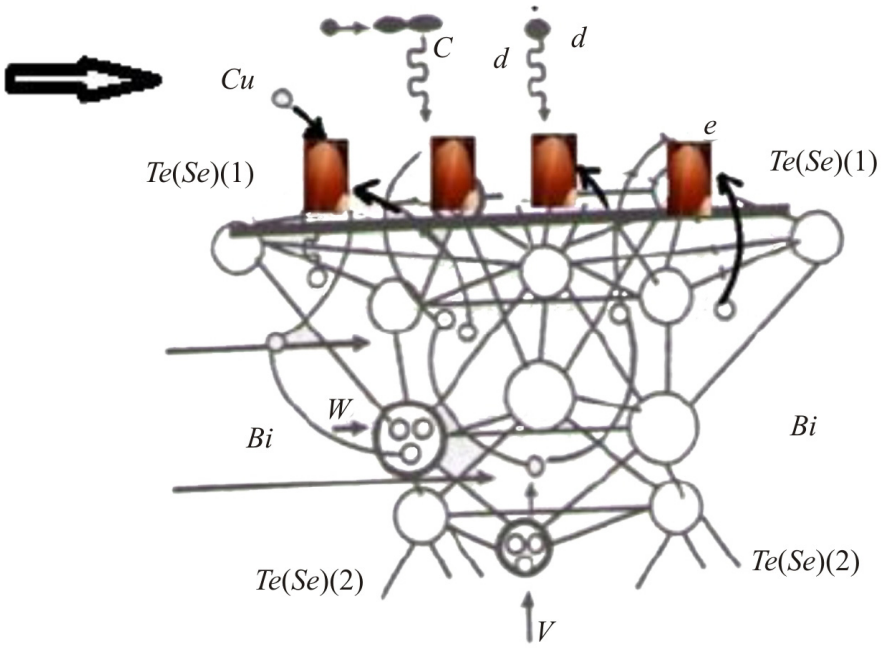

Fig. 6. Allocation scheme don't facetted NI on the van der Waals surface (0001) of Bi_2Te_3<Cu>, formed in the process of self-intercalation.

In both cases, the main mechanism for the growth faceted and don't faceted islets when limiting stage is the stage of the final surface diffusion and Ostwald ripening process.

We can say that the presented templates structures is followed particulars in clearly patterns; being between quintets $Te^{(1)}$-$Te^{(1)}$ $A_2^VB_3^{VI}$ these patterns move apart of quintets and actively participate in the scattering of electrons and phonons, which is manifested in a decrease lattice thermal conductivity in Bi_2Te_3 <*In, Se*> to K_L=5·10^2 W/cm·K at a total thermal conductivity K_t = 13.4·10^2 W/cm·K. In principle emergence of patterns in matter structure not a new phenomenon. Patterns in the world of particles can be similar to patterns not only in the world of atoms, but to those in solid-state structures. Except the given structures (Fig. 5) it is possible to review examples of patterns in composites, in multiphase eutectic systems.

Conclusion

Comparing the surface morphology of natural structures and morphology of nanostructured Sb_2Te_3 (Bi_2Te_3) crystals revealed geometrically similar elements. Benard cells, "bee honeycombs", some form of hexagonal nano-objects on the van der Waals surface of layered crystals were an example of conservative and dissipative self-organization. In such systems, self-organization processes in the $A_2^V B_3^{VI}$ interlayer space leads to the formation of hexagonal structures and nanoislets at various hierarchical levels.

Formation mechanisms of NI on a surface (0001) $Bi_2Te_3<Cu>$ at self-intercalation and intercalations analized on the basis models of atoms condensation processes at a stage of Ostwald ripening that were convenient model for studying of forming processes self-organized nanoobjects on (0001) surface of layered structures.At self-intercalation of copper from layers and vacant sites on a telluride surface (0001) Bi_2Te_3 where the rate-limiting step is process of condensation of *Cu* atoms, by a mechanism Ostwald ripening formed domed don't facetted nanoislets.

In the process of directed diffusion of atoms *Se, Zn* intercalation in the space $Te^{(1)}$-$Te^{(1)}$ on the (0001) surface self-organized nanostructures faceted pyramidal shapes in the $Bi_2Te_3<Se>$, and in $Bi_2Te_3<Zn>$ faceted NI formed due to coalescence of small NI.

In the deformed layered crystals in $Te^{(1)}$-$Te^{(1)}$ interlayers are created dissipative systems. Along with microdeformation in deformable crystals of $A_2^V B_3^{VI}$ there is a macroplastic current in which three-dimensional structural elements in combination with processes of the accelerated migration and coalescence participated. Dissipative structures in playing a role of macrodefects reduce the general heat conductivity of a crystal and by that increase its thermoelectric efficiency.

References

1. Nikolis G., Prigozhin I.// Self-Organization in Non-Equilibrium Systems.Wiley.1977,ISBN 0-471-02401-5.
2. Prigozhin I. // From Being To Becoming. Freeman. 1980, ISBN 0-7167-1107-9.
3. Raygorodsky A.M .//Problem of Borsuk. M.: Изд. МЦНМО,2006,p.9-56.
4. Mandelbrot B. B.// The Fractal Geometry of Nature, W. H. Freeman & Co, 1982, ISBN 0-7167-1186-9.
5. Prigozhin I., Stengers I.// Order out of Chaos: Man's new dialogue with nature. Flamingo. 1986, ISBN 0-00-654115-1.
6. Feder J.//Fractals, Springer, 1988, ISBN 0306428512, 9780306428517.
7. Geim A.K. // Random wandering – unpredictable way towards graphene. Usp. Fiz. Nauk, 2011, t.181, №12, pp. 1284-1298.
8. Schroeder M.R. // Fractals, Chaos, Power Laws. W.H. Freeman & Company, 1991.
9. Gasenkova I.V., Svechnikova T.E.//Research of structure of monocrystals of solid solutions on the basis of bismuth telluride// Thermoelectrics and their application, St. Petersburg, 2002, page 145.
10. Gasenkova I.V., Ivanova of L.D. Granatkin Yu.V//Inorganic materials, RAS, 2001, t.37. №. 11, pp. 1306 - 1312.
11. F.K.Aleskerov, E.M.Derun, M. G. Pishkin, G. Kavei, S.Sh. Kakhramanov.//Some features of nanoobjects formation in interlayer space of Bi_2Te_3 crystals //"Physics", Baku, Elm, T.XIII, 2007, pp.41-50.
12. P. Mikin. // Some last achievements in modeling by limited diffusion of aggregation and related processes. Fractals in physics, Works VI of the international symposium on fractals in physics (MSTF, Trieste, Italy. July, 1985) p. 281.

13. L. Turkevich, G. Cher.//Law of large-scale transformation of probability of accession of a particle to the DOA models. Fractals in physics, Works VI of the international symposium on fractals in physics (MSTF, Trieste, Italy. July, 1985) p. 310.
14. Kukushkin S.A., Osipov A.V.//Processes of condensation of thin films, Usp. Fiz. Nauk, 1998, t.168, № 10, pp. 1083-1116.
15. Geguzin I.E, KaganovskyJu.S./ A diffusive transfer of mass is in islands tapes, Usp. Fiz. Nauk, 1978, t.125, №3, pp.48-525.

Submitted 27.02.2015

X. Zianni

X. Zianni

Dept. of Aircraft Technology, Technological Educational Institution of Sterea Ellada, 34400 Psachna, Greece
Dept. of Microelectronics, Institute for Nanoscience and Nanotechnology (INN), NCSR 'Demokritos' 15310 Athens, Greece

MODELING THE THERMOELECTRIC PROPERTIES OF MODULATED NANOCOMPOSITES

Nanocomposite materials are promising for improved thermoelectric (TE) properties compared to the constituent bulk-like materials. Main effects on electrons and phonons transport properties originate from scattering on boundaries/interfaces and energy barriers. In nanostructures with a 1D doping concentration modulation, a TE power factor enhancement was predicted in the presence of two phases for the electron transport and non-uniform thermal conductivity. We have explored the influence of the composite nanostructure dimensionality on the TE efficiency enhancement. The two- and three-dimensional non-uniform nanostructures have been modeled by a network model. Our results indicate two regimes depending on the distribution of the non-uniformity in the nanostructures. The transport properties can be interpreted by either average properties or by the formation of percolation paths for conduction. Our study indicates that a network analysis could be useful in designing thermoelectric composite materials and to interpret experimental data.

Key words: modeling; thermoelectric transport properties; nanocomposites; network analysis

Introduction

Efficient thermoelectric materials require good electron transport properties and poor thermal conductivity. Nanocomposite materials are promising materials for enhancement of the thermoelectric efficiency. In nanocomposites, the electron and phonon properties are decoupled due to the structural and/or compositional non-uniformity. So far most high performance TE units are based on inorganics/metalloids or their composites [1]. Since the discovery of TE properties of intrinsically conducting polymers such as polyanilines, polypyrroles, polythiophenes or their derivatives are intensively investigated because they possess relatively low thermal conductivity, good electrical conductivity and are easy to prepare, air stable, light weight and much less costly in their production compared to their inorganic counterparts [2, 3]. Recently, it has been demonstrated that the introduction of low dimensional nanostructures in organic composites materials [4-5] has significantly improved TE characteristics due to inter-component junctions, thereby leading to phonon scattering and hoping of charge carriers [6, 7]. In addition, the use of organic/inorganic nanocomposites has attracted much attention due their exceptional electrical, thermal and mechanical characteristics [8-16].

We have previously explored the prospects for thermoelectric (TE) efficiency enhancement in non-uniform nanostructures above the quantum confinement regime [17-18]. In this regime, electrons and phonons can be treated as bulk-like carriers experiencing effects of the non-uniformity as they move through the nanostructure. Main effects on their transport properties originate from scattering on boundaries/interfaces and energy barriers. In one-dimensional modulated nanostructures (nanowires), a TE power factor enhancement was predicted in the presence of two phases for the electron transport and non-

uniform thermal conductivity [18]. We have explored the influence of the nanostructure dimensionality on the TE efficiency enhancement. The two- and three- dimensional non-uniform nanostructures have been modeled by a network model [19]. The model is described in section II. In section III, we present the structures that we have investigated and our results on the calculated transport properties. The main conclusions are drawn in section IV.

Model

We have used a network model software for calculating the thermoelectric properties, i.e. total electric and thermal resistances and total Seebeck coefficient, of modulated composite materials [19]. The real structure of the composite sample is translated into a pixel grid where local transport properties are assigned to each pixel including bulk-like properties as well as interface properties to adjacent pixels which can be adjusted to account for real interfaces. The resulting networks are embedded between a left and a right contact, each at constant temperature and constant electrostatic potential. By using nodal analysis, the total thermal and electric resistances of the structure, as well as local voltages or temperature differences between the pixels are obtained. In an additional step, the local temperature differences are used to simulate local Seebeck voltages as voltage sources between the pixels in order to obtain the total Seebeck voltage and, thus, the Seebeck coefficient, of the structure.

Results and discussion

We have modeled nanocomposite materials consisting of two phases: the TE-phase dispersed within the M-phase. The M-phase consists of a matrix material with the properties of the bulk material. The TE-phase consists of a material with enhanced Seebeck coefficient. Concerning the conductivity, we consider that the TE-phase is dispersed in (i) a conductive M-phase or in (ii) an insulating M-phase. In the former (latter) case, the conductivity of the TE-phase is lower (higher) that the conductivity of the M-phase.

We explore the dependence of the transport properties on the composition of the nanocomposite as expressed by the percentage (%) of the bulk-like phase (M-phase) in the composite material. In Fig. 1, there are shown three schematics of the nanocomposite material with different % of the bulk-like phase.

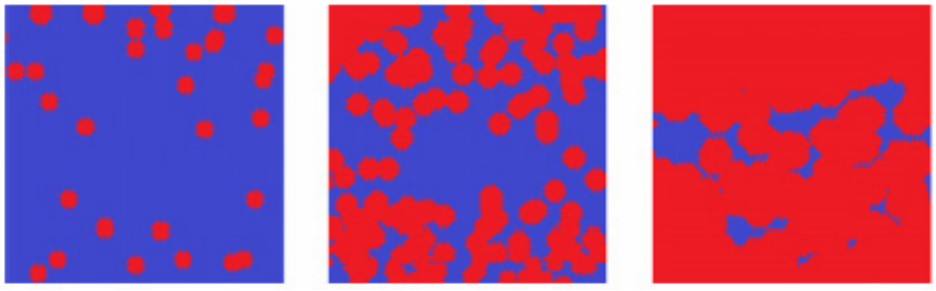

Fig. 1. A two-phase nanocomposite with the increasing ratio of the TE-phase (red) over the M-phase (blue) from left to right.

(i) TE- phase dispersed in a conductive M-phase

The transport properties of the composite material are shown in Fig. 2 and Fig.3 with respect to the transport properties of the bulk-like M-phase. In the left panel of Fig. 2, it is shown the conductivity of the nanocomposite material. The conductivity increases when the percentage of the more conductive M-phase increases. We have considered the following cases for the transport properties of the two constituent phases:

(a) uniform Seebeck coefficient and thermal conductivity (blue squares), (b) enhanced Seebeck in the TE-phase and uniform thermal conductivity (green dots), (c) enhanced Seebeck and slightly lower thermal conductivity in the TE-phase, κ_{TE}=0.8 κ_M (magenta triangles) and (d) enhanced Seebeck and strongly lower thermal conductivity in the TE-phase, κ_{TE} =0.1 κ_M (red diamonds). The conductivity of the composite material has been found the same in all cases (a)-(d). In all these cases, it increases from the TE-phase conductivity to the M-phase conductivity with increasing % of the M-phase. In the right panel of Fig. 2, it is shown that the thermal conductivity of the composite material also increases from the TE-phase thermal conductivity to the M-phase thermal conductivity with increasing % of the M-phase.

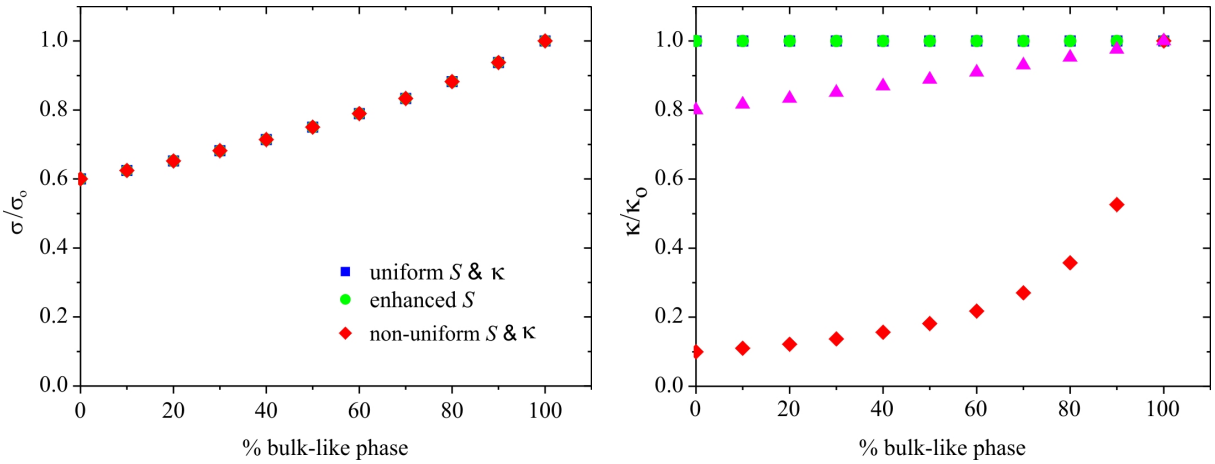

Fig. 2. The conductivity (left panel) and the thermal conductivity (right panel) of the composite material as function of the percentage of the bulk-like phase (M-phase). The symbols are explained in the main text.

The Seebeck coefficient of the composite material is shown in the left panel of Fig. 3. When the thermal conductivity of the TE-phase is the same (green dots) or slightly lower (magenta triangles) than the thermal conductivity of the M-phase, the Seebeck coefficient of the composite decreases nearly linearly with increasing % of the M-phase. A less steep decrease is found when the TE-phase has considerably lower thermal conductivity (red diamonds). In this case the composite material has enhanced Seebeck coefficient even at low concentrations of the TE-phase. In the right panel of Fig. 3, it is shown that in this case the TE power factor of the composite material is significantly enhanced. The effective TE power factor is ~4 times higher than that of the bulk-like material when a ~ 10% of the TE phase is dispersed in the composite material.

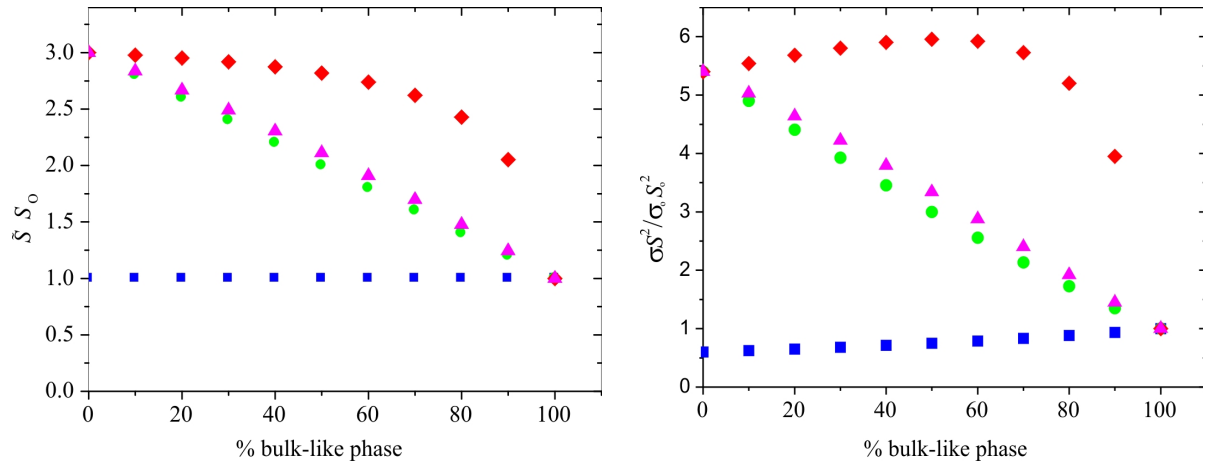

Fig. 3. The Seebeck coefficient (left panel) and the power factor (right panel) of the composite material as function of the percentage of the bulk-like phase (M-phase). The symbols are as in Fig. 2 and are explained in the main text.

(ii) TE-phase dispersed in an insulating M-phase

It has been assumed hat $\sigma_{TE} = 60\ \sigma_M$ and uniform thermal conductivity. The transport properties of the composite material are shown in Fig. 4 and 5 with respect to the transport properties of the TE-phase. The conductivity of the composite material is shown in Fig. 4 for 3D (blue diamonds), 2D (green dots), and 1D (red squares) structures. As expected, the effective conductivity decreases with increasing percentage of the M-phase. It can be noticed that the decrease is steep and shows a percolation threshold that depends on the dimensionality of the material structure. In 3D, a percolation path is formed at a rate concentration of ~.20-0.30. In 2D, a percolation path is found at ~0.5. In 1D, there is no percolation threshold because a percolation path cannot be formed. In this case, the conductivity is interpreted by the effective conductivity of a 1D in-series resistor network. The conductivity decreases smoothly with increasing percentage of the insulating M-phase.

The Seebeck coefficient is shown in the left panel of Fig. 5. The same percolation threshold behavior is found for the Seebeck coefficient as for the conductivity in 2D and 3D. A linear increase is found in the case of 1D similarly as that found for a conductive M-phase. The transport properties are interpreted in both cases (i) and (ii) by the properties of an effective medium rather by those of a percolation path.

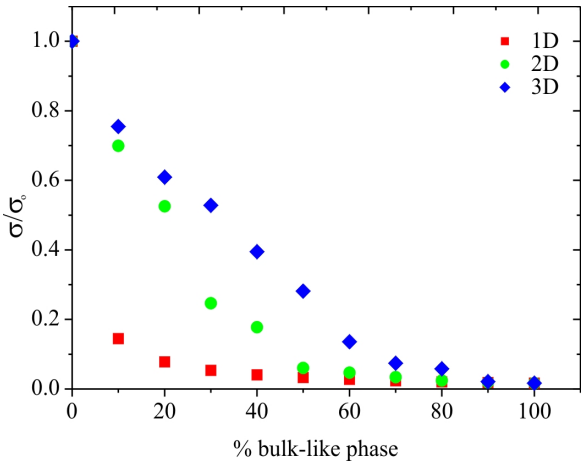

Fig. 4. The conductivity of the composite material with respect to the TE-phase conductivity for 1D (red squares), 2D (green dots) and 3D (blue diamonds) structures.

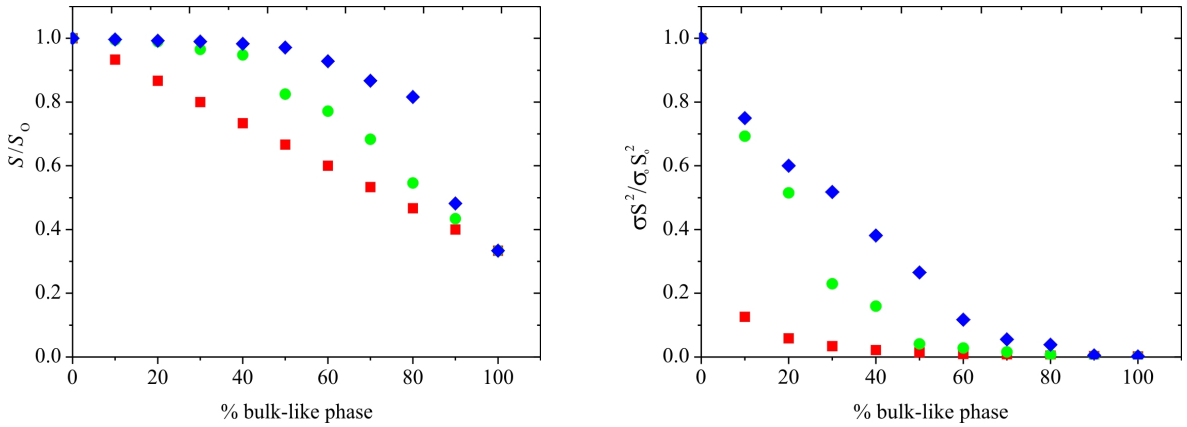

Fig. 5. The Seebeck coefficient (left panel) and the TE power factor (right panel) of the composite material with respect to the corresponding TE-phase properties for 1D (red squares), 2D (green dots) and 3D (blue diamonds) structures.

The TE power factor is shown in the right panel of Fig. 5. A very low TE power factor is found below the percolation threshold in 3D and 2D. The TE power factor increases rapidly above the

percolation threshold and is determined by the transport properties of the percolation path (TE-phase properties). In 1D, the decrease of the TE power factor is interpreted by the transport properties of the effective medium.

Conclusion

We have investigated the thermoelectric transport properties of a composite material in the presence of two phases. A bulk-like phase (M-phase) and a phase with enhanced TE properties (TE-phase). We have used a network analysis model to calculate the thermoelectric properties of the composite material. We have found that the thermoelectric properties of the composite material are strongly dependent on the material composition. Moreover, they depend on the relative transport properties of the two phases. We have identified two distinct regimes. When the M-phase is conductive, the thermoelectric properties of the composite material can be estimated by those of the effective medium with the average composition of the two phases. When the M-phase is insulating, the thermoelectric properties of the composite material are very poor below the percolation threshold. They improve rapidly above the percolation threshold and they are determined by the properties of the percolation path. Our study indicates that a network analysis could be useful in designing thermoelectric composite materials and to interpret experimental data.

Acknowledgment Funding by the European Social Fund (ESF)-European Unions and National Resources within the framework of the Grant of Excellence “ARISTEIA” is acknowledged.

References

1. A.J.Minnich, M.S.Dresselhaus, Z.F.Ren, and G.Chen, Bulk Nanostructured Thermoelectric Materials: Current Research and Future Prospects, *Energy Environ. Sci.* **2**, 466–79 (2009).
2. O.Bubnova and X.Crispi, Towards Polymer-Based Organic Thermoelectric Generators, *Energy Environ. Sci.* **5**, 9345–62 (2012).
3. N.Dubey and M.Leclerc, Conducting Polymers: Efficient Thermoelectric Materials, *J. Polym. Sci. B* **49** 467–75(2011).
4. N.Toshima, M.Imai and S.Ichikawa, Organic–Inorganic Nanohybrids as Novel Thermoelectric Materials: Hybrids of Polyaniline and Bismuth(III) Telluride Nanoparticles, *J. Electron. Mater.* **42** , 898–902(2010).
5. C.C.Liu, F.X.Jiang, M.Y.Huang, B.Y.Lu, R.R.Yue, and J.K.Xu, Free-Standing PEDOT-PSS/Ca3Co4O9 Composite Films as Novel Thermoelectric Materials *J. Electron. Mater*. **40**, 948–52 (2011).
6. M.Zebarjadi, K.Esfarjani, M.S.Dresselhaus, Z.F.Ren, and G.Chen, Perspectives on Thermoelectrics: from Fundamentals to Device Applications, *Energy Environ. Sci*. **5**, 5147–62 (2012).
7. Y.Du, S.Z.Shen, K.Cai, and P.S.Casey, Research Progress on Polymer–Inorganic Thermoelectric Nanocomposite Materials, *Prog. Polym. Sci*. **37**, 820–41(2012).
8. C.Meng, C.Liu, and S.A.Fan, A Promising Approach to Enhanced Thermoelectric Properties Using Carbon Nanotube Networks, Adv. Mater. **22,** 535–9 (2010).
9. Q.H.Wang, D.O.Bellisario, L.W.Drahushuk, R.M.Jain, S.Kruss, M.P.Landry, S.G.Mahajan, S.F.E.Shimizu, Z.W.Ulissi, and M.S.Strano, Low Dimensional Carbon Materials for Applications in Mass and Energy Transport, *Chem. Mater*. **26**, 172–83 (2014).

10. L.Wang, X.Lu, S.Lei, and Y.Song, Graphene-Based Polyaniline Nanocomposites: Preparation, Properties and Applications, *J. Mater. Chem*. **A 2,** 4491–509(2014).
11. C.Yu, Y.S.Kim, D.Kim, and J.C.Grunlan, Thermoelectric Behavior of Segregated-Network Polymer Nanocomposites, *Nano Lett*. **8**, 4428–32 (2008).
12. J.Xiang and L.T.Drzal, Templated Growth of Polyaniline on Exfoliated Graphene Nanoplatelets (GNP) and its Thermoelectric Properties, *Polymer* **53**, 4202–10(2012).
13. B.Abad, I.Alda, P.Díaz-Chao, H.Kawakami, A.Almarza, D.Amantia, D.Gutierrez, L.Aubouy, and M.Martín-González, Improved Power Factor of Polyaniline Nanocomposites with Exfoliated Graphene Nanoplatelets (GNPs), *J. Mater.Chem*. **A 1**, 10450–7 (2013).
14. C.A.Hewitt, A.B.Kaiser, S.Roth, M.Craps, R.Czerw, and D.L.Carroll, Multilayered Carbon Nanotube/Polymer Composite Based Thermoelectric Fabrics, *Nano Lett*. **12,** 1307–10 (2012).
15. D.Kim, Y.Kim, K.Choi, J.C.Grunlan, and C.Yu, Improved Thermoelectric Behavior of Nanotube-Filled Polymer Composites with Poly(3,4-ethylenedioxythiophene) Poly (styrenesulfonate), *ACS Nano* **4,** 513–23 (2010).
16. R.Islam, Chan-Yu-King Roch, J.-F.Brun, C.Gors, A.Addad , M.Depriester, A.Hadj-Sahraoui, and F.Rousse, Transport and Thermoelectric Properties of Polyaniline/Reduced Graphene Oxide Nanocomposites, *Nanotechnology* **25**, 475705-11(2014).
17. N.Neophytou, X.Zianni, H.Kosina, S.Frabboni, B.Lorenzi, and D.Narducci, Simultaneous Increase in Electrical Conductivity and Seebeck Coefficient in Highly Boron-Doped Nanocrystalline Si, *Nanotechnology* **24** (20), 205402 (2013).
18. X.Zianni , D.Narducci, Parametric Modeling of Energy Filtering in Thermoelectric Nanocomposites, *Journal of Applied Physics* **117**, 035102 (2015).
19. F.Gather, C.Heiliger, and P.J.Klar, NeMo: A Network Model Program for Analyzing the Thermoelectric Properties of Meso and Nanostructured Composite Materials, *Progress in Solid State Chemistry* **39**, 97e107 (2011).

Submitted 10.01.2015

L.I. Anatychuk

L.I. Anatychuk, O.V. Nitsovich

Institute of Thermoelectricity NAS and MES of Ukraine1, Nauky Str., Chernivtsi, 58029, Ukraine

O.V. Nitsovich

RESEARCH OF DOUBLE-LAYER THERMOELEMENTS WITH PERIODICALLY PROFILED SURFACE

In the work the results of computer simulation and experimental research of a new type of transverse thermoelements, i.e. a double-layer thermoelement with a periodically profiled surface are presented . It is shown that the deviation of the computed and experimentally obtained values of power and transverse thermoEMF in relation to temperature gradient is no more than 6%. It has been established that the application of the double-layer thermoelements with the periodically profiled surface makes it possible to obtain big values the transverse thermoEMF, power and efficiency in comparison with anisotropic and short-circuited thermoelements.

Key words: thermoelectric generator, micro-CHP, cogeneration

Introduction

Interest to transverse type thermal converters arose in 1970s due to their attractive properties, i.e. the dependence of transverse thermoEMF on geometric dimensions of thermoelements and the absence of commutations with the search of constructions with low-inertia detectors. These circumstances for example give the possibility to increase high-speed performance of the thermoelements with the decrease of their thickness without losses of volt-watt sensitivity. Thus, the transverse type thermal converters are promising to create high-speed thermoelectric devices. However, semiconducting materials for which thermoEMF anisotropy is typical and which are used for making anisotropic thermoelements have relatively low thermoelectric figure of merit. [1-3]. Although it is possible to create high-voltage thermoelements, whose emf is defined by the correlation of geometric dimensions of the oriented single crystals, the power generated by the volume units is less than the standard Seebeck generators possess.

The problem of the new type thermoelements search is topical that would allow to improve the working characteristics of the thermoelectric devices by optimizing the construction and operation modes of the thermoelements. Modern computer technologies make it possible to perform optimization of the new thermoelements constructions and determine their advantages in comparison with other types of thermoelements.

The aim of the present work is the experimental research of the new type thermoelements, i.e. the double-layer thermoelements with the periodically profiled surface, and the comparison of the experimental research result with the computer simulation results.

Simulation of the double-layer thermoelement with the periodically profiled surface

The physical model of the double-layer thermoelement with the periodically profiled surface is shown in Fig. 1.

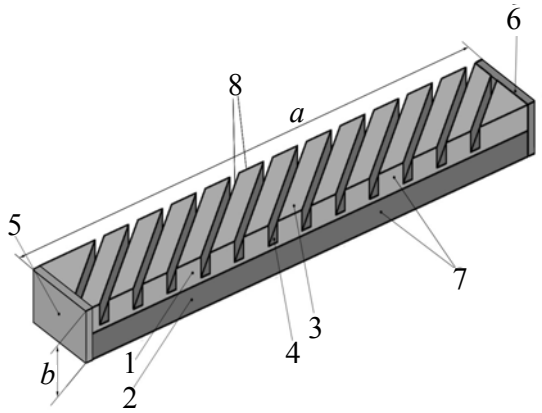

Fig. 1.Double-layer thermoelement with periodically profiled surface [4-5]. 1 – material of p-type conductivity; 2 – material of n-type conductivity; 3 –fins p-type material; 4 – grooved in p-type material; 5, 6 – electrical contacts; 7, 8 –thermoelement sides where sources and heat sinks are located; a, b – thermoelement geometrical dimensions.

The thermoelement consists of the materials of *n*- and *p*-type of conductivity. One of the thermoelement layers has the periodically profiled outer surface with the system of fins and hollows oriented angle wise towards the bar sides 7 and 8, which are thermostated at different temperatures T_1 and T_2. Other outer sides of the thermoelement are in thermal insulation. Electrical contacts are thin metal layers with high electrical conductivity and therefore are practically equipotential within the limits of one contact.

The layered structure with the layers with different thermoelectric properties can be regarded as artificially anisotropic media. Thus, the presence of temperature drop between the corresponding side planes 7 and 8 (Fig. 1) of the double-layer thermoelement with the periodically profiled surface lead to the appearance of electrical current and thermoEMF in the direction perpendicular to the heat flow. This phenomenon is analogous to the transverse Seebeck in the anisotropic medium [3]. Like in the anisotropic thermoelement, the transverse emf value depends on the relation of the thermoelement geometrical dimensions *a/b*. However, in this case the EMF value will not also depend on the thermoelement profiled layers parameters. Therefore, the transverse thermoEMF value $E_\perp$ can be presented in the following way:

$$E_\perp = \Delta\alpha \Delta T \frac{a}{b} f(\varphi, n), \tag{1}$$

where ΔT is the thermoelement temperature difference, $\Delta\alpha$ is the Seebeck coefficients difference of the working body layers material, $f(\varphi, n)$ is the function of the angle of slope of the locking elements (fins) φ towards the thermoelement hot plane and a number of periods of the profiled layers profile *n* per the thermoelement length unit *a*; *b* is the distance between the hot and cold thermoelement planes.

In works [4-5] there are presented the results of the multidimensional optimization of the given thermoelement by computer simulation. At the bottom of this model there lies the method of finite elements where the thermoelement working body is divided into a big number of finite elements, and in each of them the function value is searched which satisfies the set differential equations with corresponding boundary conditions.

The calculations were carried out for the thermoelement from Bi_2Te_3 material [4]. Ftom the computer simulation results it is established that for every geometry and thermoelectric parameters of the thermoelement layers the less the value is d_1 / d_2 (Fig. 2), the more the transverse thermoelement thermoEMF is, and correspondingly its efficiency. The transverse thermoEMF is a non-monotonic function and reaches the maximum at the specific 'porosity' values δ_1/δ_2 (Fig. 2) of the profiled layer.

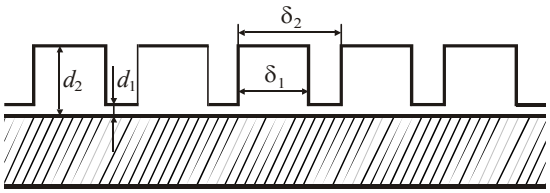

Fig. 2.Geometrical parameters of the thermoelement profiled layer.

In works [4-5] it was shown that for any 'porosity' of the profiled surface the transverse thermoEMF reaches its maximum value when the electrical conductivity value of the profiled layer is twice as much as the lower layer electrical conductivity of the thermoelement.

It was established that the EMF and power values increase with the increase of the relation between the thicknesses of the profiled and non-profiled thermoelement layers. Dependences of emf and the thermoelement electrical power on the relation of geometrical dimensions are monotonic functions that increase with the value growth a/b (Fig. 1).

In order to check the computer simulation results and practical confirmation of the effectiveness of the double-layer thermoelement with the periodically profiled surface the experimental researches were performed. The fulfilled work contained the following stages: synthesis of thermoelectric materials, measurement of the temperature dependences of kinetic parameters of the given materials, obtainment of the double-layer pivots by extrusion methods, manufacturing of samples of the double-layer thermoelement with the periodically profiled surface, emf and power measurements of the obtained double-layer thermoelements.

Manufacturing of double-layer thermoelements with the periodically profiled surface

Thermoelectric materials were synthesized Bi_2Te_3 (75%) + Bi_2Se_3 (25%) and Bi_2Te_3 (30%) + Sb_2Te_3 (70%) (*n*- and *p*-type, correspondingly) in order to produce the samples of artificially anisotropic thermoelements

The following step was to obtain the double-layer pivots of the thermoelectric material, i.e. preforms for future profiled thermoelements by thermomechanic treatment of the synthesized material. The thermomechanic treatment presupposes the plastic deformation (extrusion) of the preforms through the filament extrusion device with the set profile and the following pivot annealing. Such method allows obtaining the calibrated pivots of different cuttings and a profile with the uniform distribution of material properties along its length.

Thus, the double-layer pivots with the transverse cutting 4.1×4.1 mm^2 were obtained by the preform extrusion that consisted of two equal parts of *n*- and *p*-type conductivity (Fig. 3, *a*). The appearance of ready double-layer pivots of the thermoelectric material is shown in Fig. 3, *b*).

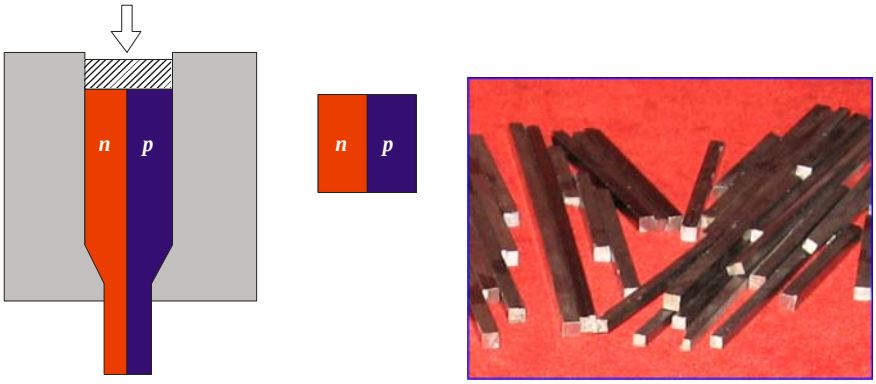

a) *б)*

Fig. 3.Scheme to obtain a double-layer pivot of a thermoelectric material by extrusion (a) and appearance of pivots (b).

In order to define the temperature dependences of the kinetic parameters of the thermoelectric material areas, the samples have been cut out of the obtained pivots that contained the material of only one of the areas. Temperature dependences of the kinetic parameters in the temperature range of 290 ÷ 580 K have been measured for the obtained samples of *n*- and *p*-types of conductivity. The appearance of these dependences and the material thermoelectric figure of merit are presented in Fig. 4.

Further preparation for the production of the thermoelement working body included the cutting of double-layer pivots into the samples of the definite length, profiling of one of the layers and samples polishing.

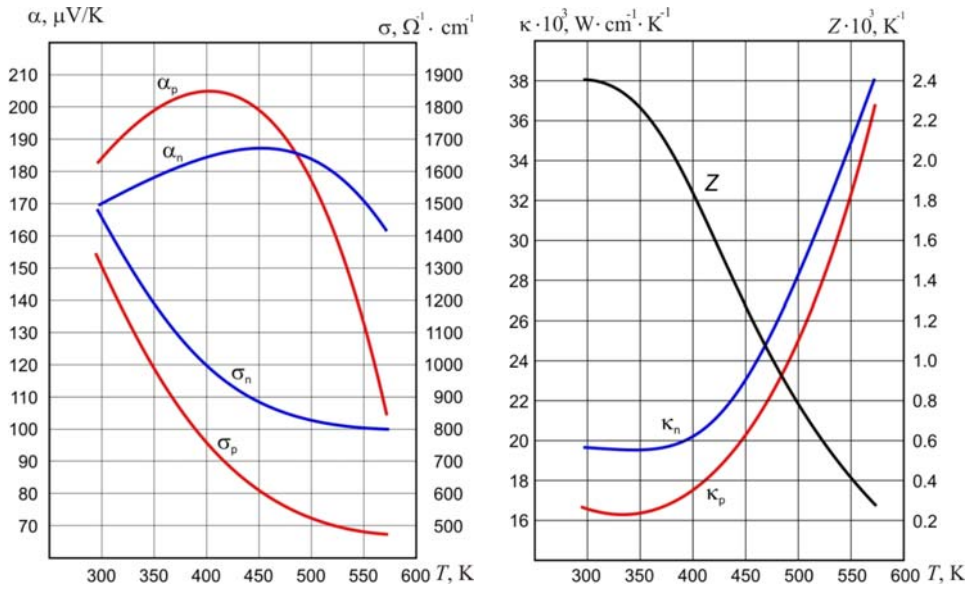

a) *b)*

Fig. 4. Temperature dependences of a thermoEMF coefficient, specific electrical conductivity, specific thermal conductivity of the areas and thermoelectric material figure of merit.

In order to carry out the experimental researches of the double-layer thermoelements with the periodically profiled surface, the samples with the transverse cutting of 4×3.5 мм^2 and the length of 10 mm were produced. The thickness of the solid non-profiled layer is δ_1 = 1.5mm, thickness of the profiled layer is δ_2 = 0.2mm, δ_3 = 2.3mm (Fig. 5). The profiled layer fin is 0.24mm, the groove width is 0.67mm.

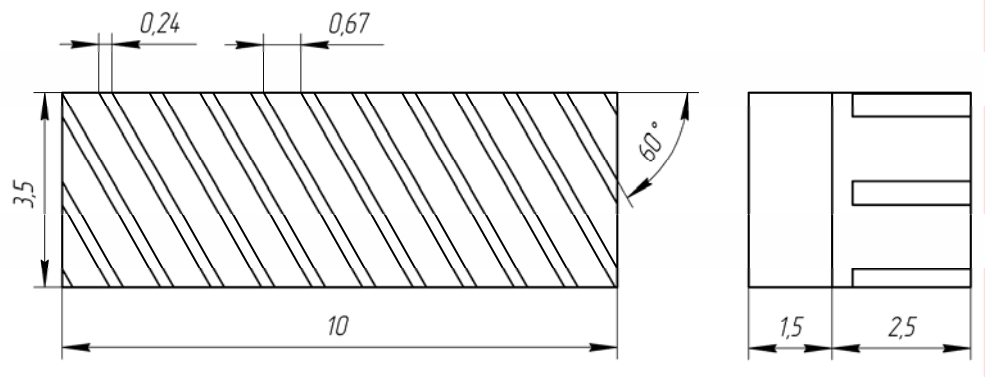

а) *б)*

Fig.5. Front (a)and side (b)projections of the profiled thermoelement.

Appearance of the ready double-layer thermoelement with the periodically profiled surface is shown in Fig. 6.

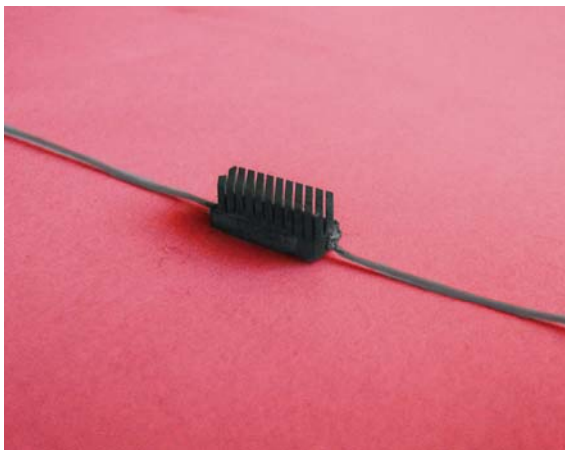

Fig. 6. Double-layer thermoelement with the periodically profiled surface.

Experiment scheme the profiled thermoelements emf and and power measurements

The scheme of the experimental assembly for measuring emf and power of the layered thermoelements is shown in Fig. 7.

The measurements have been carried out for the double-layer thermoelements with the periodically profiled surface 1, which are included into the electrical circuit in series. The hot planes temperature is set by the heater 5 and controlled by the thermocouple 3. The cold planes temperature is controlled by the thermocouples 2 and is set by heat sinks 4, through which the water of the set temperature circulates along the pipe 6. All measurements are carried out in the vacuum conditions of 10^{-5}mm.mercury column.

In Fig. 8 the assembly during the experiment process is shown.

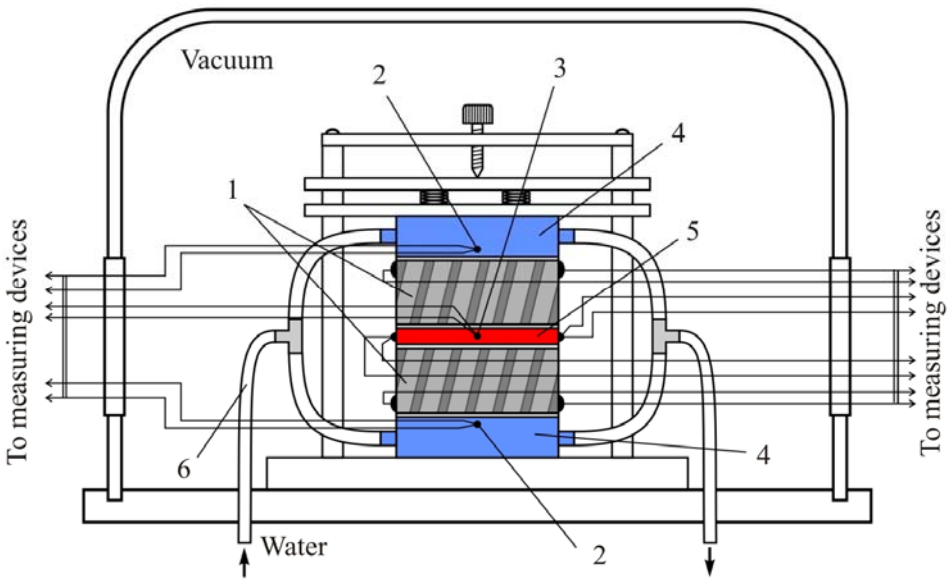

Fig.7. Scheme of the experimental assembly for studying the double-layer thermoelements with the periodically profiled surface: 1 – double-layer thermoelements, 2 –thermocouples for temperature control of cold planes, 3 – thermocouple for temperature control of hot planes, 4 – heat sinks, 5 -heater, 6 – pipe for water supply to heat sinks.

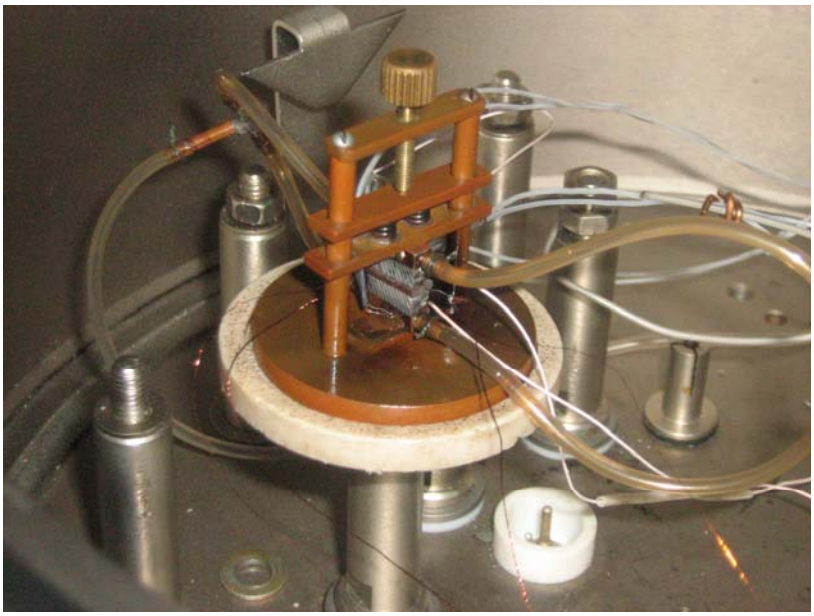

Fig.8.Assembly for emf and power measurements of the double-layer thermoelements with the periodically profiled surface.

Dependences of emf and power of the double-layer thermoelements with the periodically profiled surface on the hot plane temperature were measured during the researches. The cold plane temperature of the thermoelement was 290 K. ThermoEMF of the thermoelements couple was measured in the unloaded circuit.

Results of the experimental researches of the double-layer thermoelements with the periodically profiled surface

In order to define the resistances of the thermoelements and the maximum power W the loading characteristics were taken. The electrical power was fixed at the optimal load of the thermoelements, which is brought to the heater and through the electrical conductors and the thermocouple taking into account the heat losses, and also by the radiation from the side surfaces the heat flow was defined Q, passing through the thermoelements.

In Fig. 9 the appearance of the loading characteristics of the couple of the double-layer thermoelements with the periodically profiled surface connected in series was given obtained during the experiment. As it is seen from the figure the maximum power with the growing temperature drop on the thermoelements is shifted to the side of big resistances that is connected with the electrical conductivity drop of the thermoelement material with the temperature increase.

The measurement results of the transverse thermoEMF dependence on the temperature drop at the thermoelement and the corresponding computer experiments are presented in Fig. 10.

The graphs of dependence of electrical power of the double-layer thermoelement with the periodically profiled surface on temperature drop at the thermoelement are shown in Fig. 11. Deviation from the computed computer simulation and the experimentally defined power values are not more than 6% and are within the limits of the experiment error.

Thus, the double-layer thermoelements with the periodically profiled surface broaden the element thermoelectricity basis and are promising for using as thermal sensitive elements of different heat metric devices.

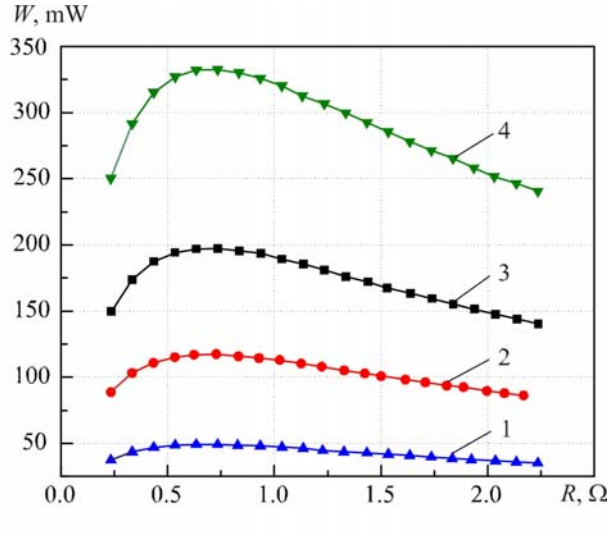

Fig.9.Loading characteristics of the couple of the double-layer thermoelements with the periodically profiled surface connected in series at different temperature drops: 1 - ΔT=84 K; 2 - ΔT=130 K; 3 - ΔT=185 K; 4 - ΔT=285 K.

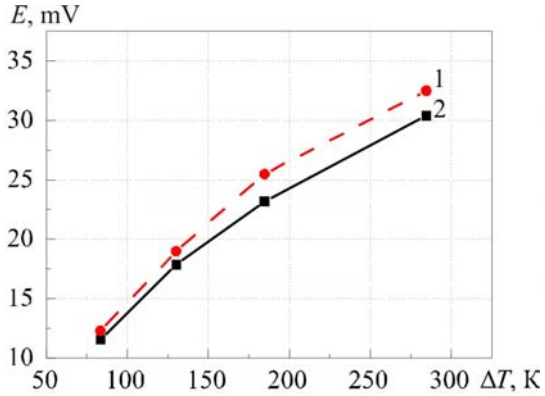

Fig. 10.Dependence of transverse thermoEMF of the double-layer thermoelement with the periodically profiled surface on temperature drop at the thermoelement: 1 – computer experiment, 2 –physical experiment

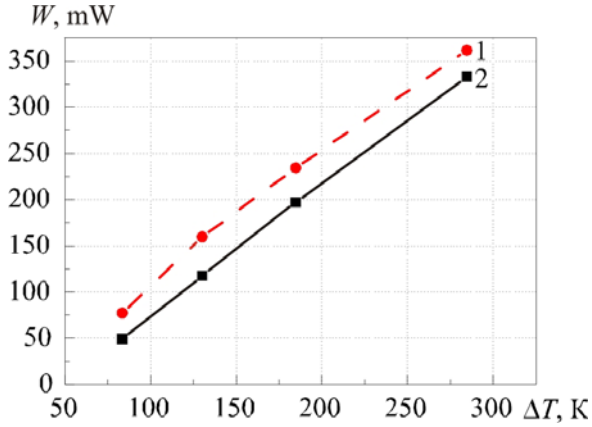

Puc. 11. Dependence of electrical power of the double-layer thermoelement with the periodically profiled surface on temperature drop at the thermoelement: 1 – computer experiment, 2 –physical experiment

They promote the development and creation of the low inertia radiation detectors, heat flow detectors, microcalorimeters and heat meters.

Conclusions

1. There has been produced the double-layer thermoelement with the periodically profiled surface that generated the transverse thermoEMF of 30.4 mV at the temperature drop of 285 K and the power of 332 mV.
2. There have been experimentally confirmed the computer simulation results of the double-layer thermoelement with the periodically profiled surface. It is shown that deviation from the computed and the experimentally defined thermoEMF values are not more than 6%.
3. The application of the double-layer thermoelement with the periodically profiled surface makes it

possible to obtain the greater values of the transverse thermoEMF, power and the efficiency in comparison with the anisotropic and short-circuited thermoelements. This broadens the possibilities of the practical application of the transverse thermoEMFs.

Reference

1. Goldsmid H. J. Artificial Transverse Thermoelements with the Porous Component// Thermoelectricity. – 2008. – №1. – p. 7–12.
2. Goldsmid H. J. Materials for Artificial Transverse Thermoelectric Devices// Thermoelectrics. – 2008. – №4. – p. 42–51.
3. Anatychuk L.I. Thermoelements and Thermoelectric Devices: Directory. – K.: Nauova Dumka, 1979. – 768p.
4. L.I. Anatychuk, O.J. Luste, O.V. Nitsovich. Computer simulation of energy conversion in a double-layer thermolement with periodically profiled surface // Journal of Thermoelectricity. – 2007. – №2– C.73-80.
5. Anatychuk L. I., Luste O. Ya., Nitsovich O. V. Temperature Dependences Of Parameters of A Double-Layer Thermoelement with the Periodically Profiled Surface // Thermoelectrics. – 2008. – №2. – p .32-40.

Submitted 26.02.2015

T. Fröhlich, M. Hohmann, M. Schalles

Technische Universität Ilmenau, Institute for Process Measurement and Sensor Technology, POB 100565, 98684 Ilmenau

CALIBRATION BENCH FOR HEAT FLUX SENSORS

A new calibration bench was developed at the Institute for Process Measurement and Sensor Technology of Technische Universität Ilmenau to calibrate heat flux sensors (HFS). The bench provides well known temperatures at both sides of the HFS, from which the heat flux can be determined. The temperatures are determined using a method known from the calibration of contact surface thermometers. By means of the values measured by thermocouples distributed along the central axis of two homogenization blocks, the surface temperatures of each homogenization block, and thereby the surface temperatures of the HFS, are extrapolated. The extrapolated surface temperatures are controlled in a manner that the difference between the two temperatures changes in the range of 0 mK to 200 mK. Using these temperature differences and the sensor signal, the offset and the sensitivity of the HFS can be determined. HFS based on thermopiles and HFS based on the transversal seebeck-effect were constructed calibrated at the bench.

Key words: heat flux sensor, calibration, surface temperature

Introduction

Heat flux sensors (HFS) for heat flux of conductive origin are usually calibrated at calibration benches using the guarded-hot-plate-method [1]. This method requires a known heat flux through the sensor under test. This heat flux is usually provided by a heater on one side of the HFS, measured by means of the temperature difference over a plate with known geometry and thermal conductivity and dissipated in a heat sink on the other side of the HFS. One of the main requirements for this method is a one-directional heat flux from the heat source to and through the sensor under test, which can only imperfectly be provided. The calibration bench presented in this paper uses a different approach. It uses the determination of the surface temperature of the sensor under test to investigate its characteristics.

Design and operating principle

Calibration bench

The calibration bench is an axial symmetrical construction consisting of two meander-shaped heaters and two cylindrical homogenization blocks (steel 1.4301) with integrated thermocouples (TCs) type K, surrounded by an insulation made of alkaline-earth silicate wool (Fig. 1). The homogenization blocks are 76 mm in diameter and 25 mm in height. The geometry of the air gap between the blocks depends on the geometry of the sensor under test (the HFS). The power of the heaters on top of the upper and at the bottom of the lower homogenization block can be controlled individually and heat the bench in a temperature range from 20 °C to 400 °C.

The three TCs in each homogenization block are used to extrapolate to the blocks surface temperature using a quadratic polynomial approach. This method is known from the calibration of contact surface thermometers [2]. Using this method, the surface temperatures of the homogenization blocks and of the HFS respectively, are determined and used as controlled variable. By means of the heaters, the temperatures are controlled in a manner that the difference of the extrapolated surface temperatures changes from $\Delta T = 0$ K to $\Delta T = \pm 200$ mK. The temperature difference of 200 mK was found to be great enough to get an evaluable signal and small enough to get a not to high deformation of the thermal field.

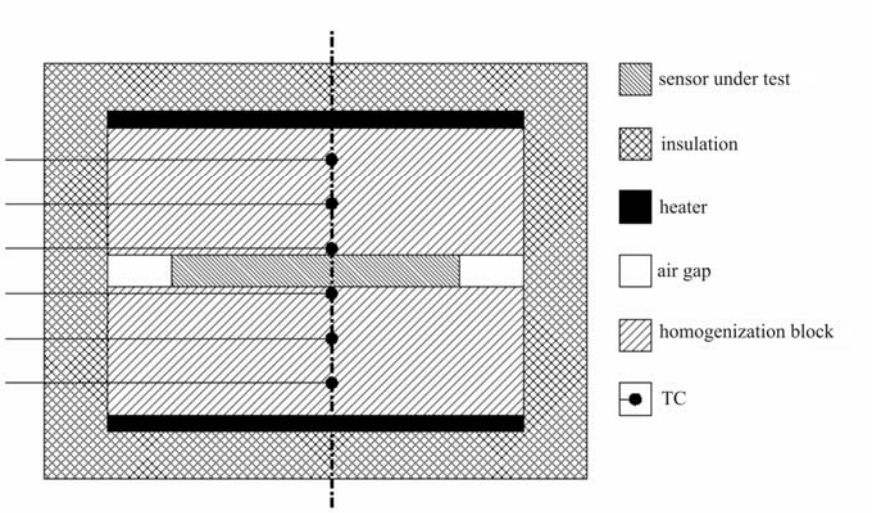

Fig. 1. Design of the calibration bench.

Operating principle

The aim of the calibration is to determine the sensitivity S and the offset U_0 of the characteristic (1) of the HFS, where ΔT is the temperature difference between top and bottom of the HFS.

$$U_{\mathrm{HFS}} = U_0 + S \cdot \Delta T \tag{1}$$

Each of the temperatures has errors due to temperature measurement and the unknown temperature field across the surface of the HFS (2).

$$U_{\mathrm{HFS}} = U_0 + S \cdot [(T_{\mathrm{upper}} + E_{\mathrm{upper}}) - (T_{\mathrm{lower}} + E_{\mathrm{lower}})] \tag{2}$$

To compensate the influence of these errors, two different temperature differences T_{upper}-T_{lower} (a and b) are used to determine $S(\Delta T)$. Assuming that the errors E are constant or change negligibly, $S(\Delta T)$ can be determined using the two signals U and the four temperatures T (3).

$$\begin{aligned} U_{\mathrm{HFS,a}} &= U_0 + S \cdot [(T_{\mathrm{upper,a}} + E_{\mathrm{upper}}) - (T_{\mathrm{lower,a}} + E_{\mathrm{lower}})] \\ U_{\mathrm{HFS,b}} &= U_0 + S \cdot [(T_{\mathrm{upper,b}} + E_{\mathrm{upper}}) - (T_{\mathrm{lower,b}} + E_{\mathrm{lower}})] \\ S(\Delta T) &= \frac{U_{\mathrm{HFS,a}} - U_{\mathrm{HFS,b}}}{(T_{\mathrm{upper,a}} - T_{\mathrm{lower,a}}) - (T_{\mathrm{upper,b}} - T_{\mathrm{lower,b}})} \end{aligned} \tag{3}$$

To determine the offset U_0, the HFS has to be flipped at one temperature or the polarity of the electrical connection to the measuring device has to be reversed (4).

$$U_{\mathrm{HFS,plus}} = U_0 + S \cdot [(T_{\mathrm{upper}} + E_{\mathrm{upper}}) - (T_{\mathrm{lower}} + E_{\mathrm{lower}})]$$
$$U_{\mathrm{HFS,minus}} = U_0 + S \cdot [(T_{\mathrm{lower}} + E_{\mathrm{lower}}) - (T_{\mathrm{upper}} + E_{\mathrm{upper}})] \quad (4)$$
$$U_0 = \frac{U_{\mathrm{HFS,plus}} + U_{\mathrm{HFS,minus}}}{2}$$

To get the sensitivity as a function of heat flux $\dot{q}$, the one-dimensional formulation of Fourier's law (5) is used, where λ is the thermal conductivity. With the assumptions of one-dimensional heat conduction and a constant temperature gradient across the length *l* of the sensor one gets (6).

$$\dot{q} = -\lambda \nabla T \quad (5)$$

$$\dot{q} = -\frac{\lambda}{l} \Delta T \quad (6)$$

Using equations (3) and (6), the sensitivity $S(\dot{q})$ is given by equation (7). The thermal conductivity and the thickness are temperature-dependent, but their changes in the small temperature interval of 200 mK can be neglected.

$$S(\dot{q}) = \frac{l}{\lambda} \cdot \frac{U_{\mathrm{HFS,a}} - U_{\mathrm{HFS,b}}}{(T_{\mathrm{upper,a}} - T_{\mathrm{lower,a}}) - (T_{\mathrm{upper,b}} - T_{\mathrm{lower,b}})} \quad (7)$$

Sensors under test

The sensors under test were constructed at the Institute for Process Measurement and Sensor Technology of the Technische Universität Ilmenau. Two principles were used: one design using thermopiles, which is a well-known principle for HFS [3], and one design using the transversal seebeck-effect [4], [5]. Both types of sensors were constructed with the same geometrical parameters, disks with 54 mm in diameter and 1.5 mm in height.

HFS using thermopiles

The sensors consist of two rings of TCs type E, which are thermally connected in parallel and electrically connected in series. These so called thermopiles have 25 junctions at the inner and 35 junctions at the outer ring and are mounted to a backing made of glass ceramic ($\lambda = 1.72$ W m^{-1} K^{-1}, Fig. 2). To investigate the influence of the filling (heat conducting compound, $\lambda = 3$ W m^{-1} K^{-1}), sensors with and without filling were constructed.

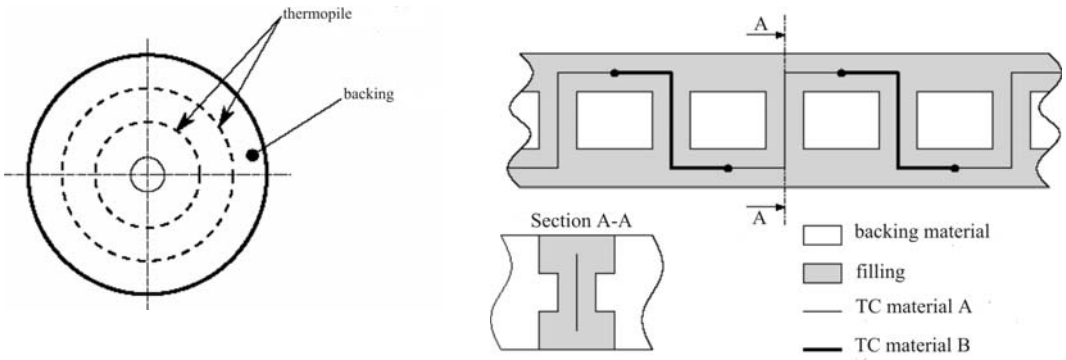

Fig. 2. Design of the HFS and cross-section along one thermopile.

The theoretical sensitivity $S(\dot{q})$ (8) depends on the sensitivity $S_{\mathrm{TC}}(T)$ of the TC type E, the distance between the junctions l_{J}, the thermal conductivity and the number n of TCs in the thermopile [3]. The sensitivity $S(\Delta T)$ only depends on $S_{\mathrm{TC}}(T)$ and n (9).

$$S(\dot{q}) = \frac{n \cdot S_{\mathrm{TC}}(T) \cdot l_{\mathrm{J}}}{\lambda} \tag{8}$$

$$S(\Delta T) = n \cdot S_{\mathrm{TC}}(T) \tag{9}$$

To estimate the theoretical sensitivity, the equivalent electrical circuit [2] was used. With this model and the values for $S_{\mathrm{TC}}(T)$ from [6] for different temperatures the sensitivity was estimated (Table 1).

Table 1

Theoretical sensitivity of the HFS using thermopiles.

	60 °C		100 °C		150 °C	
thermopile	$S(\Delta T)$, μVK^{-1}	$S(\dot{q})$, $\mu VW^{-1}m^2$	$S(\Delta T)$, μVK^{-1}	$S(\Delta T)$, μVK^{-1}	$S(\dot{q})$, $\mu VW^{-1}m^2$	$S(\Delta T)$, μVK^{-1}
25 with filling	56.96	406.83	58.61	56.96	406.83	58.61
35 with filling	79.66	568.28	81.96	79.66	568.28	81.96
25 without filling	40.42	194.97	41.59	40.42	194.97	41.59
35 without filling	56.51	272.20	58.14	56.51	272.20	58.14

HFS using transversal Seebeck-effect

The sensors main part is a solid disk made of a stack of *NiCr*- and *CuNi*-layers. These metals (material for TC-type E) are welded by means of diffusion welding and cut into disks under an angle of 45° (Fig. 3). In this artificial anisotropic material, the Seebeck coefficient y and the thermal conductivity λ are tensors of second order and described by (10) and (11), where $\lambda_{\parallel}$ and $\sigma_{\parallel}$ represent the material properties along, $\lambda_{\perp}$ and $y_{\perp}$ the properties perpendicular to the main axis of the stack [5].

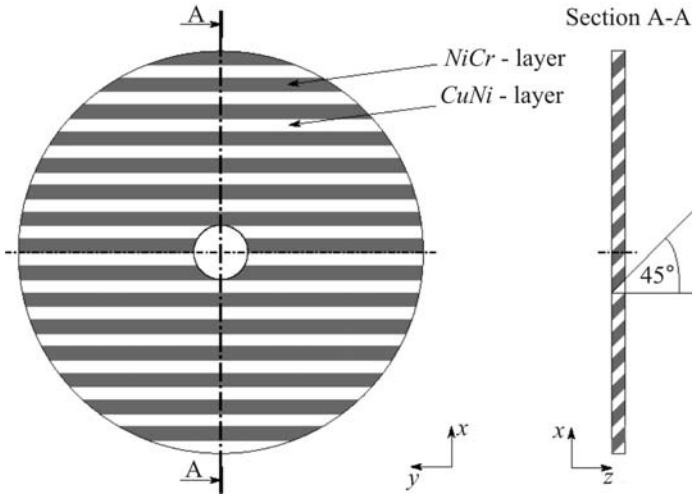

Fig. 3. Design of the HFS made of artificial anisotropic material.

$$\sigma = \begin{bmatrix} \sigma_P \cos^2\alpha + \sigma_\wedge \sin^2\alpha & 0 & \frac{1}{2}(\sigma_P - \sigma_\wedge)\sin(2\alpha) \\ 0 & \sigma_P & 0 \\ \frac{1}{2}(\sigma_P - \sigma_\wedge)\sin(2\alpha) & 0 & \sigma_P \cos^2\alpha + \sigma_\wedge \sin^2\alpha \end{bmatrix} \tag{10}$$

$$\lambda = \begin{bmatrix} \lambda_{\parallel} \cos^2\alpha + \lambda_\perp \sin^2\alpha & 0 & \frac{1}{2}(\lambda_{\parallel} - \lambda_\perp)\sin(2\alpha) \\ 0 & \lambda_{\parallel} & 0 \\ \frac{1}{2}(\lambda_{\parallel} - \lambda_\perp)\sin(2\alpha) & 0 & \lambda_{\parallel} \cos^2\alpha + \lambda_\perp \sin^2\alpha \end{bmatrix} \tag{11}$$

The signal of the sensor is the electric field E generated by the thermopower inside the sensor (12) integrated along the direction of the measured voltage, x in this case (13).

$$E = \sigma \cdot \nabla T \tag{12}$$

$$U_x = \int_0^d \left((\sigma_{\parallel} \cos^2\alpha + \sigma_\perp \sin^2\alpha)\frac{\partial T}{\partial x} + \frac{1}{2}(\sigma_{\parallel} - \sigma_\perp)\sin(2\alpha)\frac{\partial T}{\partial z} \right) dx \tag{13}$$

Assuming one-dimensional heat conduction in z-direction with a constant gradient, one gets the sensor signal as a function of the temperature difference ΔT in *z*-direction (14).

$$U_x = \frac{1}{2}(\sigma_{\parallel} - \sigma_\perp)\sin(2\alpha)\frac{d}{l}\Delta T_z \tag{14}$$

Hence, the theoretical sensitivity $S(\Delta T)$ depends on the anisotropy of the thermopower $(\sigma_{\parallel} - \sigma_\perp)$, the cutting angle α, the diameter *d* and the thickness *l* of the sensor. The theoretical sensitivity $S(\dot{q})$ additionally depends on the thermal conductivity λ in *z*-direction.

$$S(\Delta T) = \frac{U_x}{\Delta T_z} = \frac{1}{2}(\sigma_{\parallel} - \sigma_\perp)\sin(2\alpha)\frac{d}{l} \tag{15}$$

$$S(\dot{q}) = \frac{U_x}{\dot{q}_z} = \frac{(\sigma_{\parallel} - \sigma_\perp)\sin(2\alpha)d}{(\lambda_{\parallel} \cos^2\alpha + \lambda_\perp \sin^2\alpha)l} \tag{16}$$

Differently from the HFS using thermopiles, the theoretical sensitivity of this design depends on more material properties. In addition to the ones already mentioned, the electrical resistivity is used to determine $\sigma_{\parallel}$ [5]. Since these material properties are not exactly known and several different values can be found in references, a Monte-Carlo simulation of the sensitivity was carried out using the values listed in Table 2 and a variation of $\pm 20\,\%$ for each of them.

Table 2

Material properties of NiCr and CuNi [2], [7], [8], [9].

material	σ, μVK^{-1}	λ, $Wm^{-1}K^{-1}$	γ, $\mu\Omega^{-1}m^{-1}$
NiCr	28.07	19.0	1.4
CuNi	-42.05	25.29	2.0

The results of this simulation are minimal and maximal expected values for the sensitivity at the three temperatures, which are shown in Table 3. The high difference of the minimal and maximal expected values can be explained by the nonlinear relation of the material properties in the model (10). The calculated values define a range, in which the calibration results should be lying to be considered as valid.

Table 3

Minimal and maximal theoretical sensitivity of the HFS using transversal Seebeck effect.

	60 °C		100 °C		150 °C	
value	$S(\Delta T)$, μVK^{-1}	$S(\dot{q})$, $nVW^{-1}m^2$	$S(\Delta T)$, μVK^{-1}	$S(\dot{q})$, $nVW^{-1}m^2$	$S(\Delta T)$, μVK^{-1}	$S(\dot{q})$, $nVW^{-1}m^2$
minimum	0.46	0.06	0.52	0.07	0.56	0.08
maximum	421.80	59.89	441.74	62.83	467.90	66.44

Properties of the bench

Stability of the surface temperatures

Each of the extrapolated surface temperatures is controlled by a PID-controller respectively. These controllers are able to hold the setpoint, but there are oscillations with a period of about 300 s and a magnitude less than 30 mK around the setpoint (Fig. 4). These oscillations are caused by the periodic change of the temperature in the laboratory due to air condition, cross-sensitivity of the two controllers and the nonexistent active cooling. Nevertheless this quality of the controlled temperatures is sufficient for calibration, since integration intervals of 600 s are possible during the calibration process.

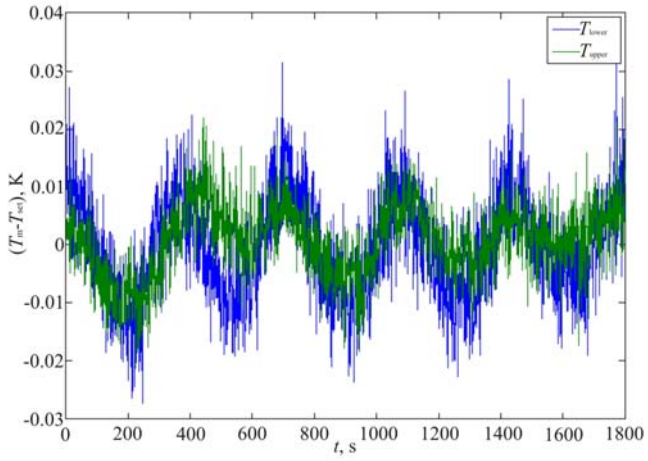

Fig. 4. Temperature differences between the setpoint temperature T_{set} and the measured surface temperatures T_m of the upper and the lower homogenization block in steady state.

Axial temperature distribution

Fig. 5 shows the axial temperature distribution in the blocks during the calibration at $T_{set} \sim 100$ °C with a temperature difference of T_{upper}-$T_{lower} = 100$ mK. In each block the temperature distribution follows a quadratic function. The deviation of a linear distribution is caused by the heat exchange with

the other block respectively and the heat losses through the non-ideal insulation. The temperature distribution across both blocks is an indication of the influence of thermal contact resistances between the HFS and the blocks surfaces.

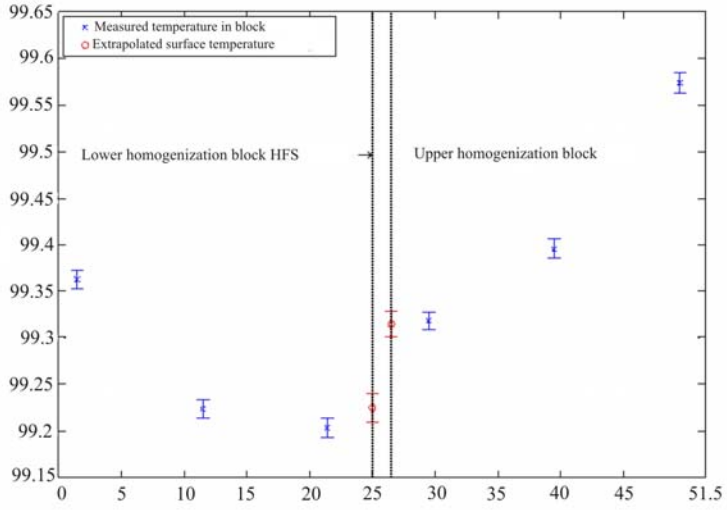

Fig. 5: Axial temperature distribution from height h=0 mm (bottom) to h=51.5 mm (top) of the bench at T_{set} ~ 100 °C and the temperature difference T_{upper}-T_{lower} = 100 mK. The error bars show the standard deviation of the temperatures (2500 data points).

Homogeneity of the temperature field

To estimate the homogeneity of the temperature field across both sides of the HFS, a TC was used to measure the surface temperatures at several points. For this, a dummy of a HFS with a radial groove was manufactured in which the TC was inserted. For each measurement series, the dummy was rotated 45°. At every angular step, the TC was moved in the groove from the center outwards in 2.5 mm-steps. This measurement was performed at steady state of the surface temperatures at 60 °C. The results in show, that the absolute temperature difference across the each surface has a magnitude of 160 mK.

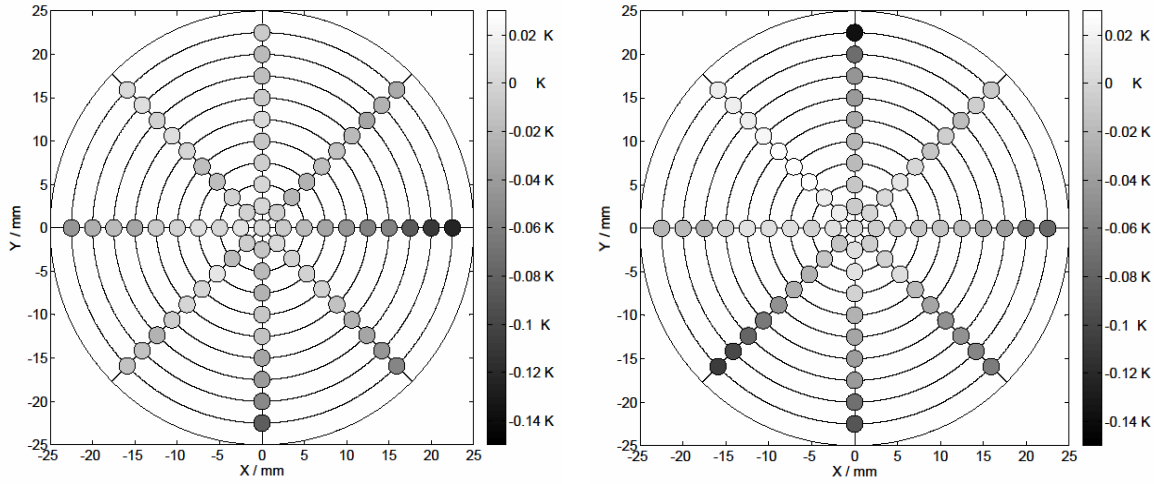

a) *b)*

Fig. 6. Temperature field at the surface of the upper (a) and the lower (b) homogenization block at T_{set} = 60 °C, the difference to the extrapolated surface temperature at the center is shown.

The difference of the measured temperature field compared to a typical one with gradient in radial direction can be explained by the shape of the heaters. Due to the non-uniform heat input, the temperature field gets deformed, which has been simulated with the Finite Element Method (Fig. 7).

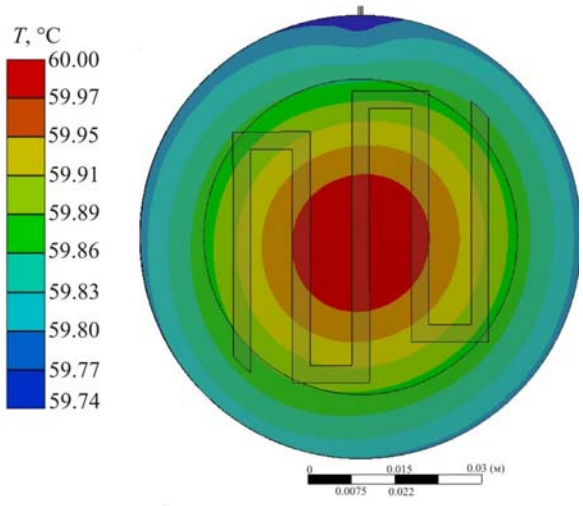

Fig. 7. FEM-Simulation of the temperature field due to the non-uniform heat input. The homogenization block, the heater and the position of the HFS are shown.

Calibration results

HFS using thermopiles

Due to the long integration interval at every calibration point, the calibration at one temperature takes about 5 h. During this time, 5 calibration points are measured (Figr. 8, Fig. 9). To determine the sensitivity, these points are taken to fit a polynomial of first degree in a least-squares-manner, which fulfills equation (3). The offset results from temperature differences due to the calibration of the TC inside the normalization blocks.

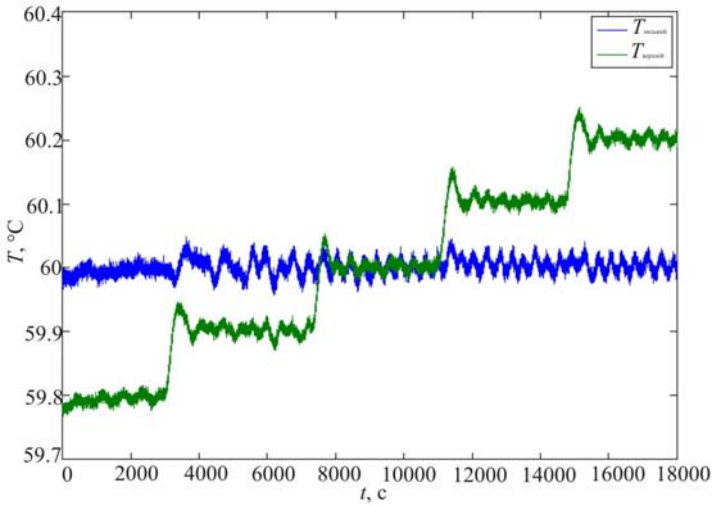

Figr. 8. Temperatures during the calibration around 60 °C.

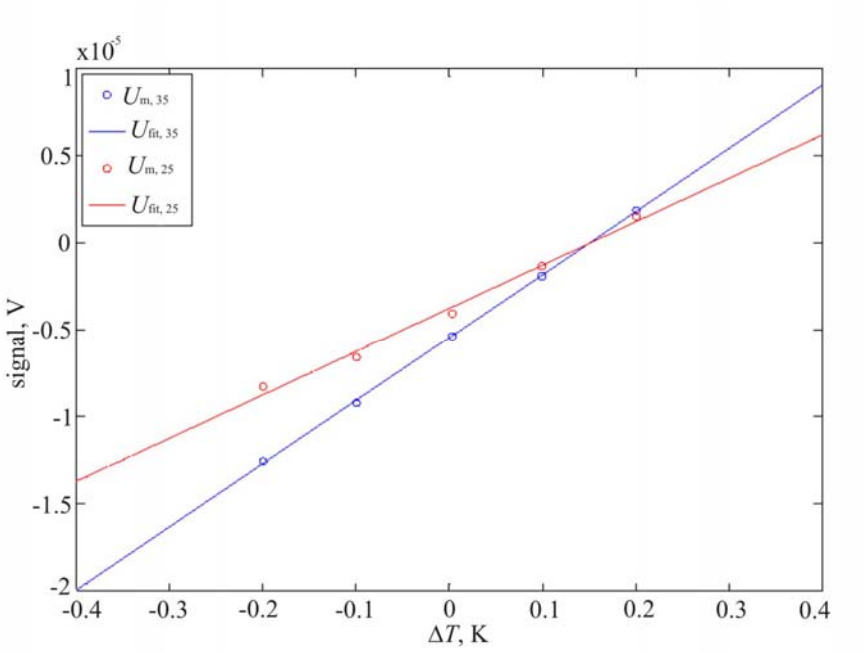

Fig. 9. Sensor signals during the calibration around 60 °C. U_m is the measured signal of each thermopile, U_{fit} is the approximated polynomial of first grade from which the sensitivity is taken.

The high differences between the theoretical values and the measured ones (Table 4) are caused by the thermal resistances between the HFS and the blocks surfaces. These resistances can hardly be measured, but are also present at the real application. Due to this, the measured sensitivities can be used in the application if the surface properties and the contact forces are comparable to the calibration circumstances.

Table 4

Measured sensitivity of the HFS using thermopiles.

	60 °C		100 °C		150 °C	
thermopile	$S(\Delta T)$, μVK^{-1}	$S(\dot{q})$, $\mu VW^{-1}m^2$	$S(\Delta T)$, μVK^{-1}	$S(\dot{q})$, $\mu VW^{-1}m^2$	$S(\Delta T)$, μVK^{-1}	$S(\dot{q})$, $\mu VW^{-1}m^2$
25 with filling	25.52	182.27	28.56	203.95	29.91	213.59
35 with filling	36.63	261.31	36.64	261.37	38.66	275.80
25 without filling	27.19	131.15	30.22	145.75	32.34	155.98
35 without filling	41.14	198.17	46.60	224.43	50.31	242.31

The relative error E_r (17) of the measured sensitivity S_m to the theoretical S_t (Table 5) shows, that the relative error gets smaller with higher temperature and if there is no filling in the HFS. This indicates the influence of the contact resistance. These contact resistances have a higher influence on the sensitivity than the heat conduction trough air or ceramic filler. Additionally, the influence of heat transfer by radiation becomes greater at higher temperatures when there is only air between the thermopiles and the surface of the homogenization blocks.

$$E_r = \frac{S_m - S_t}{S_t} \cdot 100 \qquad (17)$$

Table 5

Relative error of the sensitivity.

	60 °C	100 °C	150 °C
thermopile	E_r / %	E_r / %	E_r / %
25 with filling	-55.20	-51.27	-50.59
35 with filling	-54.02	-55.30	-54.32
25 without filling	-32.73	-27.34	-24.70
35 without filling	-27.20	-19.85	-16.22

HFS using transversal Seebeck effect

The same temperature sequence as shown in Figr. 8 was used for this calibration. The results also show an offset due to the calibration of the TC inside the normalization blocks. The measured values for the sensitivity are shown in Table 6, where the material properties of Table 2 were used to calculate $S(\dot{q})$. The values are in the expected range and an increasing sensitivity with increasing absolute temperature can be seen.

Table 6

Measured sensitivity of the HFS using transversal Seebeck effect.

60 °C		100 °C		150 °C	
$S(\Delta T)$ / μVK^{-1}	$S(\dot{q})$ / $nVW^{-1}m^2$	$S(\Delta T)$ / μVK^{-1}	$S(\Delta T)$ / μVK^{-1}	$S(\dot{q})$ / $nVW^{-1}m^2$	$S(\Delta T)$ / μVK^{-1}
4.93	0.68	5.50	0.75	6.09	0.83

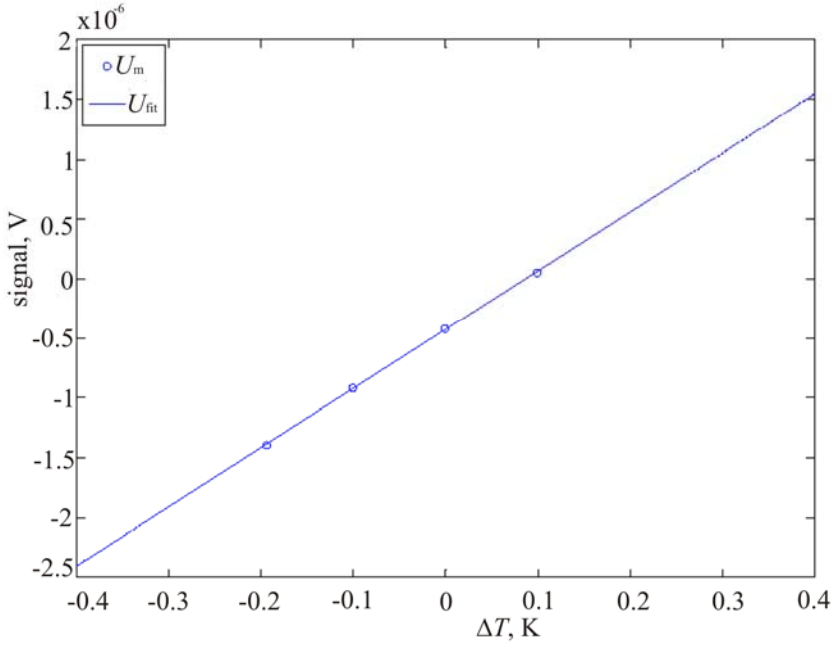

Fig. 10: Sensor signals during the calibration around 60 °C. U_m is the measured signal, U_{fit} is the approximated polynomial of first grade from which the sensitivity is taken.

Conclusion and outlook

A new bench for the calibration of heat flux sensors was developed, built up and tested. The thermal properties of the bench like stability of the temperature and axial and radial temperature distribution were measured. The results show, that the bench can be used to calibrate HFS with small heat fluxes. Two types of sensors were calibrated, the measured sensitivities compared to the theoretical ones show that every measurement with a HFS has to be checked carefully due to thermal contact resistances. A first set of calibrations from 60 °C to 150 °C has already been carried out, the test with temperatures up to 400 °C is in progress.

Acknowledgement. The authors would like to thank the German Federal Ministry of Education and Research (BMBF) for the financial support of the VIP-Project "TempKal", in which context this calibration bench was developed.

References

1. F.Arpino, M.Dell'Isola, G.Ficco, L.Iacomini, V.Fernicola, Design of a Calibration System for Heat Flux Meters, International Journal of Thermophysics **32**(11-12), 2727-2734 (2011).
2. F.Bernhard (Ed.), Technische Temperaturmessung (Berlin: Springer-Verlag, 2004).
3. P.R.N.Childs, J.R.Greenwood, C.A.Long, Heat Flux Measurement Techniques. In: Proceedings of the Institution of Mechanical Engineers, Part C: Journal of Mechanical Engineering Science (1999), p. 655-677
4. Andrey V.Mityakov, Sergey Z.Sapozhnikov, Vladimir Y.Mityakov, Andrei A.Snarskii, Maxim I.Zhenirovsky, Juha J.Pyrhönen, Gradient Heat Flux Sensors for High Temperature Environments, Sensors and Actuators A: Physical **176**,1-9 (2012).
5. K.Fischer, C.Stoiber, A. Kyarad, H.Lengfellner, Anisotropic Thermopower in Tilted Metallic Multilayer Structures, Applied Physics A: Materials Science & Processing **78,** 323-326 (2004).
6. DIN EN 60584-1: Thermopaare. Teil 1: Grundwerte der Thermospannung (1996)
7. ASTM, Standard Specification and Temperature-Electromotive Force (EMF) Tables for Standardized Thermocouples, 2003.
8. O.Madelung and G.K.White (Ed.): Landolt-Börnstein, Zahlenwerte und Funktionen aus Naturwissenschaften und Technik: Gruppe III: Kristall- und Festkörperphysik. Bd. 15: Metalle: Elektronische Transportphänomene, Teilband c: Wärmeleitfähigkeit von reinen Metallen und Legierungen (Berlin Heidelberg New York Paris Tokyo Hong Kong Barcelona Budapest: Springer, 1991).
9. J.R.Davis, Heat-Resistant Materials, ASM Specialty Handbook (Materials Park Ohio: ASM International, 1997).

Submitted 19.02.2015

Yu.M. Lobunets

Yu.M. Lobunets

Institute of Thermoelectricity NAS and MES of Ukraine
1, Nauky Str., Chernivtsi, 58029, Ukraine

HEAT EXCHANGE-TYPE TEG FOR MICRO-CHP

The application potential of heat exchange-type TEG in micro-CHP (combined heat and power) schemes is discussed. The outlook for using such TEG is outlined.
Key words: thermoelectric generator, micro-CHP, cogeneration

Introduction

Combined heat and power production (cogeneration) is one of the most efficient trends in energy saving that has an exceptionally wide application field. This trend is based on the fact that all thermal energy consumers use low-grade heat carriers (hot water, saturated steam), while production of such heat carriers is based on high-grade sources of energy (organic fuel combustion products). Fraction of thermal energy used in the high-temperature range for electric energy generation permits to increase considerably the efficiency of fuel utilization and reduce the working cost of thermal and electric energy. First and foremost, cogeneration schemes found application in industry where all prerequisites existed to this end, and then started to extend to municipal engineering, one of the largest consumers of organic fuel. Primarily it is related to district heating systems where it is possible to complete water heaters with gas steam or gas reciprocating units. At the same time, methods for economic encouragement of resource-saving technologies are improved. Scientific and technical progress in the field of using renewable energy sources (wind, solar, geothermal, biomass energy) inevitably results in the expansion and practical implementation of the concept of decentralized power supply, where on an equal basis with heavy power plants, of considerable importance are low-power distributed sources of electric energy working for a unified power grid. In the most developed countries this process is encouraged by special legislative acts and pricing system that assure the cost effectiveness of such sources of energy and the respective inflow of investments to this field, which also stimulates development of new technologies and equipment for cogeneration microsystems (according to the rules adopted in the EU, micro-CHP include systems of less than 50 kW power output). As an example, we refer to micro-CHP systems based on domestic gas boilers using for their operation the Diesel [1], Stirling [2] and Rankine [3] cycles. An exceptionally wide market for such systems in the European Union countries, USA and Japan is supported by legislative acts that permit to supply generated power to electric grid according to tariffs assuring equipment payback. Preliminary analysis of technical and economic features of such systems provides an opportunity to predict that thermoelectric generators also can find their niche in this market.

Fig.1 shows a cogeneration scheme of a gas boiler operated with the use of organic Rankine cycle (ORC) [3]. High-temperature combustion products of gas fuel 1 come to steam generator 2, where overheated steam of organic heat carrier 3 is generated, which actuates turbo-generator with the

rotor wheel of spiral type 4. Then the steam comes to a condenser 5 where it gives heat to heat carrier of heating system and is condensed. Condensate comes back to steam generator and the cycle is closed. A mandatory requirement for this scheme is the availability of storage tank in heating system, assuring a more uniform generator operating mode.

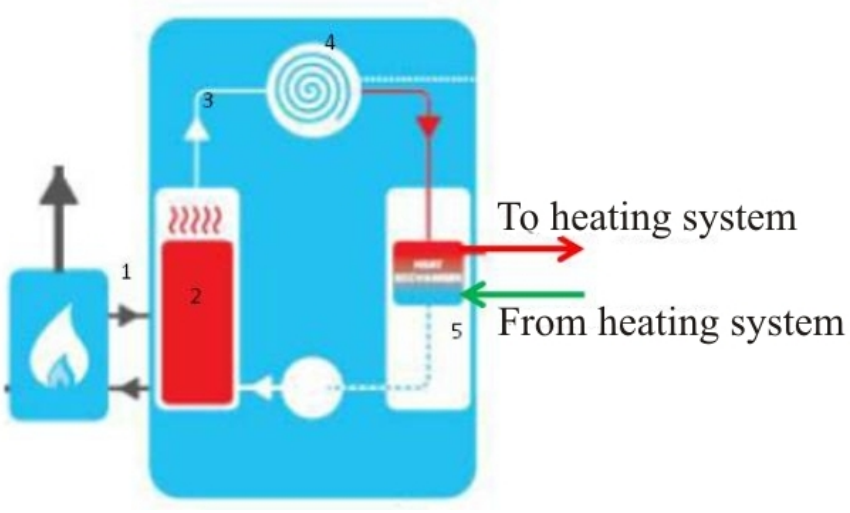

Fig.1. Schematic of micro-CHP with ORC [3]

Such Flow Energy –manufactured micro-CHP [3] has the following characteristics:

- thermal power – 16.9 kW;
- electric power - 1000 W;
- average productivity – 2000 kW-h/year;
- hot water delivery to heating system – 0.217 kg/s;
- maximum water temperature - 82°C;
- gas flow rate – 1.8 m^3/h;
- thermal efficiency – 92%;
- retail cost - 3675£ (5700$US*)*;
- electricity tariff 0.1345 £/kW-h (0.2$US/kW-h) [4];

The above data imply that coefficient of thermal into electric energy conversion for this micro-CHP is about 6%, that is, parameters of the generating part correlate completely with the level of modern TEG parameters. Below we consider one of possible schemes of TEG for micro-CHP and give the results of analysis of its technical and economic characteristics.

Scheme of TEG for micro-CHP

Schematic of micro-CHP/TEG under study is given in Fig.2. Unlike that considered above, it requires minimal modification of the boiler and can be adapted to any gas boiler through change of its temperature conditions. Gas boiler 1 heats intermediate heat carrier to temperature t_{ho}, following which the latter comes to the hot channels of heat exchange-type TEG 2 [5]. Heat carrier from the storage tank of heating system 3 with temperature t_{xo} comes to the cold channels of TEG, where it is further heated to the necessary temperature t_{xe}, following which it returns to heating system. Part of heat flux flowing between heat carriers is converted into electric energy. Inverter 4 must be also used in the scheme to convert direct current of TEG to alternating current of required parameters.

Fig. 2. Schematic of micro-CHP/TEG

Let us consider conditions whereby such micro-CHP/TEG can compete with the scheme based on the use of ORC. It is evident that the main requirement for this is to assure technical and economic features that correspond to the above and guarantee acceptable equipment repayment periods. The basic data for the analysis of micro-CHP/TEG can be defined as follows:

- electric power N_o = 1000 W;
- thermal power Q_o =16,9 kW;
- hot heat carrier temperature t_{ho} = 250°C;
- TEG input water temperature t_{xo} = 65°C;
- maximum TEG unit cost $Price_{max}$ = 1200 $US/kW.

Hot heat carrier temperature was selected on the basis of using low-temperature thermoelectric material (Bi_2Te_3) in the TEG. Maximum unit cost of the TEG was determined on the basis of 3-year repayment period with regard to tariff for electric energy 0.2$US/kW-h.

Micro-CHP/TEG performance analysis

The task of the analysis is to define in the space of the basic technical and economic parameters of TEG such ratios thereof which assure the solution of the problem. For this purpose, we shall use a mathematical model given in [6]. Under conditions in hand, the decisive influence on the technical and economic features of TEG is exerted by thermal resistance ratios characterizing the process of heat transfer in the heating heat carrier – thermoelement – cooling heat carrier system. In the generalized form they are defined by the Biot criteria values on the cold (Bi_x) and hot (Bi_h) thermopile side

$$Bi = \frac{\alpha h}{\lambda}, \tag{1}$$

where $\alpha = \frac{1}{R_t}$ is the effective coefficient of heat exchange between the surface of junctions and heat carrier that takes into account all thermal resistances on the way of heat flux the sum of which comes to $R_t = \frac{1}{\alpha_0}$. Here, α_o is coefficient of heat exchange; h_i and λ_i is the thickness and thermal conductivity of each layer on the way of heat flux (connecting elements, heat spreader, thermopile package, solder layers, etc).

As long as $\sum_i = \frac{h_i}{\lambda_i}$ component is primarily defined by thermopile fabrication method, to independent parameters one should refer only thermoelement height h and coefficients of heat exchange on the cold α_x and hot side α_h. Let us consider in more detail the effect of these parameters and their related restrictions.

In [7], it was shown that for fixed heat exchange conditions (α_x=const; α_h=const) maximum power is realized under Bi =1, that is, there is a completely defined optimal thermoelement height h that assures maximum power. In this case, the available temperature difference $dt_o=[t_{ho} - t_{xo}]$ is equally divided between the useful drop ($dT=T_h - T_x$) and the loss in the drop ($dt=[(t_{ho} - T_h) + (T_x-t_{xo})]$) on thermal resistances R_t. The influence of thermoelement height on these parameters in dimensionless form is illustrated in Fig.3.

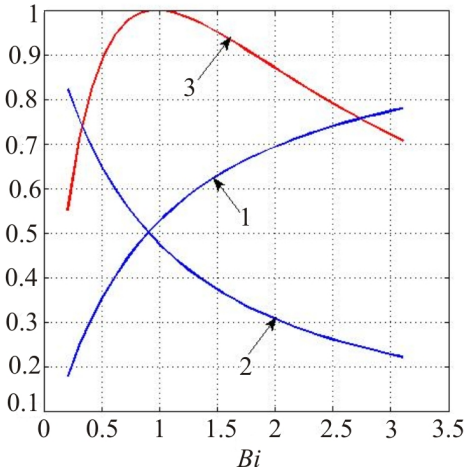

Fig.3. Dependences of the useful temperature drop (1), the loss in temperature drop (2) and thermoelement power (3) on the Biot criterion.

At the same time, the absolute power value is essentially dependent on heat exchange coefficient and monotonically increases with the latter (Fig.4).

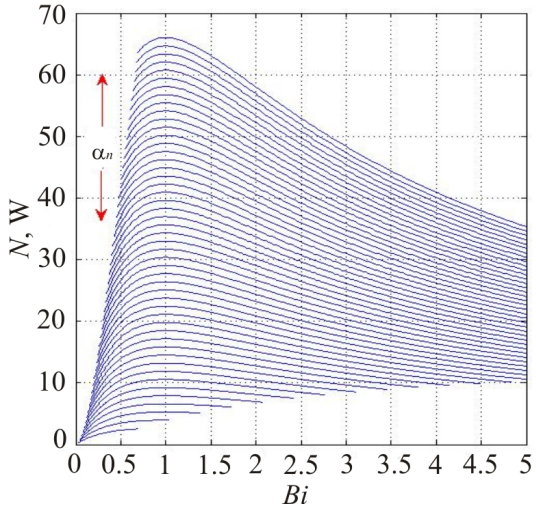

Fig.4. Dependence of thermoelectric module power on Bi for different combinations of thermoelement height h and heat exchange intensity α (arrows are used to denote the direction of parameter growth)

Thus, the optimal value of thermoelement height for known intensity of heat exchange is readily found from condition of Bi =1, Fig.5.

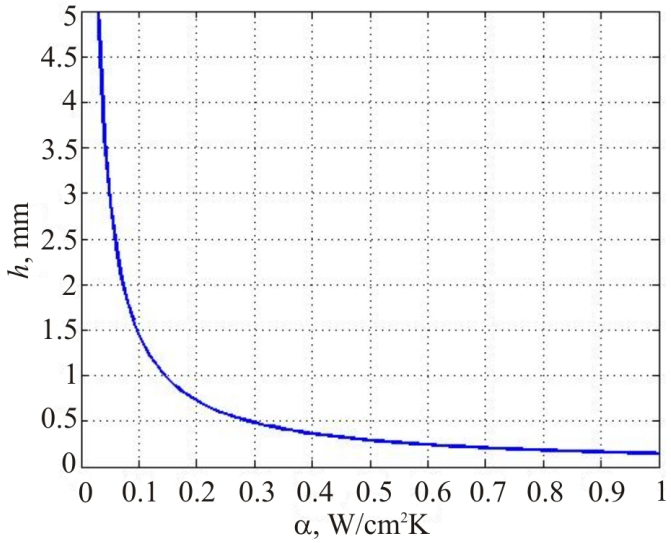

Fig. 5. Dependence of thermoelement optimal height h on the intensity of heat exchange α.

Dependences of power and efficiency of standard module 50×50 mm on the parameters under consideration are given in Fig.6 and Fig.7. Fig. 8 shows a counter plot visualizing the ratios between module power and efficiency that meet one of the main requirements of the problem – the efficiency > 6% (the respective ratio of h to α is marked by arrows).

For the most widespread technologies of thermoelectric module manufacturing the lower limit of thermoelement height can be assumed as h=0.5 mm. As it follows from Fig.8, for the effective use of thermoelements of such height it is necessary to assure condition $\alpha > 0.25$ (R_t=1/α <4). Taking into account that a typical value of heat exchange coefficient for conditions under consideration is $\alpha_o \approx 1$ W/cm^{2}K (that is, $R_{t\alpha} \approx 1$), one can formulate concrete requirements to quality of thermopile heat spreaders, namely their total thermal resistance must fit in the value of $\sum_i = \frac{h_i}{\lambda_i} < 3$.

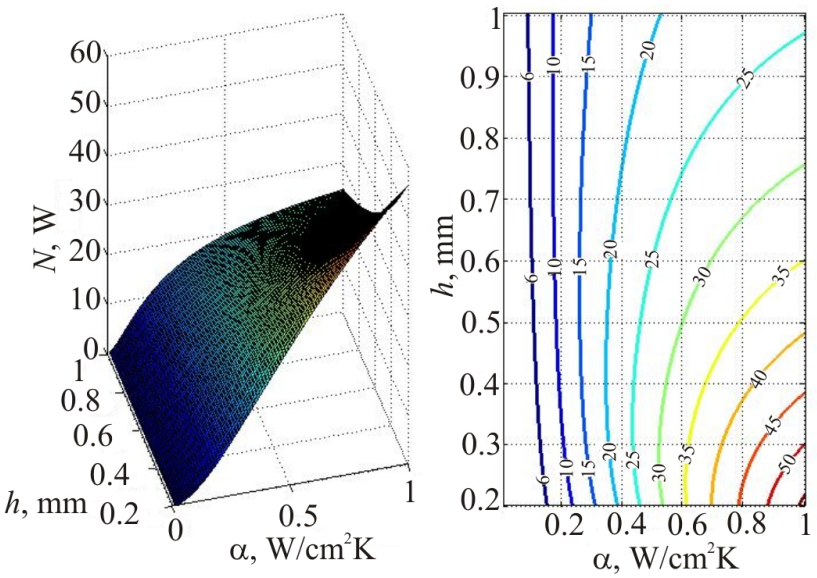

Fig.6. Dependence of TEG module power N on h and α.

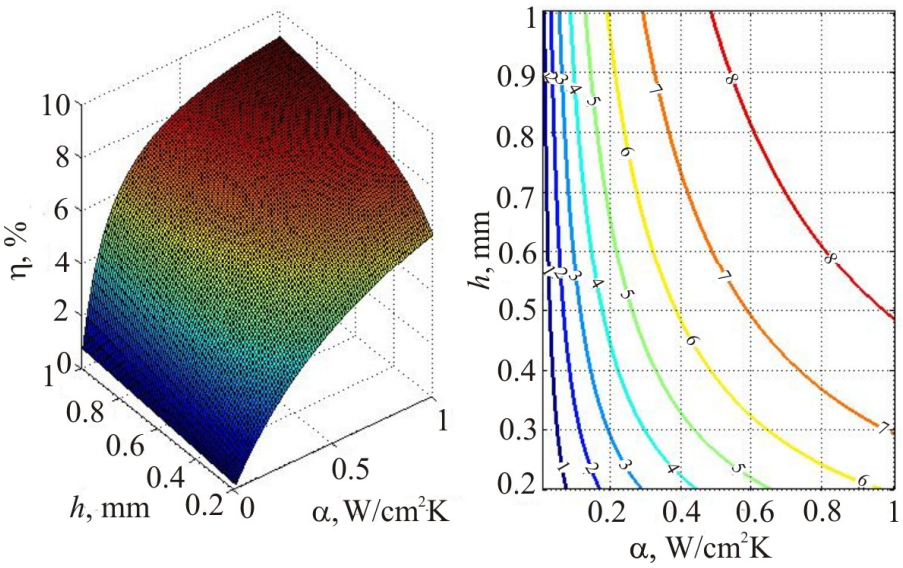

Fig.7. Dependence of TEG module efficiency on h and α.

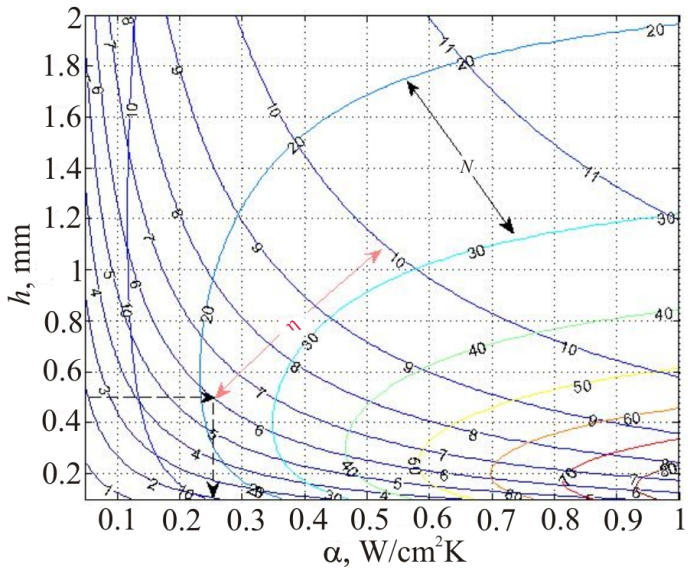

Fig. 8. An area of feasible solutions for TEG module in h, α space.

Based on these calculations, one can estimate the unit cost of CHP/TEG. For this purpose, the ratio for estimation of thermoelectric module unit cost has been used in the form:

$$\text{Price} = (k_1 g_m / k_2) / N_m, \$\text{US} / \text{W} \qquad (2)$$

where N_m – is module power, *W*;

g_m is mass of thermoelectric material in the module, *g*;

k_1= 0.4 is thermoelectric material cost, *$US/g;*

k_2=0.35 is the share of material cost in total module cost.

Coefficients k_1, k_2 have been found from the analysis of market value of thermoelectric modules. The results obtained are given in Fig. 9.

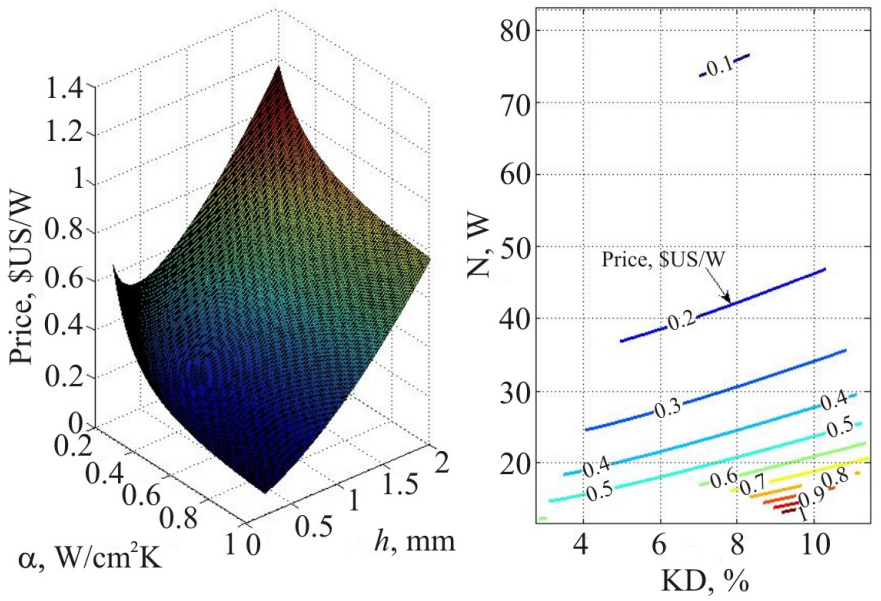

a) *b)*

Fig. 9. Unit cost of TEG module (\$US/W) in the area of feasible solutions.

From Fig.6*b* it follows that the real cost of TEG (0.3\$US/W) corresponds to power range of standard module 50×50×0.5 mm N_m =25...30 W and efficiency 6...8%. That is, the electric power of micro-CHP/TEG of given thermal power Q_o =16.9 kW can reach 1.3 kW with the total amount of thermoelectric modules about 50 pcs and their total cost about 400 \$US which meets completely the requirements of problem set (with account of additional expenses, as well as the cost of inverter and TEG design on the whole, the price of generating part of micro-CHP/TEG fits reliably in the sum of 1200\$US).

Conclusions

1. A scheme of micro-CHP/TEG based on gas boiler and heat exchange-type TEG has been considered.
2. It has been shown that the above scheme has quite acceptable technical and economic features that can assure its competitive ability in the market for micro-CHP.
3. The main requirements to TEG parameters assuring optimal technical and economic features of micro-CHP have been formulated.

Designations: h – thermoelement height, mm; T – thermoelement temperature; t – heat carrier temperature; T_p – characteristic temperature; λ – thermal conductivity coefficient, W/cm K; R_t – thermal resistance, cm²K/W; α – heat exchange coefficient, W/cm²K; $Bi = \frac{\alpha h}{\lambda}$ – Biot criterion.

Indices: h – hot; x – cold

References

1. http://world.honda.com/power/cogenerator/
2. http://viessmann.com.ua/sistemy-otoplenia-463/Kogeneracionnaia ustanovka VITOTWIN 300-W Mikro-KWK s dvigatelem Stirlinga.html

3. http://www.flowenergy.uk.com/meet-flow/
4. https://www.ofgem.gov.uk/environmental-programmes/feed-tariff-fit-scheme/tariff-tables
5. Yu.M.Lobunets, Thermoelectric Generator, Patent of Ukraine №8357 of 27.08.2013.
6. Yu.M.Lobunets, Performance Analysis of Heat-Exchange Type Thermoelectric Generator, J.Thermoelectricity 1. – P. 54 – 61 (2014).
7. Yu.M.Lobunets, Heat-Exchange Type TEG for Marine Propulsion Plants, J.Thermoelectricity **5**, 2014. – P. 29-36.

Submitted 10.03.2015

D.F. Worner

D.F. Worner

Jet Propulsion Laboratory, California
Institute of Technology,Oak Grove Drive,
Pasadena, 4800, CA, 91109, United States of America

ANOTHER UPDATE ON THE MULTI-MISSION RADIOISOTOPE THERMOELECTRIC GENERATOR POWERING THE CURIOSITY ROVER

The Multi-Mission Radioisotope Thermoelectric Generator (MMRTG) for the Mars Science Laboratory (MSL) mission was developed by the United States Department of Energy (DOE) for the National Aeronautics and Space Administration (NASA) and fueled on October 28, 2008 in preparation for a late 2009 launch. Once launched, the MSL spacecraft provided a hi-fidelity telemetry stream measuring the generator's electrical and thermal performance. These data were used to update predictive models and a new prediction of the performance of the MMRTG on the surface of Mars was run just before Entry, Descent, and Landing (EDL) at Mars. Once landed the MMRTG powering Curiosity was found to be working extremely well, providing power above predictions and operating within its flight allowable temperature limits. The generator was producing approximately 114 W at the beginning of the surface mission, a mission of nearly two Earth years or one Mars year. This paper will elaborate on the MMRTG's performance throughout the primary mission and the initial months of the first extended mission as well as discuss related events and phenomena that affected the MMRTG's performance.

Key words: radioisotope thermoelectric generator, power output, energy lifetime.

Introduction

The United States Department Of Energy (DOE) developed the Multi-Mission Radioisotope Thermoelectric Generator (MMRTG) for the National Aeronautics and Space Administration (NASA) [1], and the generator was conceived as a multi-mission power source supporting missions going to such diverse destinations in the Solar System as Europa, Titan, the Moon, and others. It is a highly reliable, long-lived, rugged radioisotope power system (RPS). The MMRTG can be landed on other bodies, works in either vacuum or atmospheres, provides quiet power, and can be flown on NASA's certified launch vehicles.

The Mars Science Laboratory (MSL) was chosen as the first mission to use the MMRTG. The generator is now at the base of Gale Crater on Mars powering and heating the Curiosity rover. See Fig. 1. for a depiction of the rover. The MMRTG provides power to charge the rover's batteries and when the scientists have selected experiments, the rover draws on the batteries to run science instruments, drive the vehicle, and do other activities that draw high current. Simultaneously, infrared heat from the MMRTG is captured by two heat exchangers surrounding the MMRTG. The heat is then circulated to the rover electronics box to keep the electronics well within their operating limits.

Key mission dates include landing: Aug. 6, 2012 [2]; first drive: Aug. 22, 2012 [3]; end of primary mission: June 24, 2014 [4].

A close-up view of the Multi-Mission Radioisotope Thermoelectric Generator can be seen in Fig. 2.

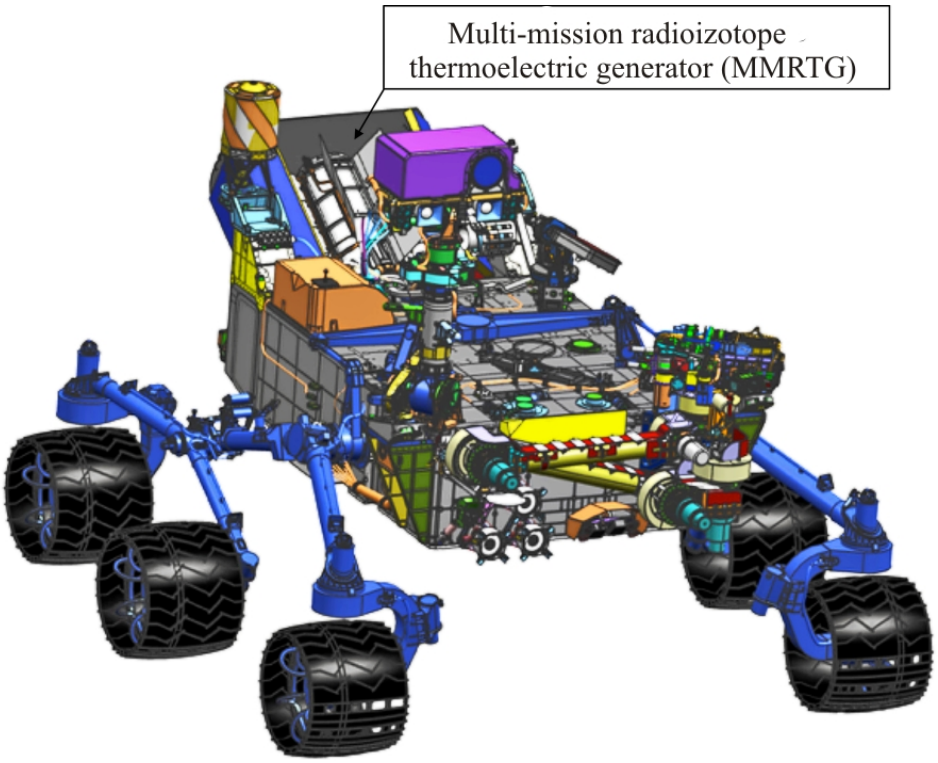

Fig. 1. Landed Rover Configuration. The Curiosity rover with MMRTG installed on the aft-end of the rover.

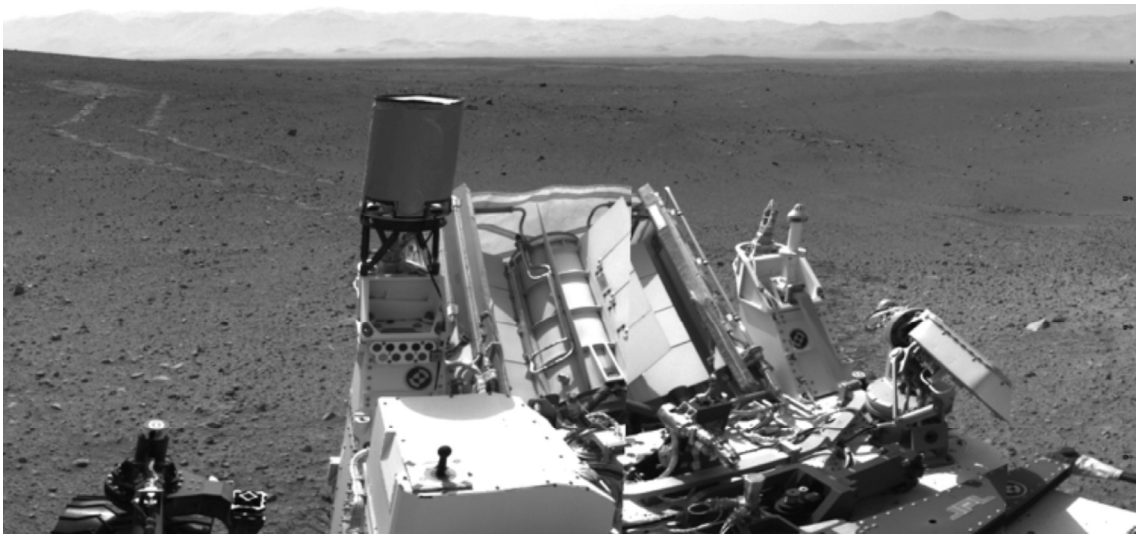

Fig. 2. MMRTG on Mars. This image was taken on sol 24.

This paper describes the MMRTG's performance and predictions of its performance from pre-launch through the start of the first extended mission along with discussion of several events and phenomena that affected its performance.

Pre-launch predictions

A set of power predictions using conservative assumptions for aging and degradation were prepared before launch, in June 2011, just months before launch. There were three predictions from three unique models that were plotted together, and uncertainty was assigned (see Fig. 3.) [5]. The MSL Project was briefed on those predictions, and the inherent uncertainties in the predictions. The MSL Project managers chose to re-plan the surface mission using the revised predictions plus uncertainty. The power predictions plus uncertainty meant the battery would be charged slightly more slowly; and hence, some science activities would take longer to achieve and some eliminated. The re-planned mission would still meet the NASA requirements.

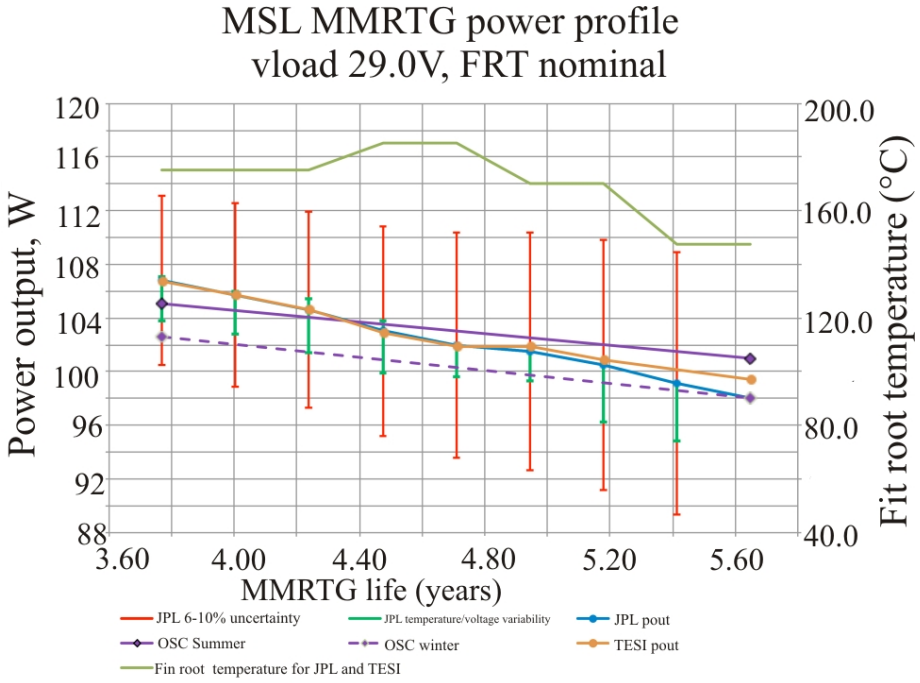

Fig. 3. Pre-Launch Power Predictions. MMRTG power prediction (power out, Pout) by the Jet Propulsion Laboratory (JPL) throughout the MSL surface mission including uncertainty, 6% at beginning of surface mission growing to 10% at end of mission. Orbital Sciences Corporation (OSC)/Analytix and Teledyne Energy Systems Inc. (TESI) data are also shown.

Landing

The temperature of the MMRTG rose rapidly from shortly before atmospheric entry until near landing as predicted. Venting the MMRTG cooling fluid caused this. The fluid was being circulated to the cruise stage where heat from the fluid was radiated over-board. To fly the entry vehicle in the Martian atmosphere, the cruise stage had to be jettisoned and the fluid vented to space. At approximately the same time as fluid venting, the segment of the power bus connecting the entry vehicle to the cruise stage was opened or dead-faced so that when the explosive bolt cutter severed the power bus wires, shorts would not affect the entry vehicle's performance. Fig. 4. depicts the primary sections of the Mars Science Laboratory spacecraft before atmospheric entry at Mars.

The power bus voltage dropped to ~31 V following power bus dead-facing [5]. This voltage change also shifted the MMRTG power operating curve to a new level, but downward power output trending remained at a steady rate except for a few minor transients. That is, the forced cooling of the

MMRTG had stopped, and it was still protected from direct interaction with the atmosphere inside the entry vehicle and so its fin root temperatures were rising rapidly.

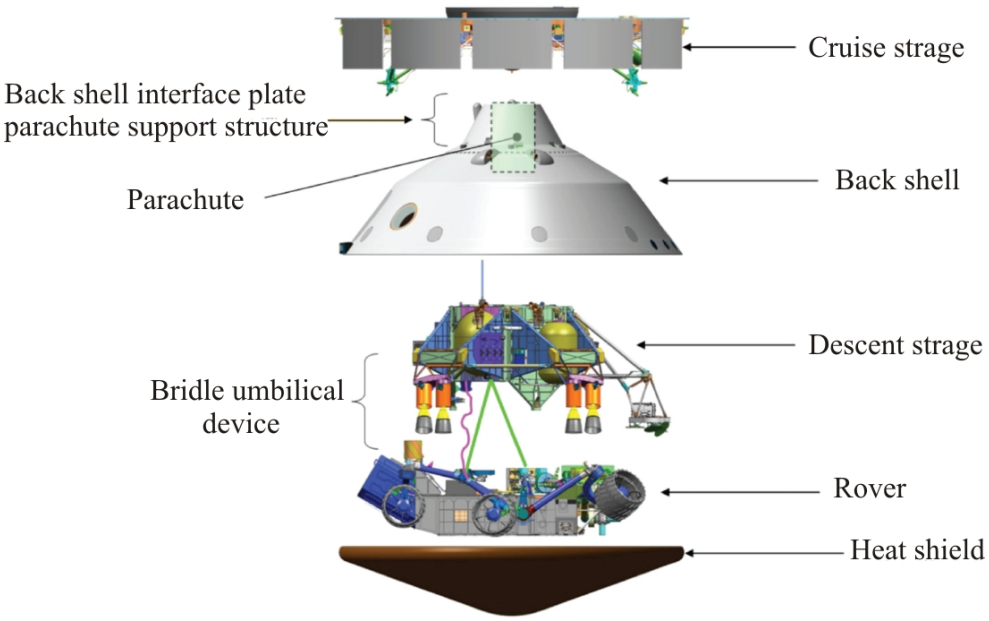

Fig. 4. Mars Science Laboratory Spacecraft. The Mars Science Laboratory spacecraft in an expanded view showing the how the key elements of the spacecraft are stacked together.

The rise in fin root temperature caused this collapse in the ΔT from the hot junction to the cold junction led to a power drop from the MMRTG. Power output declined until heat shield separation (HSS), and then the breeze of the atmosphere had an effect. At heat shield separation, the MMRTG power output started to recover. The rate of increase in MMRTG temperatures was observed to slow down. The power output completed a slow recovery until it reached a new steady state at roughly 114 W about 5 hours after the cooling fluid was vented. This actual, steady state value of 114 W compares to a predicted 106.3 W.

Primary mission power output

The monthly, average power output and the monthly temperatures are plotted in Fig. 5. The monthly average power output has steadily declined reflecting an average degradation rate of ~4.8% per year since landing. That includes fuel decay and reduced Carnot efficiency. The figure also shows that average temperatures have stayed within a 7°C band showing the generator temperature is falling with time, another indication of the fuel decaying with time. Fig.6. plots average monthly power output measurements between maximum and minimum power average curves. Power varies between minimum and maximum on a daily and monthly basis for several reasons. The causes of the greatest changes in power output on a daily basis are rover power bus-load voltage changes, temperature swings in the atmosphere, and the daily rising and setting of the Sun heating the MMRTG.

However, Fig. 5. suggests average temperatures are not moving sufficiently to be the dominant cause of change in power output. Power bus voltage changes are a dominant source of change in power output; these load changes occur daily as the rover wakes in the morning and draws on the battery throughout the day and is then put into sleep mode where the MMRTG recharges the battery for the next day's operations.

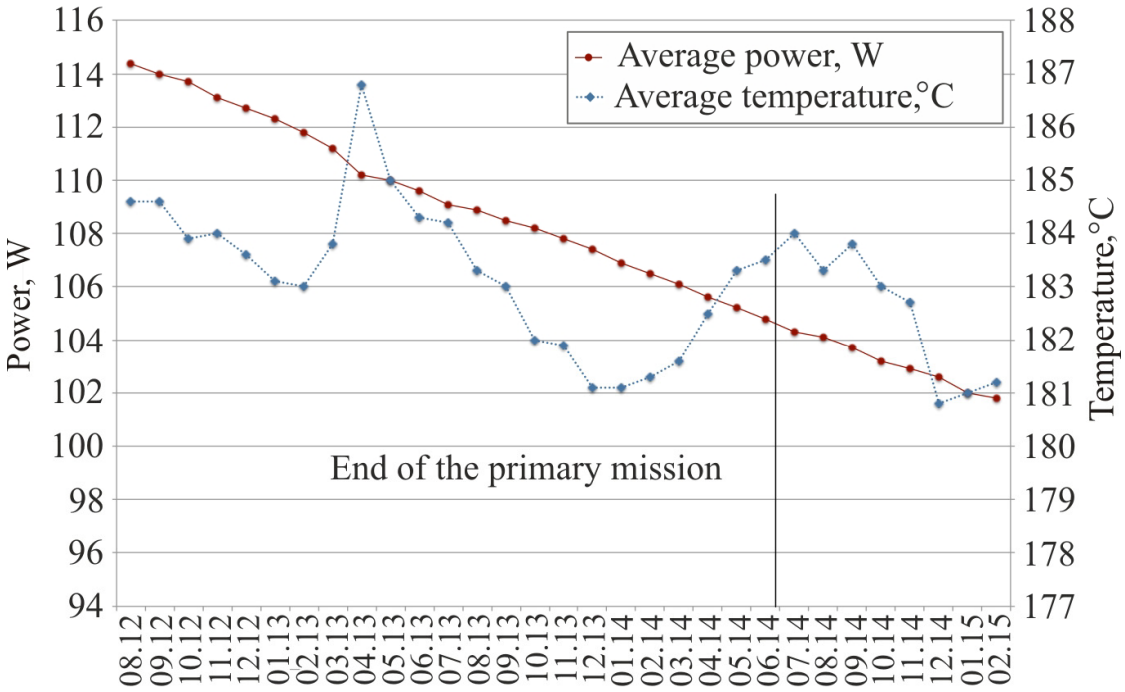

Fig. 5. MMRTG power and temperature. Monthly average power output (left axis) and monthly average temperatures (right axis) for a temperature sensor that is used in estimating the fin root temperature of the MMRTG on the Curiosity rover are plotted. Dates are read as Month-20xx.

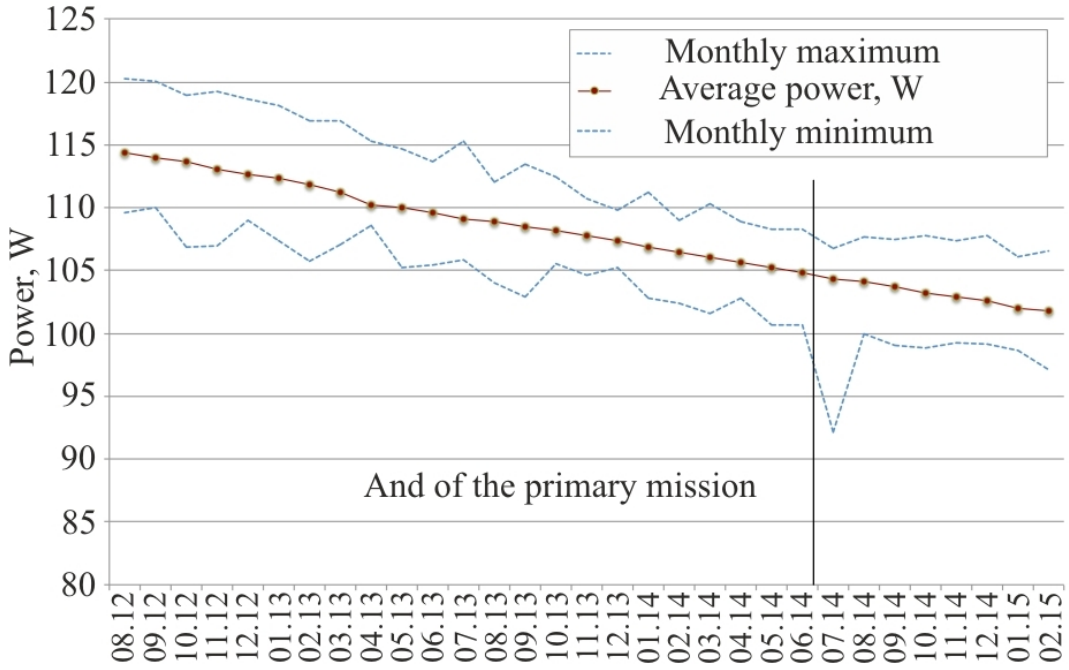

Fig. 6. MMRTG power output. Monthly averages for minimum, maximum, and average power output from the MMRTG powering the Curiosity rover. Dates are read as Month-20xx.

Winds on mars and their effects on multi-mission radioisotope thermoelectric generator temperatures

Atmospheric temperature changes are not the dominant cause of power output changes in the MMRTG on the Curiosity rover, but they can be significant. Atmospheric temperatures can drive power output to be especially volatile when daily cooling near sunset is followed by visiting "dustless" dust devils as on sol 37 [6, 7] or katabatic winds [8, 9]. In addition, thermal tides are planetary-scale gravity waves with periods that are harmonics of the solar day and are caused by the interaction of the atmosphere on the illuminated side of the planet with the solar radiation [9] and amplified by the Gale Crater topography [7].

The Rover Environmental Monitoring Station (REMS) on the MSL mission has sensors recording air and ground temperature, local atmospheric pressure, relative humidity, wind speed, as well as ultraviolet radiation in different bands (between 280 and 400 nm). Since sol 9, after landing, the REMS has collected data from all sensors simultaneously on an almost daily basis [9]. Fig. 7. is a plot of data from one of the MMRTG's temperature sensors that closely follows the effects of the typical effect of katabatic winds seen by the REMS instrument shortly after sunset.

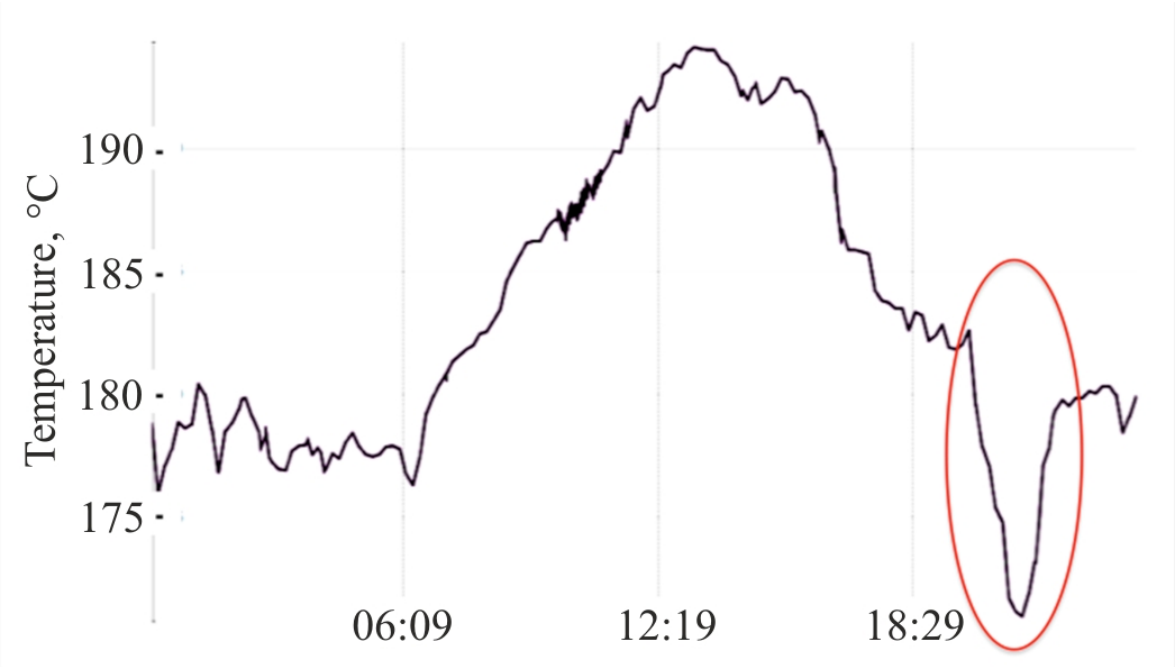

Fig. 7. Diurnal temperature swings. MMRTG fin root temperatures throughout a single sol, sol 87, are plotted; the hottest part of the sol is near noon. The circled segment of curve marks when katabatic winds blow over the MMRTG and rapidly lower the average fin root temperature. The winds then subside, and the fin root temperature rises quickly back to a nominal value. Times on the x-axis are Mars Local Times.

Heat plume over multi-mission radioisotope thermoelectric generator

The MMRTG is mounted between two nearly vertical heat exchangers, see Fig. 1., and those act as mounting points for a windscreen.

The opposite end of the MMRTG is on the rover-mounting interface. The sides of the MMRTG facing the sky and the ground are not enclosed.

The MMRTG rejects approximately 1900 W of heat continuously. Some of that heat is picked up by the rover to keep the electronics within their allowable flight temperatures. The remainder ends up in the Martian atmosphere or surface in one way or another. Before launch a thermal geyser or plume was postulated [10], the Martian atmosphere would be heated by the MMRTG's waste heat and rise over the rover, creating a buoyant plume. Fig. 7. indicates that for much of sol 87 there was little to no breeze; this pattern has been seen on most sols.

The plume may be acting as a "dust shield" for the MMRTG and aft portions of the rover by preventing dust borne by the Martian atmosphere from falling or drifting down onto the MMRTG. A series of "selfies" taken by the rover's arm-mounted camera show how soil and dust have accumulated as a function of time on the forward end of the rover. Some of that material was deposited on the rover as a result of performing sample handling, which increased after the first year on Mars; sample handling takes place on the forward end of the rover using the arm mounted there, and inevitably some material from multiple samples has been spilled onto the rover while trying to drop samples into small ports that lead to some of the instruments. However, that does not account for all of the material as some is clearly falling from the atmosphere. Fig. 8. shows accumulated dust as a function of time on the aft end of the rover well away from the sample handling equipment. In addition, the MMRTG appears to be nearly completely free of dust after approximately 2.5 years of operations on Mars. Something is shielding the MMRTG and nearby equipment from dust, likely the plume of waste heat from the generator.

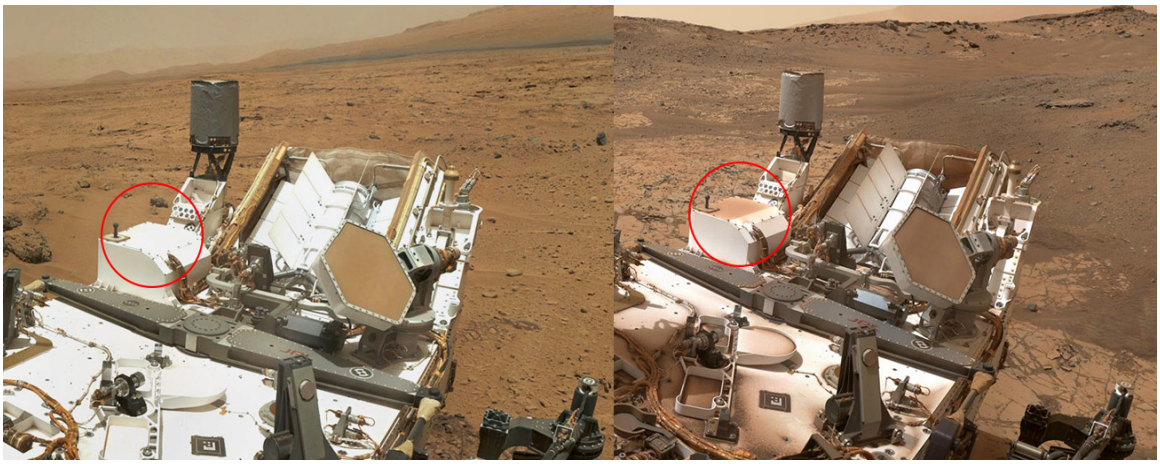

Fig. 8. Comparison of accumulated dust. Dust accumulated on the aft-end of the rover that was not deposited by the sample handling equipment. The image on the left is from October 2012, and the image on the right is from February 2015. The circled horizontal area on the right clearly shows dust accumulation over the previous years in comparison with the circled area on the left.

Extended mission (EM1 overview)

The MSL Project began planning for an extended mission in 2013 anticipating that if the rover was healthy in late 2014, NASA would likely fund an extended mission. Part of the planning included modeling available energy for science. Fig. 9. plots the estimate used for planning purposes.

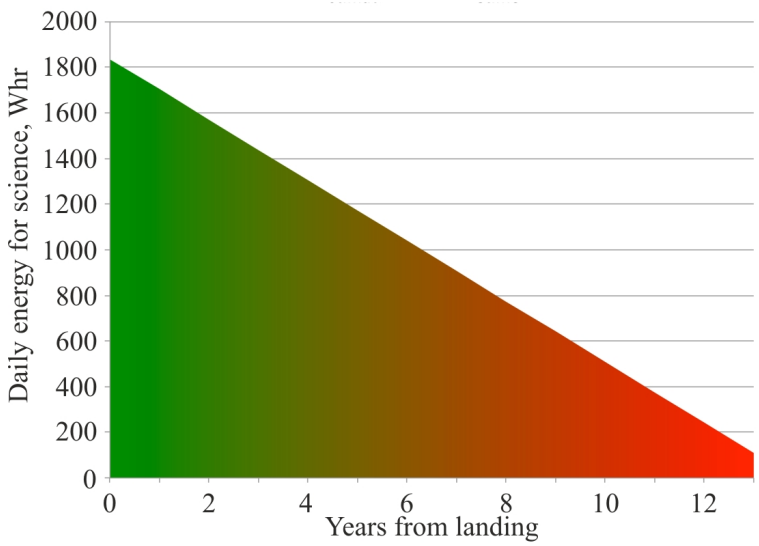

Fig. 9. Long-range energy estimate. The MSL mission uses the MMRTG to charge batteries and then draws on the batteries to conduct operations that consume high current. This plot shows how much energy should be available from the batteries as a function of time for science after accounting for the minimum energy needs of the engineering subsystems of the rover. The green section of the plot indicates there should be adequate energy to conduct all envisioned science experiments. The transition to red indicates the science experiments will likely be more limited in that timeframe.

Bumps along the way: loss of multi-mission radioisotope thermoelectric generator power circuit isolation

The Curiosity rover uses a "floated" power bus. That is, the power bus is isolated from the rover chassis by two 5 kΩ resistors. Fig. 10. is a cartoon depicting the arrangement. The MMRTG power leads are connected to two secondary batteries and separated from the rover chassis by two 5 kΩ resistors. The output from the MMRTG and batteries is used to power rover loads or is shunted to resistors. In the lower right hand corner of Fig. 10. is a depiction of known shorts in the pyrotechnic system that have tied the rover power bus return to the rover chassis; the number of shorts is unknown, but their total resistance is estimated as 6 kΩ; these shorts developed before touchdown on Mars.

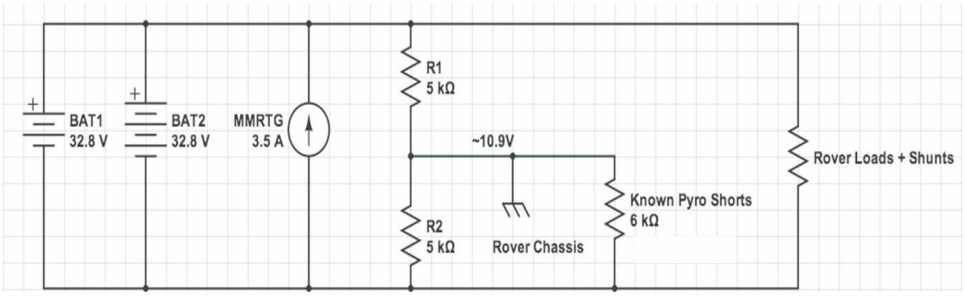

Fig. 10. Curiosity Power Bus. The diagram depicts the floating power bus used on the Curiosity rover. (Abbreviations used in the diagram are battery 1 (BAT1), battery 2 (BAT2), Multi-Mission Radioisotope Thermoelectric Generator (MMRTG), resistance 1 (R1), and resistance 2 (R2).)

By floating the rover power bus, the spacecraft gains a single-level of fault tolerance for the power bus. If a rover load has a short in its power supply and that short connects the power bus to the

chassis, rover operations would not be affected in the long run; science operations might stop temporarily as the engineers review the rover telemetry, but the hardware would continue to function normally in the presence of such a short.

On November 17, 2013, the rover's fault protection halted science operations [11] and sent an alert to the operations team in Pasadena, California. The alert came with telemetry that indicated what triggered the fault protection response to halt science operations. The power bus isolation from the chassis had changed in a significant manner; it had intermittently come and gone over several sols. NASA issued a press release on November 20, 2013 describing the situation [11]. In addition, a tiger team reviewed all of the spacecraft data and developed a fault tree. The tiger team meticulously evaluated each fault in the tree until the most likely fault was identified. The most likely fault was that the MMRTG had an internal short between its power circuit and the MMRTG housing. This behavior was seen during ground test of the engineering unit (EU) MMRTG. In addition, this behavior has been seen in other RTGs including the RTGs powering the Cassini spacecraft and Voyager spacecraft.

No adverse effect was identified as resulting from these shorts except to note that if they were to become permanent, they might degrade or eliminate the single-fault tolerance designed into the spacecraft as noted earlier. In earlier engineering unit tests and in-flight events on other missions, the shorts proved to be minor nuisances and temporary. Indeed, within a week of having detected the fault on the Curiosity rover, the fault cleared and the power bus isolation returned to its nominal value. A similar short did not return until approximately a year later.

This time, science operations were not halted. The data were reviewed and a plan put in place to attempt to clear the fault deliberately if the need arose. This time the fault did not clear in a short period, and the rover team was set to drill a nearby rock. The drill power circuit was designed to include a "battle short," a short that could be switched on and off by ground command and that shorted the power bus return to the rover chassis, thereby bypassing the isolation resistors. The battle short was built into the rover to counteract a specific power fault in the drill, but now, with the Multi-Mission Radioisotope Thermoelectric Generator suffering isolation faults, mission planners decided that activating the battle short while the MMRTG had an isolation short might send enough current through the isolation short to melt it or clear it.

Fault diagnoses during ground test of the MMRTG isolation losses and review of the isolation losses on other deep space missions indicated that the shorts were quite small dimensionally and/or were likely composed of non-metallic materials that would melt away under sufficient current. When this second MMRTG fault persisted, the rover operations team chose to attempt to "blow" the short. They activated the battle short, and within 1.5 seconds the MMRTG isolation short had cleared.

Rover drilling operations resumed almost immediately, and the short has not returned since. Similar circuits are now being designed into ground support equipment used to operate MMRTGs under life test so more detailed information can be gleaned about their shorts if they arise [12].

Conclusion

The MMRTG on the Curiosity rover continues to perform well and exceed predictions for both power and heat output. The internal shorts it infrequently experiences appear to be nuisances rather than high-risk events. The extended mission for the Curiosity rover was approved in September 2014, and the rover is now several months into that extended mission.

Acknowledgments The research described in this publication was carried out at the Jet Propulsion Laboratory, California Institute of Technology, under a contract with the National Aeronautics and Space Administration.

Reference herein to any specific commercial product, process, or service by trade name, trademark, manufacturer, or otherwise does not constitute or imply its endorsement by the United States Government or the Jet Propulsion Laboratory, California Institute of Technology.

References

1. D.Woerner, Use of an MMRTG for the 2009 Mars Science Laboratory Mission, *American Geophysical Union, Fall Meeting 2005*, abstract #P54A-02.
2. M.Wall, Touchdown! Huge NASA Rover Lands on Mars, *Space.com*, August 6, 2012. http://www.space.com/16932-mars-rover-curiosity-landing-success.html (accessed April 13, 2015)
3. *Mars Science Laboratory Curiosity Rover*, web page, Jet Propulsion Laboratory, California Institute of Technology, Pasadena, California, periodic updates. http://mars.jpl.nasa.gov/msl/mission /timeline/firstdrive/ (accessed April 13, 2015)
4. *Mars Science Laboratory Curiosity Rover*, web page, "NASA's Mars Curiosity Rover Marks First Martian Year with Mission Successes," Jet propulsion Laboratory, California Institute of Technology, Pasadena, CA, June 23, 2014 http://mars.nasa.gov/msl/news/whatsnew/index.cfm?Fuse Action=ShowNews&NewsID=1653 (accessed April 20, 2015)
5. D.Woerner, V.Moreno, L. Jones, R. Zimmerman, and E.Wood, "The Mars Science Laboratory (MSL) MMRTG *In*-Flight: A Power Update, *Nuclear and Emerging Technologies for Space* (*NETS 2013*), *American Nuclear Society,* 2013.
6. H.Kahanpää, M. de la Torre Juarez, J.Moores, N.Rennó, S.Navarro, R.Haberle, M-P.Zorzano, J.Martín Torres, J.Verdasca., A.Lepinette, J.A.Rodríguez-Manfredi, and J.Gomez-Elvira, The REMS Team and the MSL Science Team, Convective Vortices at the MSL Landing Site, *Fifth International Workshop on the Mars Atmosphere: Modeling and Observations*, Oxford, United Kingdom, January 13–16, 2014.
7. M.A.Mischna, J.Gómez-Elvira, C.Armiens, I.Carrasco, M. Genzer, F.Gómez, R. Haberle, V.E.Hamilton, A.-M. Harri, H.Kahanpää, O.Kemppinen, A. Lepinette, J.Martín Soler, J. Martín-Torres, J.Martínez-Frías, L.Mora, S.Navarro, C.Newman, M.A.de Pablo, V.Peinado, J.Polkko, S.C.R. Rafkin, M. Ramos, N.O. Rennó, M.Richardson, J.A. Rodríguez-Manfredi, J.J.Romeral Planelló, E. Sebastián, M.de la Torre Juárez, J.Torres, R.Urquí1, A.R.Vasavada, J.Verdasca, M-P.Zorzano, and the MSL Science Team, Results from the Rover Environmental Monitoring Station (REMS) on Board the Mars Science Laboratory, *Fifth International Workshop on the Mars Atmosphere: Modeling and Observations*, Oxford, United Kingdom, January 13–16, 2014. http://www-mars.lmd.jussieu.fr/oxford2014/abstracts/mischna rems oxford2014.pdf (accessed April 14, 2015)
8. F.J.Martín-Torres, M.-P. Zorzano, C.Armiens, I.Carrasco, A. Delgado-Bonal, M.Genzer, F.Gómez, J.Gómez-Elvira, R.Haberle, V.E.Hamilton, A.-M. Harri, H.Kahanpää, O.Kemppinen, M.T.Lemmon, A. Lepinette, J.Martín Soler, J.Martínez-Frías, M.Mischna, L.Mora, S.Navarro, C. Newman, M.A.de Pablo, J.Pla-García, V.Peinado, J.Polkko, S.C.R. Rafkin, M.Ramos, N.O.Rennó, M.Richardson, J.A.Rodríguez-Manfredi, J.J.Romeral Planelló, E.Sebastián, M. de la Torre Juárez, J.Torres, A.Ullán, R.Urquí1, P.Valentín-Serrano, A.R.Vasavada, and the MSL Science Team, Highlights from the Rover Environmental Monitoring Station (REMS) on Board the Mars Science Laboratory: New Windows for Atmospheric Research on Mars, *Fifth International Workshop on the Mars Atmosphere: Modeling and Observations*, Oxford, United Kingdom, January 13–16, 2014.
9. J.Gómez-Elvira, C.Armiens, L.Castañer, M.Domínguez, M.Genzer, F.Gómez , R.Haberle, A.-

M.Harri, V.Jiménez, H.Kahanpää, L.Kowalski, A.Lepinette, J.Martín,, J.Martínez-Frías, I.McEwan, L. Mora, J.Moreno, S.Navarro, M.A.de Pablo, V.Peinado, A.Peña, J. Polkko, M.Ramos, N.O.Renno, J.Ricart, M.Richardson, J.Rodríguez-Manfredi, J. Romeral, E. Sebastián, J.Serrano, M. de la Torre Juárez, J.Torres, F. Torrero, R.Urquí, L.Vázquez, T. Velasco, J.Verdasca, M.-P.Zorzano, and J.Martín-Torres, REMS: The Environmental Sensor Suite for the Mars Science Laboratory Rover, *Space Science Reviews*, volume 170, Issue 1-4, pages 583–640, September 2012. http://link.springer.com/journal/11214 (accessed April 13, 2015)

10. P.Bhandari and K.Anderson, CFD Analysis for Assessing The Effect Of Wind on the Thermal Control of the Mars Science Laboratory Curiosity Rover, *43rd International Conference on Environmental Systems*, The American Institute of Aeronautics and Astronautics, 2013. http://arc.aiaa.org/doi/abs/10.2514/6.2013-3325 (accessed April 13, 2015)
11. "Curiosity's Recent Bad Month on Mars – Science Operations Halted Again by Electrical Issue," *Spaceflight Insider*, November 23, 2013. http://www.spaceflightinsider.com/missions/curiositys-recent-bad-month-on-mars-science-operations-halted-again-by-electrical-issue/ (accessed April 13, 2015)
12. G.Bolotin and N.Keyawa, Active Short Circuit - Chassis Short Characterization and Potential Mitigation Technique for the MMRTG, *Proceedings of the 2015 Nuclear and Emerging Technologies for Space Conference*, February 23–26, 2015, Albuquerque, New Mexico, United States of America.

Submitted 05.03.2015

NEWS
OF INTERNATIONAL THERMOELECTRIC ACADEMY

XVI INTERNATIONAL FORUM ON THERMOELECTRIVITY

The Forum took place from May 19 to 22, 2015 in Paris in the conference hall “Forum de Grenelle”, in the immediate vicinity of the Eiffel Tower and other attractions of Paris.

The Forum was dedicated to Jean-Charles Peltier, a French researcher and pioneer in thermoelectric cooling.

The International Thermoelectric Academy (ITA), a French Company Marvel Thermoelectrics, the Institute of Thermoelectricity of NAS and MOS of Ukraine and the Ham Town Council acted as organizers of the Forum.

The following persons formed the International Organizing Committee: L.Anatychuk (Ukraine), Chair, A.Casian (Moldova), H.J. Goldsmid (Australia), J. Sharp (USA), J. Snyder (USA), J. Stockholm (France), L. Chen (China), M.Fedorov (Russia), R. Funahashi (Japan), S. Asmontas (Lithuania), T. Kajikawa (Japan), Y. Grin (Germany) – members. The Local Organizing Committee was headed by J. Stockholm (France).

The objective of the Forum was the analysis of the state-of-art in thermoelectricity based on the information of the achievements in the field within the last two years, broad debate on identification of the most prospective trends in thermoelectricity, formulation of recommendations aimed at acceleration of progress in thermoelectricity

17 thermoelectric organizations and companies acted as sponsors of the Forum, namely: ALTEC-M (Ukraine), Crystal TE (Russia), FerroTec (Japan), Genterm (USA), ISP NASU (Ukraine), KELC (Japan), Marlow Industries (USA), Modul (Ukraine), RIF Corporation (Russia), RMT Ltd (Russia), SELEN (Azerbaijan), Smart Thermoelectrics (Russia), SODERN (France), Thermion Company (Ukraine), Thermoprylad (Ukraine), Z-Max (Japan).

Leading specialists from 25 countries took part in the work of the Forum.

124 presentations were made at the Forum, 12 of which were invited, made by world leading scientists on the achievements in thermoelectricity, 42 oral presentations and 70 poster sessions.

President of the ITA, Dr. L.Anatychuk (Ukraine)

President of the International Thermoelectric Academy, academician of the National Academy of Sciences of Ukraine, L.Anatychuk opened the Forum.

The participants of the Forum observed a minute of silence to honour the memory of the ITA members K.I. Uemura, R. Buist, V.Mykhailovsky and V.Schennikov who passed away in 2013-2015 .

President of the ITA, Dr. L.Anatychuk (Ukraine) presented a film "On life and scientific activity of Jean-Charles Peltier".

The invited paper on recent activity on thermoelectric power generation technology in Japan was presented by an ITA academician, Dr.T. Kajikawa (Shonan Institute of Technology, Japan) and Dr. R. Funahashi (National Institute of Advanced Industrial Science and Technology Ikeda, Osaka, Japan).

L. Chen (China)

An ITA academician Dr. L. Chen (Shanghai Institute of Ceramics, China) reported on recent progresses on thermoelectric materials and applications in China within the last two years.

Y. Shinohara (Japan)

An ITA associate, Dr.Y. Shinohara (National Institute for Materials Science, Japan) presented a report on the present situation of thermo-module development in Japan.

Dr. L. Bulat, an ITA academician (ITMO University, Russia), Dr. M. Fedorov, an ITA academician and Dr. Burkov (Ioffe Physical-Technical Institute of the Russian Academy of Sciences, Russia) made a presentation on the development of thermoelectricity in Russia in 2013-2014. In this presentation the results of basic and applied researches carried out in the universities, institutes and at enterprises of the Russian Federation were considered.

The survey on the main achievements in thermoelectricity in Western Europe in 2013 – 2014 was introduced by an ITA academician, Dr. J. Stockholm (Marvel Thermoelectrics, France).

R. Funahashi (Japan)

L.Bulat (Russia)

J. Stockholm (France)

An ITA academician, Dr. J. Snyder (California Institute of Technology, Pasadena, California, USA) reported on the activity in the sphere of thermoelectricity in the USA.

J. Snyder (USA)

The work of the Forum was accompanied by interesting discussion which lasted even during the participants' informal communication.

Scientific reports on the physics of thermoelectricity were made by: Dr.S. Ašmontas, an ITA academician (Lithuania) "Peltier effect of hot carriers"; Dr.L.Vykhor, an ITA associate (Ukraine) "Bulk Peltier effect: history, theory and practical applications"; Dr. C. Goupil (France) "Feynman ratchets and thermoelectric systems: harmonic response and feedback".

In thermoelectric material science the reports were made by: Dr. A.Casian, an ITA academician (Moldova) "Prospects of low dimensional organic materials for thermoelectric applications"; Dr. P. Jund (France) "Design of thermoelectric materials via first principles calculations"; Dr.J. Grin, an ITA associate (Germany) "Chemical bonding and thermoelectric ability of materials"; Dr. V. Khovaylo (Russia) "Preparation and power factor of polyacrylonitrile-based nanocomposites"; Dr. A. Kao (Great Britain) "Thermoelectric magnetohydrodynamics in the solidification of alloys"; Dr. Q. Yao (China) "Highly regular and orderly P3HT film with enhanced thermoelectric perfomance"; Dr. J. de Boor (Germany) "Lightweight $Mg_2Si_{0.8}Sn_{0.2}$ for thermoelectric energy conversion";

S. Ašmontas (Lithuania)

C. Goupil (France)

A.Casian (Moldova)

Y. Grin (Germany)

L.Vykhor (Ukraine)

P. Jund (France)

V. Khovaylo (Russia)

A. Kao (Great Britain)

J. de Boor (Germany)

О.Н. Урюпин (Russia)

А. Воронин (Russia)

X. Zianni (Greece)

Dr. O.Uryupin, an ITA associate (Russia) "Thermoelectric properties of carbon nanotubes/ polyvinylidene fluoride composite"; Dr. J.-C. Tédenac, an ITA associate (France) "High manganese silicides for thermoelcrics.Thermodynamic database for manganese silicides"; Dr. A.Voronin (Rusia) "Features of sintering process of *Ni*(*M*)*Sn* (*M* = *M* = *Ti*, *Zr*, *Hf*) half-Heusler alloys"; Dr. A. Maignan (France) "Ceramics of thermoelectric oxides and sulfides: recent results from CRISMAT (crystallography and material science labortory)"; Dr. H. Funashima (Japan) "Theoretical study of chalcopyrite and derived compounds as thermoelectric materials"; Dr. X. Zianni (Greece) "Modeling the thermoelectric properties of modulated nanocomposites"; Dr. M. Ohtaki (Japan) "Enhanced phonon scattering in nanostructured oxide materials"; Dr. O.I. Lebedev (France) "Evidences and impact of advanced transmission electron microscopy for thermoelectric materials".

The thermoelectric applications were reported on by: Dr. D. Woerner (USA) "Another update on the multimission radioisotope thermoelectric generator powering the Curiosity rover"; Dr. T. Caillat, an ITA academician (USA) "Advanced thermoelectric technology for space power generation";

Q. Yao (China)

J.C. Tedenac (France)

A. Maignan (France)

H. Funashima (Japan)

O.I. Lebedev (France)

T. Caillat (USA)

G.Gromov (Russia)

K.T.Wojciechowski (Poland)

Dr. L.Vykhor, an ITA associate (Ukraine) "Devices with thermoelectric pumps for supply of astronauts with drinking water during long-term flights"; Dr. G.Gromov, an ITA associate (Russia) "Applications of thermoelectric micromodules: coolers, generators, sensors"; Dr. C.A. Gould (Great Britain) "The modelling and simulation of Bi_2Te_3 thermoelectric generators in synopsys TCAD"; Dr. R. Dekhtyaruk (Russia) "Thermoelectrically cooled high power LED for automotive indutry"; Dr. K.T. Wojciechowski, an ITA associate (Poland) "Analysis of possibilities of adapting thermoelectric technologies for improvement of energy efficiency of chosen devices in a combined heat and power plant".

In his presentation Dr. L.Anatychuk, President of the ITA (Ukraine) provided the results of the comparative analysis of a thermoelectric converter of energy into electricity and other types of converters. The rational areas of electric power, cooling capacity and informativeness parameters were determined which enable the absolute advantages of thermoelectric energy conversion. The requirements to materials were described where the economic expedience of thermoelectricity application is considered; as well as examples of thermoelectric energy converters mass applications with the account of the above approaches.

M. Ohtaki (Japan)

D. Woerner (USA)

C.A. Gould (Great Britain)

R. Dekhtyaruk (Russia)

Dr. L.Anatychuk, an ITA academician, gives a presentation " On the promising global applications of thermoelectricity, the related technologies and materials"

The reports on the scientific activity of the candidates nominated for election as the ITA academicians or associates as well as those from scientists and representatives of the organizations, participating in the contest for the International Thermoelectric Academy Honorary Golden Prize. For election academicians of the International Thermoelectric Academy the reports of the following candidates were made: Dr. R. Funahashi (Japan) "Development of thermoelectric waste heat recovery at medium and high temperature"; Dr. A. Maignan (France) "From solid state chemistry to thermoelectric materials"; Dr. A. Terekov (Russia), an ITA associate "NPO "Kvant" achievements in the field of thermoelectricity"; Dr. E.I. Rogacheva, an ITA associate (Ukraine) "Size effects in thin-film structures and composites based on the perspective thermoelectric materials"; Dr. A. Burkov (Russia) "State-of-the-art thermoelectric metrology and materials"; Dr. X. Shi (China) "From caged thermoelectric skutterudites to the discovery of abnormal transports in Cu-based materials"; Dr. H. Böttner (Germany) "Thin layers leading to thick changes". The candidates for the ITA associates presented the following reports: Dr. T. Fröhlich (Germany) "Challenges in measuring the temperature of exhaust gas of combustion engines"; Dr. E. Velmre (Estonia) "Unknown pages in life and scientific activity of Thomas Johann Seebeck"; Dr. R.Kuz (Ukraine) "On computer simulation in thermoelectricity";

A. Terekov (Russia)

E. Rogacheva (Ukraine)

A. Burkov (Russia)

T. Fröhlich (Germany)

R.Kuz (Ukraine)

V. Lysko (Ukraine)

R. Kobylianskyi (Ukraine)

Dr. A. Prybyla (Ukraine) "Thermoelements using thermoEMF anisotropy"; Dr. R. Kobylianskyi (Ukraine) "Short-circuited thermoelements and their applications" For being awarded the International Thermoelectric Academy Honorary Golden Prize such reports were made: Dr.S. Ašmontas, an ITA academician (Lithuania) "Thermoelectricity of hot current carriers"; Mrs. R. Gruneisen from SODERN Company (France) "Thermoelectric applications in SODERN company products".

A general International Thermoelectric Academy meeting took place on May 21, 2015 during the work of the Forum where on the contest grounds and by means of secret vote new academicians were elected, namely: Dr. R. Funahashi, Japan; Dr. A. Maignan, France; Dr. A.Terekov, Russia; Dr. E.Rogachova, Ukraine, Dr. A. Burkov, Russia; Dr. X. Shi, China; Dr. L.Vykhor, Ukraine; Dr. H. Böttner, Germany. The following scientists were elected the ITA asscates: Dr. T. Fröhlich, Germany; Dr. E. Velmre, Estonia; Dr. R.Kuz, Ukraine; Dr. V.Lysko, Ukraine; Dr. A.Prbyla, Ukraine; Dr. R. Kobylianskyi, Ukraine.

H. Böttner (Germany)

E. Velmre (Estonia)

A. Prybyla (Ukraine)

R. Gruneisen (France)

Awarding Dr.S. Ašmontas, an ITA academician (Lithuania) the ITA Honorary Golden Prize

Awarding Dr. M. Min (Estonia) the ITA Honorary Golden Prize

Awarding Mr. Kocher, the representative of the SODERN Company (France), the ITA Honorary Golden Prize

The ITA Honorary Golden Prize was given to Dr.S. Ašmontas, an ITA academician (Lithuania) in the nomination "For fundamental contribution into development of thermoelectricity"; the SODERN Company (France) in the nomination "For thermoelectric products quality and technologies"; Dr. M. Min (Estonia) in the nomination "For active promotion of thermoelectricity".

Before the unveiling of the monument to Jean-Charles Peltier in Ham

The key event at the Forum was the unveiling of the monument to Jean-Charles Peltier in Ham, his native town, 130 km away from Paris. The International Thermoelectric Academy acted as the founder of the monument. The monument was fabricated due to the donations of 35 ITA members from 15 countries. Their names are carved on the monument. Other sponsors of the monument are also 19

ITA members, sponsors the monument to Jean-Charles Peltier

Thermoelectric company - sponsors monument Jean Charles Peltier

thermoelectric companies from different countries. The festivities on the unveiling of the monument took place on May 22, 2015.The monument embodies a thermocouple cooling based on the Peltier effect.

Unveiling of the monument to Jean-Charles Peltier

After the unveiling of the monument to Jean-Charles Peltier:
G. Labille, the Mayor of Ham, Dr. L.Anatychuk, ITA President,
Dr. M. Min, Professor of the Tallinn University of Technology

The working model of the Peltier experiment is also installed at the monument. The monument was unveiled in the solemn atmosphere on May 22, 2015.

The Peltier effect demonstration

Taking photos at the monument to Peltier

The monument to Jean-Charles Peltier

In this way the grateful thermoelectricity associates honoured the memory of Jean-Charles Peltier, an outstanding scientist.

ZINOVIY MOISEEVICH DASHEVSKY

(Dedicated to 70-th birthday)

On February 9, 2015 Zinoviy Moiseevich Dashevsky, an academician of the International Thermoelectric Academy, celebrated his 70-th birthday.

Zinoviy Moiseevich Dashevsky was born in Lugansk, Ukraine.

He went into higher education in Russia, at Moscow Institute of Steel and Alloys having graduated in 1968 from the Faculty of Semiconductors and Dielectrics in the specialty of "Electrical Engineering".

In 1973 at the same Institute he defended his PhD Thesis "High-performance thermoelectric films based on *Bi-Te-Sb* solid solutions".

Throughout 1973-1979 Z.M.Dashevsky was a senior research fellow, and since 1979 till 1990 – head of Laboratory for Film Thermoelements at Institute of Current Sources, Scientific-Production Association "Kvant" (Moscow).

In 1987 he defended a thesis for a doctoral degree in engineering on the topic "Film thermoelements: physics and applications" (Saint-Petersburg Technical University). Since 1990 till 1993 he was head of Department for Thermoelectricity at State Research Institute of Current Sources (Moscow), and in 1993 – chief designer of this Institute. He was actively involved in the development of many thermoelectric projects.

During 1992-1994 he held the position of a professor of the Electronics Faculty of Moscow Open University.

Zinoviy Moiseevich was successfully engaged in teaching: at the Electronics Faculty of Moscow Open University he held a special course in "Electronic materials", and at Ben-Gurion University (Beer-Sheva, Israel) – the courses "Technology of semiconductors", "Lithography and melting", "Technology of silicon VLSI" (for post-graduates).

The main lines of Z.M.Dashevsky's research activity include:

- thermoelectricity;
- A^{IV}-B^{VI} semiconductors;
- functionally-graded thermoelectric materials;
- IR-detectors;
- quantum well structures for thermoelectric applications;
- nanocrystalline semiconductors.

The scientist's name is of wide renown in scientific community. Zinoviy Moiseevich is the author of well-known books and monographs:

1. B.Goltsman, Z.Dashevsky, V.Kaidanov, and N.Kolomoyets, Film Thermoelements: Physics and Applications (in Russian) (Moscow: Nauka, 1985), 232 p.

2. I.Balmush, Z.Dashevsky, and A.Casian, Thermoelectric Effects in Multi-Layered Semiconductor Structures (in Russian) (Kishinev: Ştiinţa, 1992), 144 p.

3. Z.Dashevsky, Thermoelectricity in Lead Chalcogenides (chapter in the book "Physics and Application of IV-VI Group Semiconductors"), ed. by D.Khokhlov (Gordon and Breach, 2002).

4. Z.Dashevsky, Highly Light-Sensitive Lead Chalcogenide Films (chapter in the handbook "Semiconductor Nanostructures and Devices"), ed by A.A. Balandin and K.L.Wang (USA, 2005).

For many years professor Dashevsky has been a scientific advisor of students and post-graduates. Under his supervision more than 7 doctoral theses have been defended at Ben-Gurion University.

Z.M.Dashevsky has been an academician of the International Thermoelectric Academy from the date of its founding.

In 2009 Zinoviy Moiseevich was awarded with the Honorary Golden Prize of the International Thermoelectric Academy in the nomination "For Outstanding Achievements in Thermoelectricity".

International Thermoelectric Academy, Institute of Thermoelectricity of the National Academy of Sciences and Ministry of Education and Science of Ukraine, congratulate Zinoviy Moiseevich on his jubilee and wish him sound health and longevity.

VILIUS YAROSLAVOVYCH MYKHAILOVSKY

In March 2015, in the 67-th year of his age, Vilius Yaroslavovych Mykhailovsky, Doctor of Science in Physics and Mathematics, a corresponding member of the International Thermoelectric Academy, a leading research fellow of Institute of Thermoelectricity of the National Academy of Sciences and Ministry of Education and Science of Ukraine passed away.

Vilius Yaroslavovych Mykhailovsky was born on April 2, 1948 in the village of Verenchanka, Zastavna district, Chernivtsi region.

He started his professional life in 1969 as a laboratory assistant at Chernivtsi State University and continued his work there as a senior laboratory assistant and engineer.

While continuing to work, he studied at the Faculty of Chemistry, and obtained a diploma of a chemist in 1972. On completing his military service, he worked as a senior research fellow at the Faculty of Chemistry of Chernivtsi University.

In 1980 V.Ya.Mykhailovsky defended his PhD thesis, and in 2007 – a doctoral thesis "Organic-fuelled thermoelectric generators".

Since 1980 he held the position of a senior engineer, then a leading engineer of Scientific Design-Technological Office "Phonon"; since 1991 he was head of a Laboratory for Chemical Sources of Heat at Institute of Thermoelectricity, and in 2001 he was appointed to the position of a senior research fellow of this Institute.

As a principal investigator and leader V.Ya.Mykhailovsky took part in 18 research and development projects, wherein 16 various-purpose electric energy sources were developed: for power supply to radio and television equipment, telemetry systems, lighting and battery charging, as well as combined heat and electricity sources for production facilities and amenity spaces.

The main lines of scientific activity of V.Ya.Mykhailovsky include:

- thermoelectric generators with organic-fuelled heat sources;

- heat sources for thermal generators: processes and technology of thermal energy production by catalytic and flame combustion of organic fuels; catalyst technology;

- combined sources of thermal and electrical energy;

- thermoelectric modules for electric energy generation.

Apart from research and development activity, the scientist was engaged in teaching work.

He is the author of over 120 research papers, 24 inventions and patents and was elected head of All-Ukrainian Public Organization of Thermoelectricians.

International Thermoelectric Academy, Institute of Thermoelectricity of the National Academy of Sciences and Ministry of Education and Science of Ukraine, founders of "Journal of Thermoelectricity" and its editorial staff are deeply mourning for the untimely end of Vilius Yaroslavovych Mykhailovsky and extend their sincere condolences to his family. The name of Vilius Yaroslavovych will live forever in the memory of those who knew him and loved him.

ARTICLE PREPARATION RULES

The article shall conform to the journal profile. The article content shall be legible, concise and have no repetitions.

The article shall be submitted to the editorial board in electronic version.

The text shall be typed in text editor not lower than MS Word 6.0/7.0.

Page setup: "mirror margins"- top margin – 2.5 cm, bottom margin – 2.0 cm, inside – 2.0 cm, outside– 3.0 cm, from the edge to page header – 1.27 cm, page footer – 1.27 cm.

Graphic materials, pictures shall be submitted in color or, as an exception, black and white, in .opj or .cdr formats, .jpg or .tif formats being also permissible. According to author's choice, the tables and partially the text can be also in color.

The article shall be submitted in English on A4 paper sheets; the number of pages shall not exceed 12. By agreement with the editorial board, the number of pages can be increased.

To accelerate publication of the article, please adhere to the following rules:

- the authors' initials and names are arranged in the centre of the first page at the distance of 1 cm from the page header, font Times New Roman, size 12 pt, line spacing 1.2;
- the name of organization, address (street, city, postal code, country) – indent 1 cm below the authors' initials and names, font Times New Roman, size 11 pt, line spacing 1.2, center alignment;
- the title of the article is arranged 1 cm below the name of organization, in capital letters, semi-bold, font New Roman, size 12 pt, line spacing 1.2, center alignment. The title of the article shall be concrete and possibly concise;
- the abstract is arranged 1 cm below the title of the article, font Times New Roman, size 10 pt, in italics, line spacing 1.2 ,center alignment;
- key words are arranged below the abstract, font Times New Roman, size 10 pt, line spacing 1.2, justified alignment. The title "Key words" – font Times New Roman, size 10 pt, semi-bold;
- the main text of the article is arranged 1 cm below the abstract, indent 1 cm, font Times New Roman. size 11 pt, line spacing 1.2, justified alignment;
- formulae are typed in formula editor, fonts Symbol, Times New Roman. Font size is "normal" – 12 pt, "large index" – 7 pt, "small index" – 5 pt, "large symbol" – 18 pt, "small symbol" – 12 pt). The formula is arranged in the text, centre aligned and shall not occupy more than 5/6 of the line width, formulae are numbered in round brackets right;
- dimensions of all quantities used in the article are represented in the International System of Units (SI) with the explication of the symbols employed;
- figures are arranged in the text. The figures and pictures shall be clear and contrast; the plot axes – parallel to sheet edges, thus eliminating possible displacement of angles in scaling;
- tables are arranged in the text. The width of the table shall be 1 cm less than the line width. Above the table its ordinary number is indicated, right alignment. Continuous table numbering throughout the text. The title of the table is arranged below its number, center alignment;
- references should appear at the end of the manuscript. References within the text should be enclosed in square brackets. References should be numbered in order of first appearance in the text. Examples of various reference types are given below.

– L.I. Anatychuk, *Thermoelements and Thermoelectric Devices: Handbook* (Kyiv: Naukova Dumka, 1979), p.766. (Book)
– T.M. Tritt, Thermoelectric Phenomena, Materials, and Applications, *Annual Review of Materials Research* **41**, 433 (2011). (Journal paper)
– U. Ghoshal, *Proceedings of the XXI International Conference on Thermoelectrics* (N.Y., USA, 2002), p. 540. (Proceedings Conference)

The article should be supplemented by:

• letter from the organization where the work was performed or from the authors of the work applying for the publication of the article;

• information on the author (authors): last name and initials; full name and postal address of the institution where the author works; academic degree; position; telephone number; E-mail;

• author's (authors') photo in color or, as an exception, in black and white. With the number of authors more than two their photos are not given;

• author's application to the following effect:

We, the undersigned authors, … transfer to the founders and editors of "Journal of Thermoelectricity" the right to publish the article…in Ukrainian, Russian and English. This is to confirm that the present publication does not violate the copyright of other persons or organizations.

Date Signatures